Università di Pisa

Dipartimento di Fisica "E. Fermi"

Elasticity and yielding in model polymer glasses

Candidate
Nicola Calonaci

Supervisor
Prof. Dino Leporini

Academic year
2015/2016

Preface

The state of matter called *glass* is characterized by the complete arrest of the dynamics on the experimental time-scale. The sharp increase in the structural relaxation time and in the viscosity of the glass-forming liquids is evidence of this arrest. Despite the accompanying discontinuity in the second order thermodynamic quantities, the glass transition cannot be considered a proper phase transition, as the glassy state is out of equilibrium.

Since all materials potentially form glass under specific conditions, the glass transition is a universal phenomenon, but it is more easily observed in some materials, among which *polymers* constitute an important class.

Polymers are systems of chain-like molecules composed by repeating units. The key feature of these systems is the *connectivity* arising from the presence of many bonds. It makes polymers exhibit a complex solidification behaviour, with an intrinsic difficulty to crystallize which favours glass formation.

In addiction to their suitability for fundamental studies of the glass transition, solid-state polymers play a significant role in technology. They are appreciated mainly because of their mechanical properties, whose microscopic origin is not yet exhaustively understood.

Molecular dynamics (MD) simulations prove an invaluable tool in this research field, since they allow for the complete control over the system under study, and for the analysis of many properties which would otherwise be inaccessible through experiment.

The goal of this thesis is to characterize the mechanical response to deformations of a coarse-grained polymer model in the glassy state. In particular, we want to relate the mechanical behaviour to connectivity. To this aim MD simulations are performed with systematic variation of bond length and chain stiffness, which are the interaction parameters determining the connectivity of the model. Mechanical deformation is simulated via the Athermal Quasi-Static (AQS) procedure at zero temperature. We show that connectivity does not directly affect the elastic shear modulus. However, since the latter depends on the morphology of the solid state, connectivity still plays a role as it determines the solidification behaviour of the model.

In the plastic regime, we show that the stress at yielding depends on the connectivity-related parameters of the model. Moreover, we find a correlation between the elastic shear modulus and the stress at yielding, compatible with experimental data reported in the literature.

The thesis is structured in the following way:

Chapter 1

An introduction to the physics of glass transition is given, with particular attention to the processes of crystal nucleation and growth, and to how these can be hindered by supercooling and eventually glass transition. In the same chapter, we introduce the essential features of polymers and we discuss the main concepts of the theory of mechanical response.

Chapter 2

The numerical techniques adopted in this work are reported. After a brief introduction to molecular dynamics simulations, we discuss in detail the chosen polymer model, the simulation protocol followed to obtain zero temperature solids and simulate deformation, and the program for data analysis.

The **original results** of this work are presented in chapters 3 to 5.

Chapter 3

First the liquid phase of the model is characterized, by measuring the spatial distribution and ordering of monomers at finite temperature. Then a linear cooling down of the samples is simulated, and the same measurements are carried out in the glassy state at zero temperature.

Chapter 4

The zero temperature solids are deformed via the AQS shear protocol. The elastic shear modulus determining the linear response to small strains is measured. Plastic yielding events are observed at larger strains and the corresponding stress is measured. The existence of a correlation between the elastic linear response and the highly nonlinear plastic behaviour is investigated. Finally we compare our results with experimental data reported in the literature.

Chapter 5

A summary of the main original results of the thesis is reported.

Contents

Preface iii

1 Introduction 3
- 1.1 The glass transition . . . 3
- 1.2 The Angell plot . . . 8
- 1.3 Polymers . . . 11
- 1.4 Mechanical response . . . 14

2 Numerical simulations of polymers 19
- 2.1 Molecular dynamics . . . 19
- 2.2 The NPT ensemble . . . 20
- 2.3 Equations of motion . . . 22
- 2.4 Periodic boundary conditions . . . 23
- 2.5 Polymer model . . . 25
- 2.6 Reduced units . . . 27
- 2.7 Simulation protocol . . . 28
  - 2.7.1 Preparation . . . 28
  - 2.7.2 Equilibration . . . 29
  - 2.7.3 Cooling . . . 30
  - 2.7.4 Deformation . . . 30
- 2.8 Data analysis . . . 31

3 Static properties in the liquid and solid phases 33
- 3.1 Introduction . . . 33
- 3.2 Quantities of interest . . . 34
  - 3.2.1 Radial pair distribution function $g(r)$ . . . 34
  - 3.2.2 Angular distribution function $ADF\,(\Delta r, \cos\phi)$ . . . 35
  - 3.2.3 Bond angle distribution function $P(\cos\theta_b)$ . . . 36
  - 3.2.4 Orientational order parameters . . . 37
- 3.3 The liquid phase . . . 38
  - 3.3.1 Bond length . . . 38

3.3.2 Chain stiffness 43
3.4 The solid phase 46
3.4.1 Bond length 47
3.4.2 Chain stiffness 56
3.5 Conclusions 66

4 Elastic and yielding properties at zero temperature 67
4.1 Introduction 67
4.2 Shear modulus 70
4.3 Yielding properties 73
4.4 Conclusions 78

5 Summary of results 81

A Monitoring of thermodynamic quantities 83

Bibliography 85

Chapter 1

Introduction

1.1 The glass transition

When a liquid is cooled down, the motion of its constituent atoms or molecules slows down, due to decreasing thermal energy. As the temperature goes through the freezing point T_M a first order phase transition is usually expected to take place, which turns the liquid into a crystal. The process of crystallization consists in two major events: nucleation and crystal growth.

Nucleation is the stage at which some atoms or molecules of the liquid begin to gather in clusters characterized by an ordered structure, which are the nuclei of the crystalline phase. This process is driven by spontaneous density fluctuations and requires a certain amount of work to be done, since the free energy gain due to the inner order of the new phase competes with the energy loss required for the formation of an interface between the crystal and liquid phases. The resulting energy barrier between the minima corresponding to the two phases is sketched in the right panel of fig. 1.1.

The minimum reversible work needed for the formation of a crystal embryo of n molecules in an incompressible liquid, under conditions of constant temperature T and pressure P is

$$W_{min} = \sigma A + n\left[\mu'(T,P) - \mu(T,P)\right] \tag{1.1}$$

as derived in [1], where σ is the surface tension, A the inter-facial area between the embryo and the bulk phase, μ' and μ the chemical potentials in the embryo and bulk phase respectively. The first term is positive and surface dependent, while the second is negative and depends on volume, so that eq. (1.1) can be written

$$W_{min}(r) = br^2 - cr^3 \tag{1.2}$$

where b and c are positive constants, and r is the radius of the crystal embryo, assumed to be spherical.

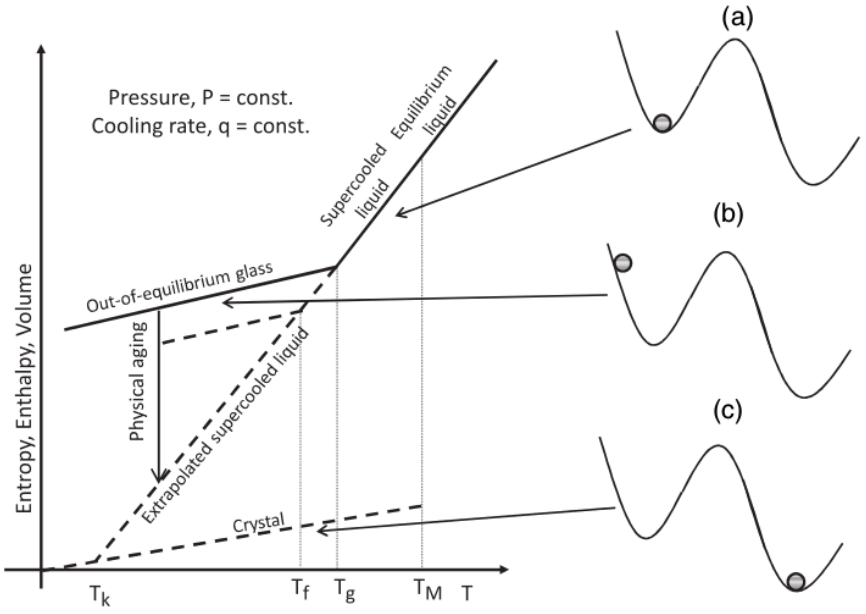

Figure 1.1: Left: typical temperature dependence of first order thermodynamic quantities such as enthalpy, entropy, volume, etc. Right: schematic plot of the free energy barrier between a liquid (shallower minimum) and a crystalline state (deeper minimum). At $T = T_M$ a liquid can either crystallize (c) or keep in the metastable state of a supercooled liquid (a). As cooling is carried on, the supercooled liquid eventually falls out of equilibrium (b). This happens at the glass transition temperature T_g. Adapted from [2].

Therefore, the work required for nucleation has the form of an energy barrier (fig. 1.2) depending on the size of the nucleus, so that a critical size r^* which maximizes $W_{min}(r)$ can be identified as that at which nucleation has become effective. Nucleation is thus a thermally activated process. When a critical-sized nucleus has formed, it then begins to grow spontaneously.

The number of critical-sized embryos formed at a temperature $T \leq T_M$ is expected to have a Boltzmann distribution

$$\rho_n(T) \sim \exp\left(\frac{W_{min}(r^*, T)}{k_B T}\right) \tag{1.3}$$

where k_B is the Boltzmann constant. However, nucleation cannot be described only by equilibrium thermodynamics. When a nucleus has formed,

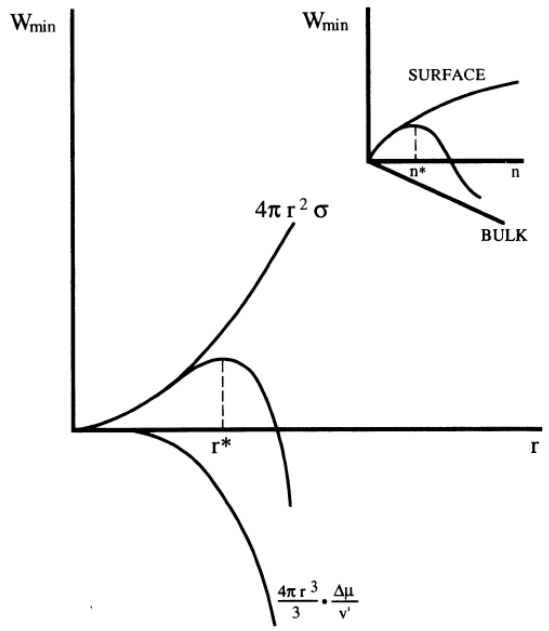

Figure 1.2: Surface and volume contributions to the energy barrier representing the work needed for the formation of a crystal embryo of radius r. Adapted from [1].

additional atoms or molecules must be transported on it, in order for critical size to be reached. This process has a kinetic nature. Since the ability of transporting matter from a point to another of a system is characterized by its diffusion coefficient D, the rate J of formation of a critical nucleus is expected to have the form

$$J(T) \sim \rho_n(T) \cdot D(T) \tag{1.4}$$

i.e. to be proportional both to the probability of a nucleus to be formed, and to the rate at which matter is transported on it.

At fixed temperature and rate J, a certain amount of time $t(\phi)$ is needed for the growth of a fraction ϕ of crystal phase. For instance, if the critical nucleus is assumed to be spherical and expanding with constant velocity u, at any time this fraction can be estimated as

$$\phi(t) = \int_0^t J\frac{4}{3}\pi \left[\int_0^{t'} u dt''\right]^3 dt' = \frac{\pi}{3} J u^3 t^4 \tag{1.5}$$

so that the time needed for a crystal fraction ϕ to grow is

$$t(\phi) = \left(\frac{3\phi}{\pi J u^3}\right)^{1/4} \tag{1.6}$$

If the system is cooled down beyond the freezing point ($T \leq T_M$), the cooling rate required to obtain a fraction ϕ of crystal phase can be estimated as

$$|\dot{T}| \sim \frac{T_M - T}{t(\phi)} \tag{1.7}$$

The critical cooling rate under which complete crystallization is achieved is obtained by imposing $\phi = 1$ in eq. (1.7):

$$|\dot{T}|_{critical} = (T_M - T)\left(\frac{\pi J u^3}{3}\right)^{1/4} \tag{1.8}$$

If the cooling process is faster than crystal growth, i.e. for cooling rates $|\dot{T}| > |\dot{T}_{critical}|$, crystallization can be hindered, completely or in part. It is important to notice that this can happen even if the crystal phase is the energetically favoured one.

The state of a liquid which has not crystallized at $T \leq T_M$ is called the *supercooled* state (situation (*a*) in fig. 1.1). From a thermodynamic point of view, despite not being in the lowest (absolute) energy minimum, supercooled liquids are classified as metastable, which means they are stable under small perturbations. Due to its location in a free energy minimum, the configuration of a supercooled liquid can persist over infinitely large time scales and the principles of classical equilibrium thermodynamics can be generally applied.

Upon cooling below the freezing point T_M, the supercooled liquid is characterized by a dramatic increase in the viscosity with decreasing temperature (see section 1.2). Such an increase in viscosity implies the concomitant slowing down of the typical relaxation time of the associated spontaneous fluctuations. The phenomenon related to such relaxation time is normally called the α process, and the characteristic time is called τ_α.

For instance, consider the spontaneous density fluctuations due to molecular rearrangement, which allow for the nucleation process. The dynamics of these rearrangements are described by the diffusion constant D, which is related to the viscosity η by the *Stokes-Einstein* relation

$$D = \frac{k_B T}{6\pi\eta a} \tag{1.9}$$

where a is the effective radius of the molecules. The sharp increase in viscosity implies a strong decrease in diffusivity. As a consequence, the characteristic time for molecular rearrangement τ_α becomes increasingly large, in such a way that it can exceed the experimental time scale (e.g. the inverse of cooling rate).

When this happens, the supercooled liquid appears structurally arrested, keeping in the same state around that of metastable equilibrium (situation (b) in fig. 1.1). This out-of-equilibrium state is called a *glass*. A glass has the mechanical properties of a solid, but it still exhibits the typical structural features of a disordered liquid.

The state in which the system is arrested can be one in which nucleation has started, so that a fraction of crystal phase ϕ can be observed in the glass. The structure of partially crystalline samples is strongly affected by the procedure of solidification, thus constituting a memory of the thermal history, for instance of solidification temperature and cooling rate.

The transition from a liquid to a glass occurs in a relatively narrow range around a reference glass transition temperature T_g. This temperature is identified as that at which a jump in the second order thermodynamic properties of the supercooled liquid (e.g. the thermal expansion coefficient) is observed (see left part of fig. 1.1). Despite the observed jump in the second order thermodynamic properties, the glass transition does not fulfil the requirements of a phase transition in a strict sense. For instance it is well documented [3] that it doesn't satisfy the relation

$$\Pi = \frac{\Delta k \Delta C_p}{TV\left(\Delta\alpha\right)^2} = 1 \tag{1.10}$$

which stands for second-order phase transitions, where Δk, ΔC_p and $\Delta\alpha$ are the variations, at the transition point, of compressibility, heat capacity at constant pressure and coefficient of thermal expansion respectively; Π is known as the Prigogine-Defay ratio.

Rather, from a thermodynamic point of view, glasses belong to the category of non-equilibrium systems (fig. 1.1(b)). If the glass transition temperature T_g is defined as that at which liquid and vitreous behaviours of the volume versus temperature intersect, we find out that it usually occurs around $\frac{2}{3}T_M$. In the narrow temperature range between T_M and $\approx \frac{2}{3}T_M$, the structural relaxation time τ_α increases in a very sharp fashion, reaching the order of 100 seconds [4, 5] at T_g, from the order of picoseconds at T_M (see fig. 1.3). Similarly the viscosity η, which starts from values around $10^{-1}P$ ($10P = 1Pa \times s$) at the freezing point, reaches order $10^{13}P$ at T_g. Viscosity is thus extraordinarily sensitive to temperature around T_g and assumes values that make glass behave mechanically like a solid on the experimental scale.

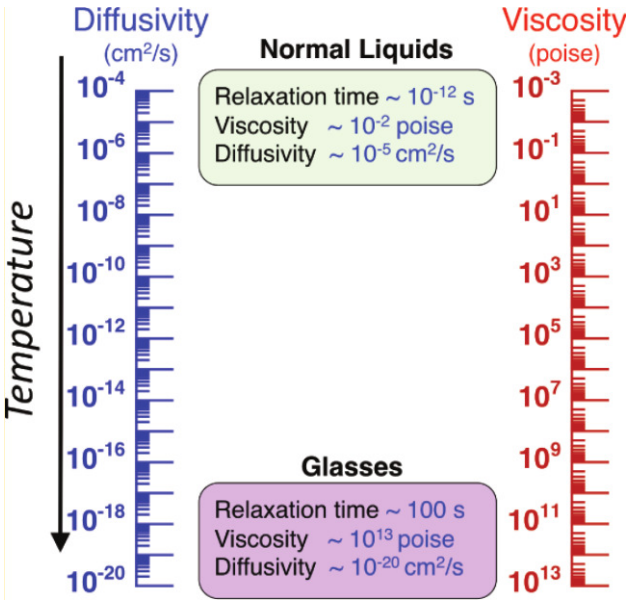

Figure 1.3: Comparison of the diffusivity and viscosity between a typical liquid (such as the water at room temperature) and a typical glass. Note the huge increase of the relaxation time from $10^{-12}s$ to $10^{2}s$. Reprinted from [4].

One of the most interesting peculiarity of the glass transition is its universality, in the sense that all kind of liquid potentially glass-forms, from atomic (both non-metallic and metallic [6]) to polymeric [7], from the ones in which dispersion forces dominate to those characterized by hydrogen and covalent bonds. Clearly these properties play a role in the experimental difficulty (e.g. large critical cooling rate) encountered in supercooling and then vitrifying a liquid. In this sense we speak about good or bad glass formers. Organic and ionic liquids, silicates, polymers and also some metallic liquids are good glass formers [8].

1.2 The Angell plot

Close to T_g, the viscosity of liquids like silica (SiO_2) exhibits Arrhenius temperature dependence

$$\eta(T) \sim \exp\left[\frac{\Delta E}{k_B T}\right] \tag{1.11}$$

where ΔE represents a temperature independent barrier of energy, to be overcome by thermal fluctuations [9]. Other liquids, like many polymers, are

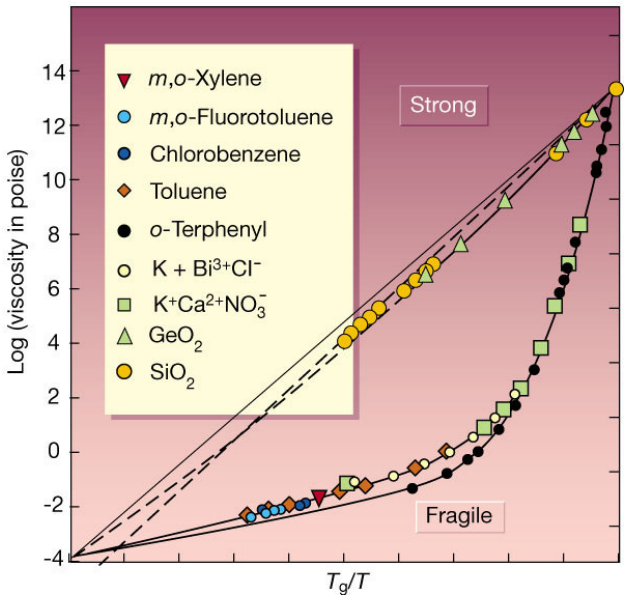

Figure 1.4: Angell plot showing the viscosity as a function of the inverse temperature normalized at the glass transition temperature T_g for different substances. An Arrhenius behaviour results in a straight line in this plot. This is typical of strong glass-formers. Non-Arrhenius increase of the viscosity corresponds to fragile glass-formers. Reprinted from [9].

characterized by a more dramatic increase in the viscosity with decreasing temperature.

The Angell plot [10], shown in fig. 1.4, displays the temperature dependence of the viscosity of a wide variety of supercooled liquids at atmospheric pressure. Defining T_g as the temperature at which viscosity reaches the value of $\eta(T_g) = 10^{13}P$, all the curves are normalized to the same value at T_g.

Two different types of behaviour are brought forth in this plot: strong and fragile. The dynamics of strong liquids are characterized by a clear Arrhenius behaviour, and the corresponding curves of $\log \eta(\frac{T_g}{T})$ in fig. 1.4 are straight. The other family of curves, to which the vast majority of glass-forming polymers belong, corresponds to fragile liquids, for which the viscosity increases much more strongly upon cooling toward T_g. These non-Arrhenius data are often fitted [9] by the Vogel-Fulcher-Tammann (VFT) expression:

$$\eta(T) \sim \exp\left[\frac{A}{T - T_0}\right] \tag{1.12}$$

where A is a temperature independent constant. Equation (1.12) implies a

Table 1.1: Fragility m and glass transition temperatures T_g of some common polymers.

	m	$T_g(K)$
PVC	191	352
Toluene	107	126
PVAc	95	311
Se	87	308
OTP	81	240
Glycerol	53	190
B_2O_3	32	554
SiO_2	20	1700
GeO_2	20	818

divergence of the viscosity at the finite temperature T_0, a prediction that cannot be verified because the system is supposed to fall out of equilibrium as T_0 is approached. However, the physical origin of the non-Arrhenius behaviour of fragile liquids is still an actively investigated question, and many other good fits of these curves exist (for instance see [11–13]).

An established result is the correlation between the different behaviour of viscosity and a different evolution of short range order: strong liquids typically have a local tetrahedral structure, which persists across the glass transition, whereas any remnants of the structure in which a fragile liquid is trapped under T_g rapidly disappear upon heating above T_g. The structural (in)stability is reflected in the (large) small changes in heat capacity and thermal expansion coefficient across the glass transition [14].

While crystal solids are easily classified by their structure, in liquids and glasses this is not possible, as their structure is amorphous and strongly depends upon the cooling history. The Angell plot offers a way to classify liquids through their fragility, which is defined as

$$m = \left. \frac{\partial \log \eta}{\partial \left(\frac{T_g}{T} \right)} \right|_{T=T_g} \tag{1.13}$$

The van der Waals molecular liquids, such as o-terfenile OTP and toluene C_7H_8 are the classical fragile ($m = 70 \div 150$) systems. The strong glass-formers ($m = 17 \div 35$) are instead characterized by strong covalent directional bonds, forming space-filling networks (like silica SiO_2 and germanium dioxide GeO_2). Hydrogen bonded materials (like glycerol or propylene glycols) present an intermediate level of fragility ($m = 40 \div 70$). Some specific

values of m and T_g are reported in table 1.1.

1.3 Polymers

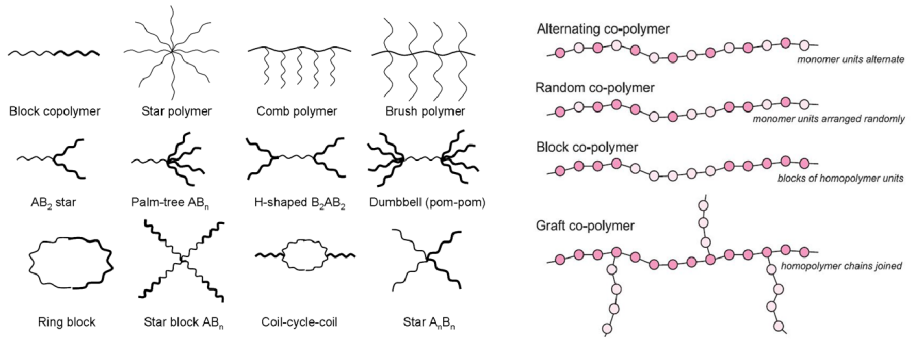

Figure 1.5: Some of the many different types of polymer. Differences can be found both in chain architecture (left panel) and in chain constitution (right panel).

According to the definition given in [15], a polymer is a substance composed of molecules characterized by the repetition of one or more species of atoms, called constitutional repeating units (or *monomers*), linked to each other in amounts sufficient to provide a set of properties which do not change markedly with the addiction of one or a few more constitutional repeating units.

Polymer chains can be classified by their *conformation* and *configuration*. The conformation of a polymer chain is its spatial organization. Many different conformations exist: linear, star, comb etc. Some of them are reported in the left part of fig. 1.5. On the other hand, the configuration is the succession of chemical elements along the chain. We distinguish homopolymers, consisting in chains of a single repeated unit, from copolymers, i.e. chains of monomers of different species, arranged in an alternating, random, block or other ways (right part of fig. 1.5).

Polymers are essential and ubiquitous in everyday life. For instance, proteins and nucleic acids, which play a basic role in the control of life processes, are polymers; other natural polymers are rubbers and cellulose, which is the basic constituent of wood and paper, while the list of synthetic polymeric systems include window glass, optical fibres and most engineering and commodity plastics.

The feature which makes polymers peculiar objects for physical investigations is chain connectivity. In the molten phase, while monomers pack densely in an amorphous structure characterized by short range order and low compressibility, a behaviour equivalent to that of simple non-polymeric liquids [16], on the chain scale additional features are brought forth by the strong interpenetration of the chains. For instance, the screening of the intramolecular excluded volume interaction, which makes the chains behave approximately as random coils on long length scales. Chain interpenetration also gives rise to temporary networks of entanglement which slow down relaxation processes and make the melt viscoelastic already at high temperatures [17].

The competition between chain-scale and monomer-scale spatial disposition gives rise to the phenomenon of geometrical frustration: at low temperature, the tendency of monomers to assume positions corresponding to an ordered configuration is opposed by the constraints imposed by the conformation of the chains. For polymers with regular enough chain structure, this usually results in two phase structures, in which crystalline and amorphous regions alternate [18]. For those polymers which have a strongly irregular chain structure, such as atactic and random copolymers, crystallization is completely inhibited, and in general even for those which own an ordered ground state the ordering is kinetically hard to achieve. For this reason polymers, except for a few cases [19], are usually good glass formers.

Besides being efficient systems for the fundamental investigation of the glass transition, another appreciable feature of glassy polymers lays in their mechanical properties: subjection to large strains can lead a polymer to harden and response toughly, instead of failing abruptly like in the case of crystalline solids [17].

The target systems of this work are simple linear homopolymers. The variables used for the description of the chain conformation in linear homopolymers are, with reference to fig. 1.6:

- the N bond vectors $\mathbf{b}_i = \mathbf{r}_i - \mathbf{r}_{i-1}$ linking the ith and $(i-1)$th monomers of a chain, with $i = 1, \ldots, N$;
- the $N-1$ bond angles $cos(\theta_i) = \frac{\mathbf{b}_i \cdot \mathbf{b}_{i+1}}{|\mathbf{b}_i||\mathbf{b}_{i+1}|}$ with $i = 1, \ldots, N-1$
- the end-to-end vector joining the first and the last monomers of the chain

$$\mathbf{R}_{ee}^2 = |\mathbf{r}_N - \mathbf{r}_0| = \sum_{i=1}^{N} \sum_{j=1}^{N} \mathbf{b}_i \cdot \mathbf{b}_j. \tag{1.14}$$

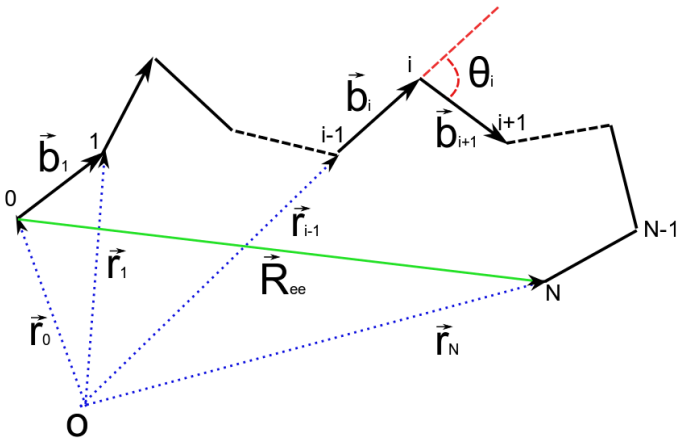

Figure 1.6: Notation for the description of the conformation of polymer chains.

The most simple model describing linear homopolymers is the *freely jointed* model [20], in which the chain-composing segments have fixed length b and point in any direction independently of each other. Within this model the average magnitude of the end-to-end vector $\mathbf{R}_{ee}$ in a chain of N monomers is given by

$$< R_{ee}^2 >= Nb^2 \tag{1.15}$$

equal to the mean square displacement of a random walk of N steps of length b. The flexibility of any polymer is characterized by the length scale of segments in which the chain must be decomposed in order for these segments to be freely jointed. This length scale is known as the *Kuhn length* l_k and is defined as the ratio

$$l_k = \frac{< R_{ee}^2 >}{L} \tag{1.16}$$

where $L = Nb$ is the contour length of the chain.

For fully flexible chains with average bond length l_b the end-to-end vector is just $< R_{ee}^2 >= Nl_b^2$ which yields a Kuhn length

$$l_k|_{fully\ \ flexible} = \frac{Nl_b^2}{Nl_b} = l_b \tag{1.17}$$

which means that the real bonds are practically freely jointed.

In the converse case of rigid rod-like polymers, chains are fully stretched, so that the length of the end-to-end vector equals L , i.e. $< R_{ee}^2 >= (Nl_b)^2$, yielding

$$l_k|_{rod-like} = \frac{(Nl_b)^2}{Nl_b} = L \tag{1.18}$$

The fully flexible and the rod-like models are the extremal versions of the linear homopolymer, and intermediate cases can be found in nature. It is interesting to understand whether and how chain flexibility can affect the morphology of the solids formed by polymer liquids upon cooling, and also their mechanical properties.

The complex structure of polymers brings about the presence of multiple relaxation phenomena, each characterized by some typical time scale. An example is the structural (α) relaxation, that is the escape process of monomers from the cage of nearest neighbours inside which they are confined to vibrate for an average time τ_α.

Another important relaxation process is that of chains losing memory of their initial conformation. This process is characterized by the autocorrelation function $C_{ee}(t)$ of the end-to-end vector $\mathbf{R}_{ee}$

$$C_{ee}(t) = \frac{1}{N_c} \sum_{p=1}^{N_c} \frac{\mathbf{R}_{ee}^p(t) \cdot \mathbf{R}_{ee}^p(0)}{R_{ee}^2(0)} \tag{1.19}$$

where the p index runs over all the chains of the system, and N_c is the total number of chains. This correlation function decreases exponentially in time, with a characteristic time-scale τ_{ee} given by

$$C_{ee}(\tau_{ee}) = e^{-1} \tag{1.20}$$

It is assumed [20] that in a polymer melt without permanent chain entanglements, τ_{ee} is the maximum relaxation time, as the chain-scale rearrangement represents the slowest motion in absence of collective modes.

1.4 Mechanical response

Here we give a brief introduction to the theory of the mechanical response in rigid bodies, in the way it is presented in [21].

Upon application of external forces, solid bodies are deformed, i.e. they change in shape and volume. When a body is deformed, in general every point in it is displaced. A displacement field vector $\mathbf{u}(\mathbf{X}) = \mathbf{x} - \mathbf{X}$ is defined in any of these points, where $\mathbf{X}$ is the position before deformation and the new position is a function of the previous one $\mathbf{x} = \mathbf{x}(\mathbf{X})$. The change in the distance $d\mathbf{X}$ of any two infinitesimally near points can be written in terms of a tensor in the following way:

$$|d\mathbf{x}|^2 - |d\mathbf{X}|^2 = 2u_{ik} dX_i dX_k \tag{1.21}$$

where dX_i is the ith Cartesian component of the original infinitesimal distance $d\mathbf{X}$ and the symmetrical tensor

$$u_{ik} = \frac{1}{2}\left(\frac{\partial u_i}{\partial X_k} + \frac{\partial u_k}{\partial X_i} + \frac{\partial u_l}{\partial X_i}\frac{\partial u_l}{\partial X_k}\right) = u_{ki} \tag{1.22}$$

is called the *strain tensor*.

When a body is deformed, the arrangement of molecules in it is changed from that of mechanical equilibrium. The internal forces which therefore arise, in order to return the body to equilibrium, are called *internal stresses*. Any portion of the body is subjected to a force of this kind, which is the sum of the forces exerted on it by all the surrounding portions. This force can be considered to act only on the surface of that portion of the body, and for this reason its per unit volume form $\mathbf{f}$ can be expressed as the divergence of a tensor of rank two

$$f_i = \frac{\partial \sigma_{ik}}{\partial X_k} \tag{1.23}$$

where σ_{ik} is called the *stress tensor* and can be shown to be symmetrical. The component σ_{ik} of the stress tensor is the ith component of the force on the unit area perpendicular to the k axis.

For small deformations the displacement field u and its derivatives are also small, so that we can keep just the first two terms in eq. (1.22), yielding

$$u_{ik} = \frac{1}{2}\left(\frac{\partial u_i}{\partial X_k} + \frac{\partial u_k}{\partial X_i}\right) \tag{1.24}$$

The work per unit volume done by internal stresses upon a small change δu in the displacement field can be shown to be

$$\delta W = -\sigma_{ik}\delta u_{ik} \tag{1.25}$$

If the process of deformation is also so slow that the deformed body is in thermodynamic equilibrium at every instant, then it is a reversible process and the corresponding variation of free energy is

$$dF = -SdT + \sigma_{ik}du_{ik} \tag{1.26}$$

where S and T are the entropy and temperature of the body. We thus have

$$\sigma_{ik} = \left(\frac{\partial F}{\partial u_{ik}}\right)_T \tag{1.27}$$

Assuming the deformed body to be isotropic, since deformations are small the variation of free energy (i.e. elastic energy) can be expanded in powers of u_{ik} as far as second order

$$\Delta F = \frac{1}{2}\lambda u_{ii}^2 + \mu u_{ik}^2 \tag{1.28}$$

where λ and μ are the so called Lamé coefficients. Only the two independent scalars of second order of the strain tensor appear, as absence of thermal expansion is assumed so that $\sigma_{ik}(u_{ik} = 0) = 0$ due to eq. (1.27).

The strain tensor can be decomposed in the sum of a simple shear u^s_{ik} (no variation of volume, $Tr(u^s_{ik}) = 0$) and a hydrostatic compression u^h_{ik} (no variation of shape, $u^h_{ik} = constant \times \delta_{ik}$) in the following way:

$$u_{ik} = \left(u_{ik} - \frac{1}{3}\delta_{ik}u_{ll}\right) + \frac{1}{3}\delta_{ik}u_{ll} \tag{1.29}$$

Replacing this expression in eq. (1.28) and deriving the elastic energy ΔF with respect to u_{ik} gives a linear relation between the strain and stress tensors:

$$\sigma_{ik} = Ku_{ll}\delta_{ik} + 2\mu\left(u_{ik} - \frac{1}{3}\delta_{ik}u_{ll}\right) \tag{1.30}$$

which is called the *Hooke's law*. The quantities μ and $K = \frac{2}{3}\mu + \lambda$ are always positive and they are respectively called the shear and bulk modulus, as they singularly appear in eq. (1.30) if the strain is either a simple shear or a hydrostatic compression.

Hooke's law can be generalized as to describe the linear elastic response of non isotropic bodies. In this case eq. (1.30) has the form

$$\sigma_{ik} = C_{ikjl}u_{jl} \tag{1.31}$$

where C_{ikjl} is the *modulus tensor* [22]. For each of the six mutually independent deformations, namely hydrostatic compression, plane strain and triaxial shear deformations, simple xy, xz and yz shear deformations, the corresponding linear stress-strain relations can be derived for small strains. For instance, the stress-strain relations for simple shear deformations are

$$\sigma_{xy} = C_{xyxy}u_{xy} = 2G_3u_{xy} \tag{1.32}$$

$$\sigma_{xz} = C_{xzxz}u_{xz} = 2G_4u_{xz} \tag{1.33}$$

$$\sigma_{yz} = C_{yzyz}u_{yz} = 2G_5u_{yz} \tag{1.34}$$

The G coefficients are the generalized shear moduli for simple shear deformations.

The strain range of validity of Hooke's law in a material is usually included in its elastic limit. In this limit the deformed body returns to its undeformed state once the external forces causing the deformation cease to act.

Larger deformations, which cause a residual deformation to remain after removal of these external forces, are said to be plastic.

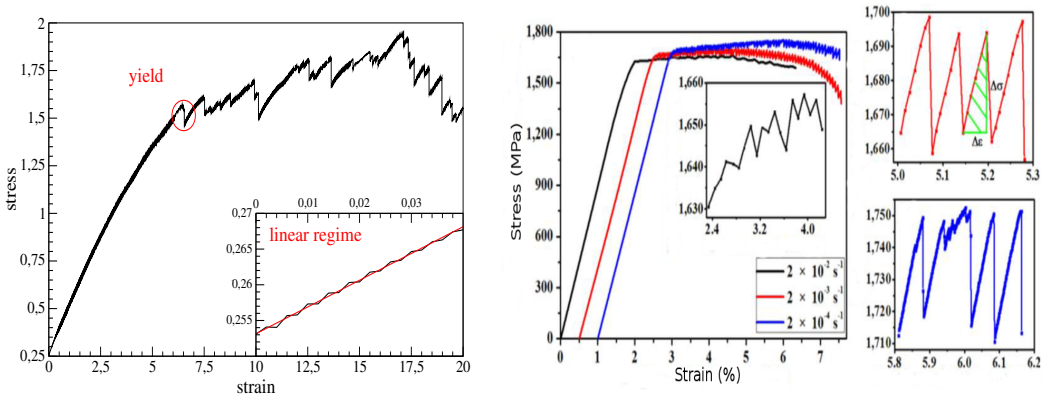

Figure 1.7: Left panel: a typical stress-strain curve obtained in our simulations. In the inset, the linear Hooke-like response for very small deformations is shown (fit curve in red). For larger strains, stress round off and eventually drops at yielding. Elastic and plastic events alternatively occur for the whole deformation process. Right panel: experimental stress-strain curve of a $Pd_{75}Si_{15}Ag_3Cu_7$ bulk metallic glass sample under uniaxial compression at different strain rates, reprinted from [23].

The mechanical response of any material is characterized by its stress-strain curve, which is unique for each material and also depends strongly on the deformation procedure. In fig. 1.7 we show both a typical stress response obtained via simulation of a polymer material loaded at zero strain rate, through the athermal quasi-static deformation protocol (see section 4.1), and the experimental stress-strain curve of a metallic glass subjected to uniaxial compression at different strain rates [23]. Despite the large differences between studied systems and procedures of measurement, some common characteristics can be observed. For instance, notice that the range of strains in which the response of the material is linear, i.e. the Hooke's regime, is usually one or more orders of magnitude smaller than that of plastic yielding.

As strain increases beyond the elastic limit, plasticity sets in and, iteratively, stress smoothly rounds off until material yielding, corresponding to a discontinuous stress drop, and then increases again.

One goal of the existing theories of plasticity is to provide constitutive equations which account for this non linear macroscopic behaviour. To this end a hypothesis is usually made that it is possible to provide a local and instantaneous representation of the material state. This is done through the introduction of an array of (scalar and rank two-tensorial) variables $\{\xi\}$ in addiction to stress (or strain) and temperature, called *internal variables*. The corresponding additional constitutive equations are provided by assuming that the rate of evolution of the internal variables is also determined by the

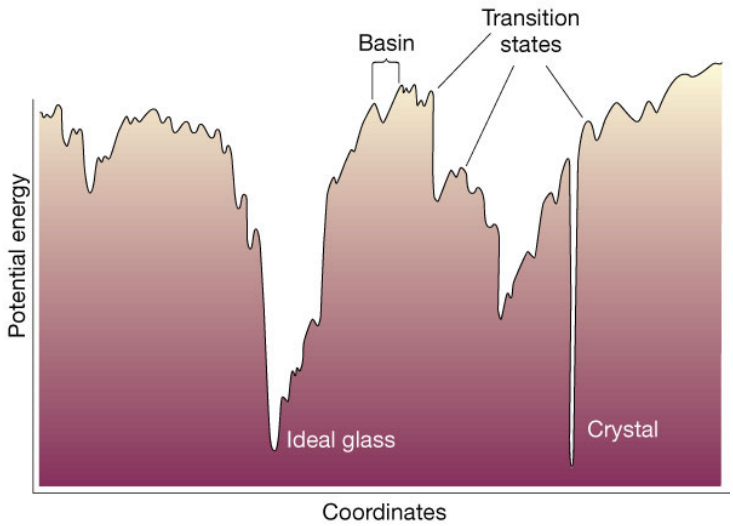

Figure 1.8: Schematization of the potential energy landscape in a one dimensional configuration space. In particular, examples of ideal glass and crystal-like minima are indicated, together with "basins" and local minima corresponding to transition states.

internal state in some way:

$$\dot{\xi_\alpha} = g_\alpha(\sigma_{ik}, T, \xi) \tag{1.35}$$

These are rate equations, which reflect the assumed rate sensitivity of the inelastic behaviour.

A number of models attempting to provide this kind of dynamical equations (e.g. activation theories, dynamics of the local stress field, dynamics of the stress distribution) has been recently reviewed in [24]. Many of these models rely on the notion of the so called *potential energy landscape* (PEL) [25], i.e. a multidimensional topographic map of the total potential energy in the configuration space of the N particle system $U(\mathbf{r}_1 \dots \mathbf{r}_N)$. A simplified illustration of this map is shown in fig. 1.8.

The potential energy landscape is characterized by its distribution of energy maxima, minima and saddle points, it defines the system dynamics and determines the system properties. Shear deformations induce changes in the PEL, and the phenomenon of yielding can be related to mechanical instabilities [26, 27].

Chapter 2

Numerical simulations of polymers

2.1 Molecular dynamics

Computer simulations are an invaluable tool for the investigation of many-body systems. They allow numerical "gedanken experiments" to be carried out, using models that approximate real physical systems. Providing essentially exact results for problems which would be otherwise soluble only by approximate methods, simulations represent an efficient test to theories. In addiction, the comparison of results obtained from simulations with those of real experiments, provide a test of the models used. On the other hand if the model proves good, it can then be used to support experiments and the interpretation of experimental results.

In this work the numerical method of classical molecular dynamics (MD) will be used. It consists in the explicit solution of the equations of motion which govern the time evolution of a model system. The model is entirely specified by the interactions between the constituent particles. Once fixed the interaction potential $U(\{\mathbf{q}_i\})$ as a function of the generalized coordinates of the system, the time evolution is described by the Hamilton equations:

$$\dot{\mathbf{q}}_i = \frac{\partial \mathcal{H}}{\partial \mathbf{p}_i}, \qquad \dot{\mathbf{p}}_i = -\frac{\partial \mathcal{H}}{\partial \mathbf{q}_i} \tag{2.1}$$

where $\{\mathbf{p}_i\}$ are the conjugate momenta of the coordinates, and $\mathcal{H}(X = \{\mathbf{q}_i, \mathbf{p}_i\})$ is the Hamiltonian. Solving these equations means computing a trajectory in the region of phase space defined by $\mathcal{H}(X) = E$, where E is the conserved energy of the system. Under the assumption of ergodicity, the phase space vectors belonging to this trajectory correspond to configurations extracted

from a microcanonical ensemble with energy E. Molecular dynamics generate a set of these configurations, via an *integrator* algorithm which solves equations 2.1 at discrete times which are multiples of a chosen *timestep* Δt. Starting from an initial configuration x_0, the integrator is iteratively used to generate the M successive $x_{n\Delta t}$, with $n = 1, \ldots, M$, through which ensemble averages A of any quantity $a(x)$ are computed:

$$A = \frac{1}{M} \sum_{n=1}^{M} a(x_{n\Delta t}) \tag{2.2}$$

The great advantage of using MD simulations is thus that they provide equilibrium averages and dynamical information simultaneously, the only downside being that results will be just as good as the model used.

Simulation code

The simulation code used in this work is LAMMPS (Large-scale Atomic/Molecular Massively Parallel Simulator) [28]. It is a classical molecular dynamics code which can be used as a parallel particle simulator at the atomic, meso, or continuum scale, including potentials for solid state, soft matter, coarse grained and mesoscopic systems. LAMMPS is distributed as an open source code. All the documentation about the algorithms implemented in the code can be found at `http://lammps.sandia.gov/doc/Manual.html`.

2.2 The NPT ensemble

Despite the Hamiltonian nature of equations 2.1, and their direct physical interpretation, the microcanonical ensemble is not always the most convenient one to be used in simulations. Since experiments are usually performed under conditions of constant number of particles N, temperature T and volume V or pressure P, the possibility of performing simulations in the corresponding ensembles is appealing.

The conditions of constant N, T and V are those of the canonical ensemble. While Hamilton equations eq. (2.1) generate the microcanonical ensemble as a consequence of total energy conservation, in the canonical ensemble energy can fluctuate. Energy fluctuations imply the Boltzmann distribution $\exp[\mathcal{H}(\mathbf{p}, \mathbf{q})/k_B T]$ of configurations, due to coupling of the system to an external thermal reservoir. In MD simulations this coupling can be included and reproduced via the *Nosé-Hoover extended phase space* technique [29, 30]. It consists in the introduction of an additional dynamical

variable s, with conjugate momentum p_s, which mimics a thermostat forcing the instantaneous temperature estimator

$$\mathcal{T} = \frac{1}{3Nk_B} \sum_{i=1}^{N} \frac{|\mathbf{p}_i|^2}{m_i} \tag{2.3}$$

to assume the value of the external temperature T, through a friction force which rescales the velocities of particles. The Nosé Hamiltonian for a system with physical coordinates $\{\mathbf{r}_1, \ldots, \mathbf{r}_N\}$ and momenta $\{\mathbf{p}_1, \ldots, \mathbf{p}_N\}$ is

$$\mathcal{H}_N = \sum_{i=1}^{N} \frac{|\mathbf{p}_i|^2}{m_i s^2} + U(\mathbf{r}_1 \ldots \mathbf{r}_N) + \frac{p_s^2}{2Q} + (3N+1)k_B T \ln s \tag{2.4}$$

where Q is the parameter that determines the time scale on which the thermostat acts. The equations of motion obtained from this Hamiltonian are then transformed via the Hoover non-canonical change of variable in the following set of equations

$$\dot{\mathbf{r}}_i = \frac{\mathbf{p}'_i}{m_i} \tag{2.5}$$

$$\dot{\mathbf{p}}'_i = \mathbf{F}_i - \frac{p_\eta}{Q}\mathbf{p}_i \tag{2.6}$$

$$\dot{\eta} = \frac{p_\eta}{Q} \tag{2.7}$$

$$\dot{p_\eta} = 3Nk_B(\mathcal{T} - T) \tag{2.8}$$

where

$$\mathbf{p}'_i = \frac{\mathbf{p}_i}{s}, \qquad dt' = \frac{dt}{s}, \qquad \frac{1}{s}\frac{ds}{dt'} = \frac{d\eta}{dt'}, \qquad p_s = p_\eta \tag{2.9}$$

Notice that the second term of eq. (2.6) has the form of a friction force, whose time evolution is driven by the difference $\mathcal{T} - T$ in eq. (2.8).

This method can be expanded to the situation in which, together with number of particles and temperature, it is pressure to be constant instead of volume. These conditions are the standard of many condensed phase experiments, and constitute the isobaric-isothermal NPT ensemble. The system must here be coupled to an external isotropic piston (barostat) that compresses or expands the system in response to fluctuations of the instantaneous internal pressure, in order to keep the latter equal in average to the

externally applied pressure. The instantaneous internal pressure is given by the estimator

$$\mathcal{P} = \frac{1}{3V} \sum_{i=1}^{N} \left[\frac{\mathbf{p}_i^2}{m_i} + \mathbf{r}_i \cdot \mathbf{F}_i \right] \tag{2.10}$$

as the result of the total force exerted by particles on the walls of the container. In order to reproduce the volume fluctuations induced by the piston (compressions and expansions), volume is introduced in the expanded phase space as an independent dynamical variable, together with its conjugate momentum [31]. The equations of motion used in LAMMPS are build up via the combination of the method of Nosé-Hoover chains for thermostatting [32] and the Martyna-Tobias-Klein (MTK) [33] method for barostatting. The physics involved is the same as in the Nosé-Hoover equations of motion, and we refer to [34] for more technical details.

It is worth reporting the chosen rate of temperature relaxation T_{damp} for the thermostat (Q in eq. (2.5)) and pressure relaxation P_{damp} for the piston, since too small values cause high fluctuations, whereas too large values correspond to very long relaxation (and so waiting) times. The most convenient values are found to be

$$T_{damp} = 100 \cdot \Delta t \tag{2.11}$$

$$P_{damp} = 10000 \cdot \Delta t \tag{2.12}$$

where Δt is the timestep of the simulation.

2.3 Equations of motion

Once the equations of motion are fixed, which describe the time evolution of the system, an integrator must be used to provide their solution at each timestep Δt. The integrator used in this work is the time reversible *velocity Verlet* algorithm [35]. Consider a set of coordinates $\{\mathbf{r}_i\}$. If Δt is chosen to be reasonably small, a Taylor expansion can be used up to the second order to obtain

$$\mathbf{r}_i\left(t + \Delta t\right) \approx \mathbf{r}_i\left(t\right) + \Delta t \mathbf{v}_i\left(t\right) + \frac{\Delta t^2}{2m_i} \mathbf{F}_i(t) \tag{2.13}$$

where $\mathbf{v}_i = \dot{\mathbf{r}}_i$ and $\mathbf{F}_i = m_i \ddot{\mathbf{r}}_i$. The same expansion can be made starting from $\mathbf{r}_i(t + \Delta t)$ and considering the evolution backwards in time

$$\mathbf{r}_i\left(t\right) \approx \mathbf{r}_i\left(t + \Delta t\right) - \Delta t \mathbf{v}_i\left(t + \Delta t\right) + \frac{\Delta t^2}{2m_i} \mathbf{F}_i(t + \Delta t) \tag{2.14}$$

Then, substituting eq. (2.14) into eq. (2.13) yields

$$\mathbf{v}_i\left(t+\Delta t\right) \approx \mathbf{v}_i\left(t\right) + \frac{\Delta t}{2m_i}\left[\mathbf{F}_i(t) + \mathbf{F}_i(t+\Delta t)\right] \tag{2.15}$$

Thus, given the initial conditions $\{\mathbf{r}_i(0), \mathbf{v}_i(0)\}$, the algorithm computes $\mathbf{F}_i(0)$ from the interaction potentials, and makes use of eq. (2.13) to obtain $\mathbf{r}_i\left(\Delta t\right)$. The new positions give $\mathbf{F}_i\left(\Delta t\right)$, which is substituted in eq. (2.15) in order to obtain $\mathbf{v}_i\left(\Delta t\right)$. The algorithm is then iterated starting from $\{\mathbf{r}_i(\Delta t), \mathbf{v}_i(\Delta t)\}$.

This scheme allows to evolve positions and velocities simultaneously. The velocity Verlet algorithm gives an error on positions and velocity of order Δt^2, but its simplicity and property of time reversibility make it one of the most attractive integrators up to date.

2.4 Periodic boundary conditions

Simulations of bulk systems require that surface effects are negligible. In any system, if N is the total number of particles, the corresponding number of particles located at the surface scales as $N^{2/3}$. In typical atomic liquid samples N is of order 10^{21} so that the fraction of atoms at the surface is negligible, whereas in molecular dynamics, a limited number of particles can be simulated. For instance the simulations carried out in this work involve $N = 4000$ particles, so that surface effects may be taken into account.

The problem can be overcome by implementing periodic boundary conditions. This is done by enclosing all the particles in a simulation box, which is then virtually replicated throughout space in an infinite lattice. A schematic 2D representation of this situation is shown in fig. 2.1. The replicas of the box are called *image* boxes, containing *image* particles. As a particle moves in the central box, its periodic images move in exactly the same way in each of the image boxes. This means that if the particle leaves the central box, one of its images will enter through the opposite face, so that number density in the central box is conserved. In this way particles are insensitive to the boundaries of the simulation box and surfaces effects are removed.

For our study of the mechanical response to simple shear deformation, the most suitable shape of the simulation box is a triclinic parallelepiped. Therefore we define the simulation box through the matrix

$$\mathbf{h} = \begin{pmatrix} L_x & xy & xz \\ 0 & L_y & yz \\ 0 & 0 & L_z \end{pmatrix} \tag{2.16}$$

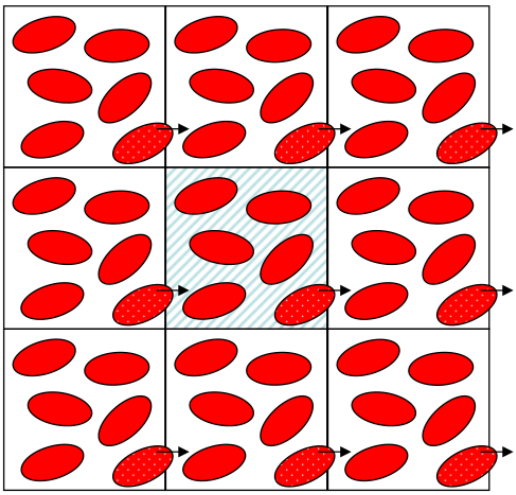

Figure 2.1: Schematic two dimensional representation of the infinite lattice build up from the repetition in space of the simulation box (shaded). Periodic boundary conditions allow a particle leaving the box to be replaced by one of its images entering from the opposite side.

where L_x, L_y and L_z are the box sides and xy, xz and yz are called the *tilt factors*. A shear deformation of a cubic box along the xy direction is simply obtained by imposing $L_x = L_y = L_z = L$, $xz = yz = 0$ and $xy \neq 0$.

Periodic boundary conditions are implemented in the following way. In any procedure which requires the computation of reciprocal distances (evaluation of forces, spatial distributions of particles, computation of order parameters etc.) every distance $\mathbf{r}_{ij}$ between the i-th and j-th particles first undergoes the sequence of transformations [36]

$$\mathbf{s}_{ij} = \mathbf{h}^{-1} \cdot \mathbf{r}_{ij} \tag{2.17}$$

$$|\mathbf{s}'_{ij}| = |\mathbf{s}_{ij}| - RINT\left(|\mathbf{s}_{ij}|\right) \tag{2.18}$$

$$\mathbf{r}'_{ij} = \mathbf{h} \cdot \mathbf{s}'_{ij} \tag{2.19}$$

where $RINT(x)$ is the function that gives the nearest integer to x. In the evaluation of inter-particle forces, this criterium corresponds to the *minimum image convention*, according to which each particle interacts only with those lying in a region of the same size and shape of the simulation box, centred on that particle. This criterium is applicable only to systems with enough short-ranged interaction potentials.

2.5 Polymer model

The model system studied in this work is the so called *soft bead-spring* model. It consists of N_c chains of M beads. Each bead (monomer) is the coarse-grained representation of the repeated unit of the polymer, which is assumed to be electrically neutral.

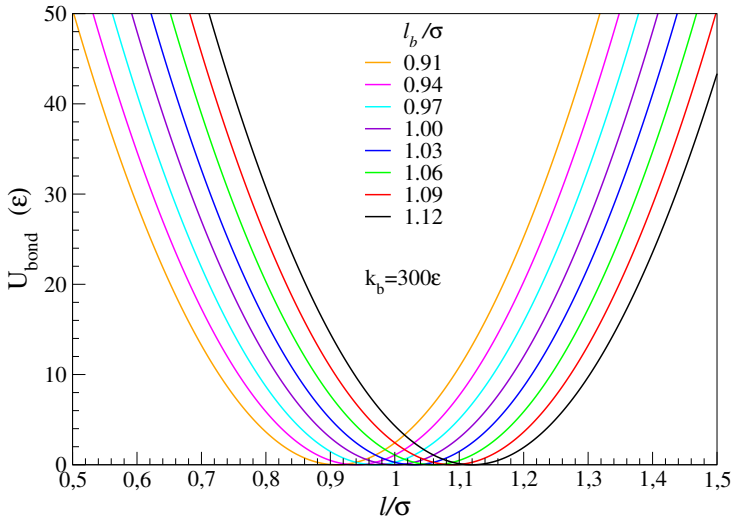

Figure 2.2: Plot of the bond interaction potential in Lennard-Jones units. The bond rigidity is fixed at $k_b = 300\varepsilon$, while different equilibrium bond lengths are studied.

The interaction between two bonded monomers along a chain, placed at a distance l from each other, is approximated via a harmonic potential of the form:

$$U_{bond}(l) = k_b (l - l_b)^2 \tag{2.20}$$

where l_b is the equilibrium bond length and k_b is the bond rigidity (fig. 2.2). Breaking of bonds and formation of new ones are not allowed in this model.

All the other, non-bonded monomers interact in pairs via a truncated and shifted Lennard-Jones potential (fig. 2.3):

$$U_{LJ}(r) = \begin{cases} 4\varepsilon \left[\left(\frac{\sigma}{r}\right)^{12} - \left(\frac{\sigma}{r}\right)^{6} \right] - C & for\ r \leq r_c \\ 0 & for\ r > r_c \end{cases} \tag{2.21}$$

where r is the reciprocal distance, σ is the zero crossing point of the potential

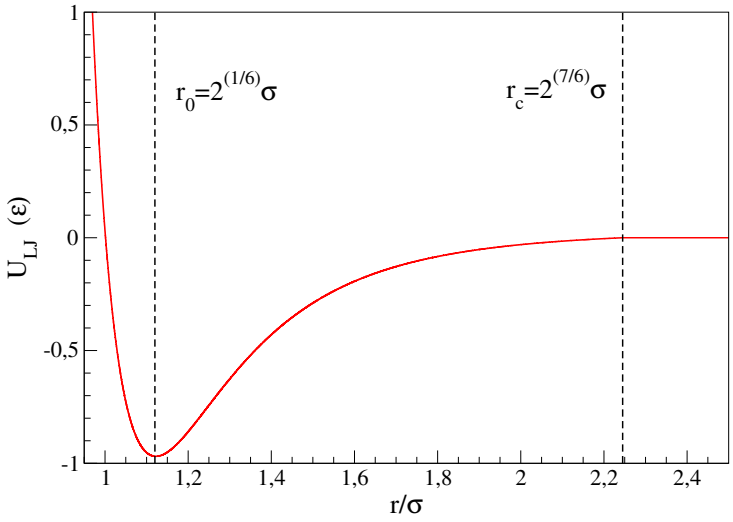

Figure 2.3: Plot of the Lennard-Jones potential determining the interaction between pairs of non-bonded monomers. The units of length σ corresponds to the zero crossing point. The potential has a minimum in $r_0 = 2^{1/6}\sigma$ and is truncated and shifted to zero at $r_c = 2^{7/6}\sigma$.

and

$$C = 4\varepsilon \left[\left(\frac{\sigma}{r_c} \right)^{12} - \left(\frac{\sigma}{r_c} \right)^{6} \right] \tag{2.22}$$

is the energy constant term used to shift to zero the potential at the cut-off radius r_c.

A negative well is found at $r_0 = 2^{1/6}\sigma$, so that r_0 will be often addressed as the *bead diameter* or *monomer diameter*. The well has depth $\varepsilon - C$ and it is responsible of cohesion in the condensed phase. The Lennard-Jones potential gives account for the Pauli repulsion between electron clouds at short distances ($r < r_0$), and for the attractive (van der Waals- or London-like) contribution at long ranges ($r > r_0$). The potential is truncated and shifted to zero at $r_c = 2^{7/6}\sigma$, a cut-off distance at which the non-shifted potential would be about 3% of the absolute value of its minimum ε. This allows saving computational time within the minimum image convention (see section 2.4), while affecting weakly enough the thermodynamic properties.

In order to cover the range of both fully- and semi-flexible polymers, the model includes also a bending angle interaction between pairs of chemical bonds, through a potential of the form:

$$U_{bending} = k_\theta \left(1 + \cos\theta_b\right) \tag{2.23}$$

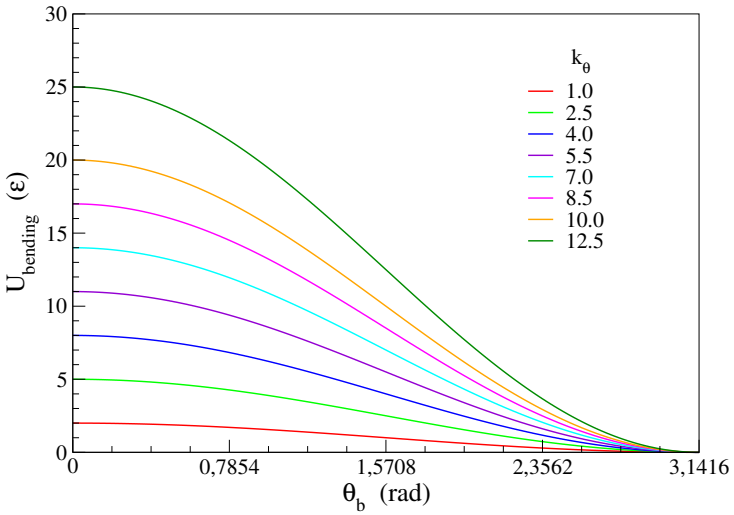

Figure 2.4: Plot of the bending angle interaction potential as function of the angle θ_b enclosed by two subsequent bonds along the polymer chain. The same plot for different values of bending stiffness k_θ is reported.

where k_θ is the bending (or chain) stiffness and θ_b is the angle enclosed by two subsequent bonds along the polymer chain (fig. 2.4). This potential has a minimum in $\theta_b = 180°$. This means that the two bonds tend to align, with a strength proportional to bending stiffness.

2.6 Reduced units

For systems consisting of only one type of particle, it is convenient to use the mass m of the particle as a fundamental unit, by setting $m = 1$. If particles interact by simple pair potentials such as the Lennard-Jones (eq. (2.21)), this approach can be extended further. The parameters of the potential, namely ε and σ, can be used as fundamental units of energy and length, respectively. From these definitions, units of other quantities such as pressure, time, momentum etc. follow directly. Some of the advantages of using reduced units are:

- the possibility to work with numerical values of order unity, instead of the very small values usually associated with the atomic or molecular scale;
- the simplification of equations of motion, as the parameters defining the model are absorbed into the units;

Table 2.1: System of units used in MD simulations of Lennard-Jones particles. The corresponding values of ε, σ and m of liquid argon [37] are also reported.

Physical quantity	Unit	Value for Ar
length	σ	$3.4 \cdot 10^{-10}\, m$
energy	ε	$1.65 \cdot 10^{-21}\, J$
mass	m	$6.69 \cdot 10^{-26}\, Kg$
time	$(\sigma^2 m/\varepsilon)^{1/2}$	$2.17 \cdot 10^{-12}\, s$
velocity	(ε/m)	$1.57 \cdot 10^{2}\, m/s$
force	ε/σ	$4.85 \cdot 10^{-12}\, N$
pressure	ε/σ^3	$4.20 \cdot 10^{7}\, N/m^2$
temperature	ε/k_B	$120\, K$

- the scalable nature of the results, which can be fitted to a whole class of systems described by the same model.

It is always possible to remap Lennard-Jones (LJ) units into real units. A list of the fundamental physical quantities, along with the corresponding LJ units are reported in table 2.1. The corresponding values for liquid Argon [37] are also reported.

In the rest of this work, all physical quantities are reported in reduced LJ units.

2.7 Simulation protocol

The simulation protocol used in this work is highly modular. Each part of the protocol is here described separately.

2.7.1 Preparation

In molecular dynamics, it is necessary to design a starting configuration for each sample of the system under study. The most suitable way to initialize the sample is made up of the following steps:

- The initial density $\rho_i = \frac{N}{V}$ is fixed and the simulation box is generated with a cubic shape of volume V and side $L = V^{\frac{1}{3}}$;
- The first monomer of each chain is placed at randomly generated coordinates inside the box;
- For each of the first monomers, the successive bonded monomer in the chain is generated, at a random point included in a sphere of fixed radius, with the constraint of a minimum distance between non-bonded monomers is also imposed. The procedure is iterated for the successive monomers of each chain until all the monomers are placed in the box.

The configuration obtained through these steps can still be unphysical, principally due to overlapping of bonds. In order to overcome this problem, a minimization of the total potential energy

$$U\left(\mathbf{r}_1 \dots \mathbf{r}_N\right) = \sum_{i,j} U_{LJ}(\mathbf{r}_{ij}) + \sum_{i,j} U_{bond}(\mathbf{r}_{ij}) + \sum_{i,j,k} U_{bending}(\mathbf{r}_i, \mathbf{r}_j, \mathbf{r}_k) \quad (2.24)$$

is performed via the conjugate gradient method. The minimization, which changes the coordinates of monomers forcing the system in the nearest local minimum of the total potential energy, is performed first with a smaller bond rigidity k_b in eq. (2.20). The resultant increased looseness of bonds allows for the disentanglement of possibly overlapped bonds. The minimization is then repeated with the appropriate bond rigidity. The configuration obtained at this point has the adequate physical features.

2.7.2 Equilibration

In order to remove the dependence of physical quantities on the choice of the initial configuration, an equilibration is performed. The equilibration of a system consists in making it evolve in time until it comes to a new equilibrium state point, where all memory of the initial configuration is lost.

To this end, first each monomer is assigned an initial velocity, the Cartesian components of which are randomly extracted from a Gaussian distribution

$$f(v_i) = \sqrt{\frac{m}{2\pi k_B T_I}} \exp\left(-\frac{m v_i^2}{2 k_B T_I}\right) \quad (2.25)$$

where $i = x, y, z$, and T_I is the chosen initial temperature. Then a molecular dynamics simulation is run in the NPT ensemble, i.e. fixing also pressure.

The complete loss of memory of the initial configuration is assured only if the longest relaxation time of the system is exceeded. This is the time τ_{ee}

(eq. (1.20)) of decorrelation of the end-to-end vector $\mathbf{R}_{ee}(t)$, so that the corresponding autocorrelation function $C_{ee}(t)$ is monitored during equilibration. An example of this monitoring is reported in appendix A, together with the monitored thermodynamic quantities (volume, temperature and pressure).

2.7.3 Cooling

Starting from the configurations obtained via the equilibration procedure, the samples are cooled down. Temperature is lowered from its initial value T_I used for the equilibration, at the finite quench rate $|\dot{T}| = 2 \times 10^{-6}$ until it reaches the final value $T_F = 10^{-3}$ (which is about $0.1K$ for Argon, see table 2.1). Examples of the monitored temperature during cooling is reported in appendix A.

As explained in section 1.1, the ability of a system to either nucleate or keep amorphous depends on the cooling rate. The slower a system is cooled down, the more variegated is the set of morphologies formed. The chosen $|\dot{T}|$ is just a good compromise between the required computational time for quenching and the achievable diversity in the response to cooling (section 3.4). On the other hand, the choice of final temperature $T_F \simeq 0$ is made in order to remove the effects of thermal vibrations in the study of the mechanical response of the solids (chapter 4).

2.7.4 Deformation

Simple shear deformation is applied to the solids at exactly $T = 0$, along each of the three shear direction (xy, xz, yz) independently, via the athermal quasi-static (AQS) protocol [24]. Starting with a cubic simulation box, i.e. with sides set at $L_x = L_y = L_z = L$ and tilt factors set at $xy = xz = yz = 0$ in eq. (2.16), in the AQS protocol the following two steps are iterated:

- The tilt factor corresponding to the chosen shear direction is incremented of $0.001\% \cdot L$. The coordinates of all the monomers are then remapped in the new box. This corresponds to affine deformation, i.e. the displacement of monomers matches the macroscopic deformation of the box.

- Since the new positions of the monomers after remapping do not belong to an equilibrium configuration, a minimization of the total potential energy is performed, this time via the steepest descent algorithm. Conceptually, this minimization corresponds to allowing the system to relax to the nearest local minimum of the total potential energy, where the resultant of the forces on each monomer is zero. This relaxation of

monomers towards new positions corresponds to the non-affine contribution to deformation.

The two steps of the AQS protocol are iterated until the chosen tilt factor reaches the value of $15\% \cdot L$.

In general, the mechanical behaviour of a system is determined by the coupled effects of thermal vibrations around a local minimum of the energy landscape, which is modified upon deformation, and of hopping between these local minima, to which plastic events are associated. As the contribution of thermal vibrations is trivial, it is convenient to remove it by taking the zero temperature limit. Under T_g the structural relaxation time diverges, so that simulating the time evolution of the system towards the nearest local energy minimum would imply either un-physically fast dynamics or too much long computational time. The minimization procedure allows to avoid this problem by directly forcing the system to the configuration corresponding to the nearest minimum of the energy landscape.

2.8 Data analysis

Analyses are carried out on the LAMMPS output files containing all the information about the system configurations (positions and velocities of all the monomers) at some chosen multiple of the simulation timestep. The analysis program, which is written in C, takes in input these files together with two additional text files: one containing the timestep Δt, the multiple of Δt at which system configurations are stored, the number of types of monomers, the number of chains N_c and the number of monomers per chain M; the other one containing information about which analysis function is to be used and the corresponding parameters (e.g. number of configuration files to be analysed, number of bins for histograms, etc.). For each physical quantity of interest the corresponding analysis function can be activated.

A description of the relevant functions used in this work is reported in section 3.2. The analysis program has been created and is constantly updated by the research group lead by the Supervisor of this work.

Chapter 3

Static properties in the liquid and solid phases

3.1 Introduction

The polymer model adopted in this work is comparable to the Kremer-Grest bead-spring model [38], which describes the polymer as a chain of M beads connected by $M+1$ bonds, made semiflexible through the inclusion of bending (chain) stiffness (eq. (2.23)). The presence, in this model, of a competition between the two inherent length scales of intra-molecular (bond length l_b) and inter-molecular (monomer diameter r_0) interactions (see section 2.5) has been already pointed out in the literature [39]. This competition, which is due to connectivity, profoundly affects the ability of a system to become solid upon cooling, and of either keep completely amorphous or to partially crystallize in the solid phase. Similar effects have been observed in simulations of cooled down samples with fixed bond length but different bending stiffness [40], another fundamental parameter determining the connectivity of the polymer. The effects of both bond length and chain stiffness are the object of the systematic study presented in this part of the work.

The effects of connectivity are investigated first in the liquid phase of the model (section 3.3). Then, we cool down the liquids at a finite quench rate in order to obtained solids at low temperature, namely $T = 10^{-3}$. The same characterization carried out for the liquids is repeated for the corresponding solids (section 3.4). This allows for a better understanding of the structural features of the solids, which is preliminary to the study of their mechanical response to deformations.

3.2 Quantities of interest

In this section the quantities of interest are defined, which describe the static properties of polymer liquids and solids. To each of these quantities corresponds a function in the data analysis program used in this work (see section 2.8). A brief description of how these functions are computed is also given.

3.2.1 Radial pair distribution function $g(r)$

In a system of non interacting particles, the number of particles included in a spherical shell of thickness dr, at a distance r from a reference one is $4\pi\rho r^2 dr$, where the number density of the system ρ is uniform. When particles interact, in general the number density depends on the distance r, so that it can be written in the following way:

$$\rho(r) = \rho g(r) \tag{3.1}$$

where ρ is the average density and

$$g(r) = \frac{1}{N(N-1)} \sum_{i}^{N} \sum_{j \neq i}^{N-1} \delta(|\mathbf{r}_{ij}| - r) \tag{3.2}$$

is the radial pair distribution function for a system of N particles. The factor $N(N-1)$ is the total number of pairs and $|\mathbf{r}_{ij}| = |\mathbf{r}_i - \mathbf{r}_j|$ is the distance between the i-th and j-th particles. If a reference particle is placed in the origin O, then $4\pi\rho g(r) r^2 dr$ is the probability density of finding another particle at a distance between r and $r + dr$ from the reference one (see fig. 3.1). The $g(r)$ function is thus a basic quantity in the description of system structure.

The algorithm used to compute $g(r)$ calculates, for a number of different configurations of the system, with equal temperature and pressure, the distances between all the particle pairs and bins them into a histogram $I\,[g(r)]$ of N_b bins of width Δr; $g(r)$ is then extrapolated from

$$I\,[g(r)] = 4\pi\rho g(r) r^2 \Delta r \tag{3.3}$$

Since a cubic simulation box of side L, with periodic boundary conditions is used in the study of static properties, $g(r)$ is computed to a maximum distance $N_b \Delta r = \frac{L}{2}$, to avoid double counting. This leads to the final form

$$g(r) = I\,[g(r)]\, \frac{2N_b^3}{\pi N} \left(\frac{\Delta r}{r}\right)^2 \tag{3.4}$$

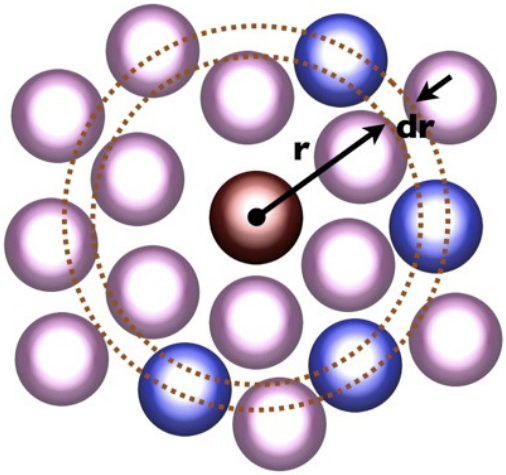

Figure 3.1: Bidimensional representation of a spherical shell of inner radius r and thickness dr, taken from the position of a reference particle (the central in brown). The particles (in blue) in this shell of neighbours are counted for computation of the radial pair distribution function $g(r)$.

This quantity is eventually averaged on the configurations sampled during the time evolution of the system, in order to reproduce a time average.

Since relative maxima of this function correspond to larger numbers of particles, the positions at which they begin and end are identified as the boundaries of coordination shells. At large distances these spatial correlations are lost and any liquid appears isotropic with uniform density ρ, so that $g(r \to \infty) \longrightarrow 1$.

3.2.2 Angular distribution function $ADF\,(\Delta r, \cos\phi)$

The angular equivalent of the radial pair distribution function $g(r)$ is the angular distribution function $ADF\,(\Delta r, \cos\phi)$. This function gives the probability density of finding a triplet of monomers, denoted by indexes i, j and l, to enclose an angle included in $[\cos\phi,\ \cos\phi + \Delta(\cos\phi)]$, with the constraint that the distances of the j-th and l-th monomers from the i-th one are included in a radial shell $\Delta r = [r_{min},\ r_{max}]$, namely

$$(\cos\phi)_{ilj} = \frac{\mathbf{r}_{li} \cdot \mathbf{r}_{ji}}{|\mathbf{r}_{li}|\,|\mathbf{r}_{ji}|} \qquad |\mathbf{r}_{li}|\,, |\mathbf{r}_{ji}| \in \Delta r \tag{3.5}$$

where $\mathbf{r}_{li} = \mathbf{r}_l - \mathbf{r}_i$ (fig. 3.2).

The distribution is obtained by binning the values of $\cos\phi$ for all the ilj triplets of given configuration, in a histogram $I\,[\Delta r,\ \cos\phi]$ of N_b bins of width

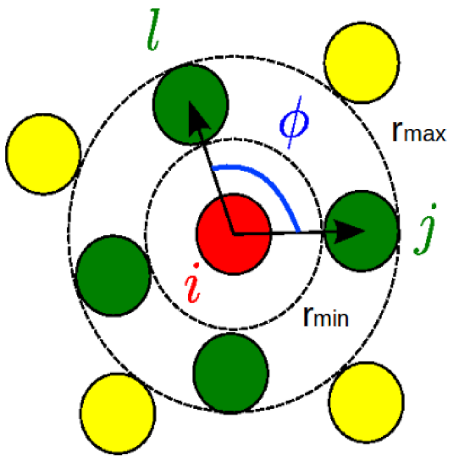

Figure 3.2: Schematic illustration of the angle involved in the computation of the anglular distribution function. First the central i-th monomer (in red) and the boundaries $\Delta r = [r_{min}, \quad r_{max}]$ (dashed lines) of the target shell are fixed. For every pair of monomers belonging to this shell (for instance the l-th and j-th in green), the angle ϕ formed by this pair and the central monomer is then computed.

$\Delta(\cos\phi)$ and normalizing by the total number of triplets found. Average on all the analysed configurations is carried out.

The interval Δr can be conveniently chosen as that corresponding to the first r_I or second r_{II} coordination shell. These can be extrapolated from the $g(r)$ function, taking the intervals of r in which respectively the first and the second maximum lies. In this way a detailed description of the local disposition of first and second neighbours is obtained. We stop at the analysis of the shell of second neighbours because for coordination shells of higher order, spatial correlations rapidly disappear, surviving only at increasingly small angles due to overlapping of terminal monomers of the triplets.

3.2.3 Bond angle distribution function $P(\cos\theta_b)$

The geometry of chains is also an important feature of the model, and it is directly affected by the control parameters l_b and k_θ. In order to characterize it, the distribution of angles θ_b enclosed by two bonds, i.e. by triplets of bonded monomers subsequent along the chain, is computed.

The distribution is build up by an algorithm which, for every triplet of

bonded monomers, denoted by indexes $i-1$, i and $i+1$, calculates the quantity

$$(\cos\theta_b)_i = -\frac{\mathbf{b}_i \cdot \mathbf{b}_{i+1}}{|\mathbf{b}_i|\,|\mathbf{b}_{i+1}|} \tag{3.6}$$

where $\mathbf{b}_i$ is the bond vector $\mathbf{b}_i = \mathbf{r}_i - \mathbf{r}_{i-1}$. For each of the analysed configurations, the obtained values are binned in a histogram $I[\cos\theta_b]$ of N_b bins of width $\Delta(\cos\theta_b)$. The probability density of finding a triplet of bonded monomers to form an angle of cosine included between $\cos\theta_b$ and $(\cos\theta_b + \Delta(\cos\theta_b))$ is then obtained via normalization of $I[\cos\theta_b]$ by the total number of bonded triplets

$$P(\cos\theta_b) = \frac{I[\cos\theta_b]}{N_c\,(M-2)} \tag{3.7}$$

where M and N_c are respectively the number of monomers in a polymer chain, and the total number of chains. Average on the configurations is then carried out.

3.2.4 Orientational order parameters

A useful description of local and global order in amorphous systems is provided by the orientational order parameters defined in [41] in the following way. Consider the vector $\mathbf{r}_{ij}$ joining the i-th monomer to the j-th one chosen among its nearest neighbours. To this vector, a polar and an azimuthal angle, namely $\theta(\mathbf{r}_{ij})$ and $\phi(\mathbf{r}_{ij})$, are associated. The set of spherical harmonics $Y_{lm}[\theta(\mathbf{r}_{ij}), \phi(\mathbf{r}_{ij})]$ is then assigned to $\mathbf{r}_{ij}$, and it can be conveniently averaged either over the set of nearest neighbour distances from the fixed i-th monomer, in order to obtain the local quantity

$$\overline{Q}_{lm}^{local}(i) = \frac{1}{n_b(i)} \sum_{j=1}^{n_b(i)} Y_{lm}[\theta(\mathbf{r}_{ij}), \phi(\mathbf{r}_{ij})] \tag{3.8}$$

where $n_b(i)$ is the number of nearest neighbours of the i-th monomer. Or it can be averaged also on all the i-th central monomers giving the global quantity

$$\overline{Q}_{lm}^{global}(i) = \frac{1}{N_b} \sum_{i=1}^{N_b} \overline{Q}_{lm}^{local}(i) \tag{3.9}$$

where N_b is the total number of vectors like r_{ij} in the system. Starting from these two objects, one can build up the rotationally invariant combinations

$$Q_l^x = \left[\frac{4\pi}{2l+1} \sum_{m=-l}^{l} \left| \overline{Q}_{lm}^x(i) \right|^2 \right] \tag{3.10}$$

where x stands for either *'local'* or *'global'*.

Table 3.1: Orientational order parameters for random, fcc, hcp and icosahedral neighbour configurations, as computed in [42].

Configuration	Q_4^{global}	Q_6^{global}	Q_4^{local}	Q_6^{local}
Random	0.010	0.010	0.22	0.22
Fcc	0.191	0.574	0.191	0.574
Hcp	0.097	0.485	0.097	0.485
Icos	0.00	0.663	0.00	0.663

These invariants are also direction-independent for even values of l, as even-l spherical harmonics are invariant under inversion. The orientational order parameters for random configurations of nearest neighbours in polymer systems have been recently calculated in [42], together with those corresponding to ideal *fcc*, *hcp* and *icosahedral* atomic clusters. The results are reported in table 3.1.

3.3 The liquid phase

The analysis of static properties of the model in its liquid phase is carried out on systems prepared and equilibrated in the way depicted in section 2.7. The separate effects of bond length and chain stiffness on these properties are studied. First k_θ is set to zero in eq. (2.23) and simulations with systematically changed values of l_b in eq. (2.20) are performed. Analyses are carried out and, in light of the results, the most convenient value of l_b is fixed for simulations with systematic variation of $k_\theta > 0$.

Production simulations are performed in the NPT ensemble at zero pressure (details in chapter 2), while the ranges of temperature and density investigated, namely $1.2 \leq T \leq 1.6$ and $0.90 \leq \rho \leq 1.00$, are chosen in such a way to assure the state of liquid during equilibration. In order to understand the structure of these liquids, information extracted from the functions described in section 3.2 are combined.

3.3.1 Bond length

In order to investigate the influence of bond length l_b on the static properties of the liquids, analyses are carried out in a systematic manner by simulating

8 systems, each with a different value of l_b: 0.91, 0.94, 0.97, 1.00, 1.03, 1.06, 1.09, 1.12, the last being the equilibrium separation of non bonded monomers $r_0 = 1.12$ (see (2.21)). These systems are equal in all the other features, as they all consist of $N_c = 160$ chains of $M = 25$ monomers, with an initial density $\rho_i = 1.00$ and temperature $T = 1.2$.

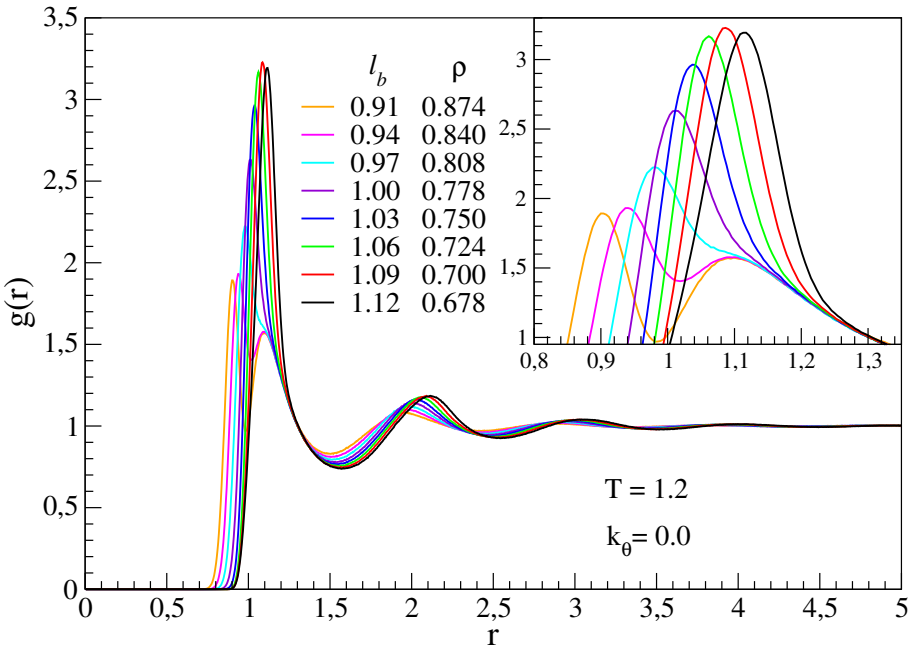

Figure 3.3: Radial distribution function of monomer pairs $g(r)$ at temperature $T = 1.2$. Systems with different bond lengths l_b are initialised with the same density $\rho_i = 1.00$ which for each sample turns to a different value ρ during equilibration. The peaks of this distribution correspond to coordination shells. In the inset only the first shell is displayed: notice the two distinct peaks resolved for small values of l_b, corresponding to contributions at l_b and r_0. The $g(r)$ tends to 1 for large r, where we find an ideal gas-like distribution with homogeneous density ρ.

In order to characterize the structure of our systems in the liquid phase, the average spatial disposition of first and second neighbours is studied.

As it can be seen from the $g(r)$, shown in fig. 3.3, for all systems the first coordination shell lies in $r_I = [0.7,\ 1.6]$. To this shell belong the two monomers bonded to the central one and other non-bonded monomers. In the inset these two contributions are clearly distinguishable for systems with small l_b, in the form of two distinct subsequent peaks of $g(r)$ centred respectively at l_b and r_0. As the value of l_b comes closer to r_0, the resolution of

these two peaks weakens until they appear joint in a single one. Among the non bonded first neighbours are found also monomers belonging to the same chain of the central one, and in particular those which are two bonds distant from it along the chain. This can be understood from the distribution func-

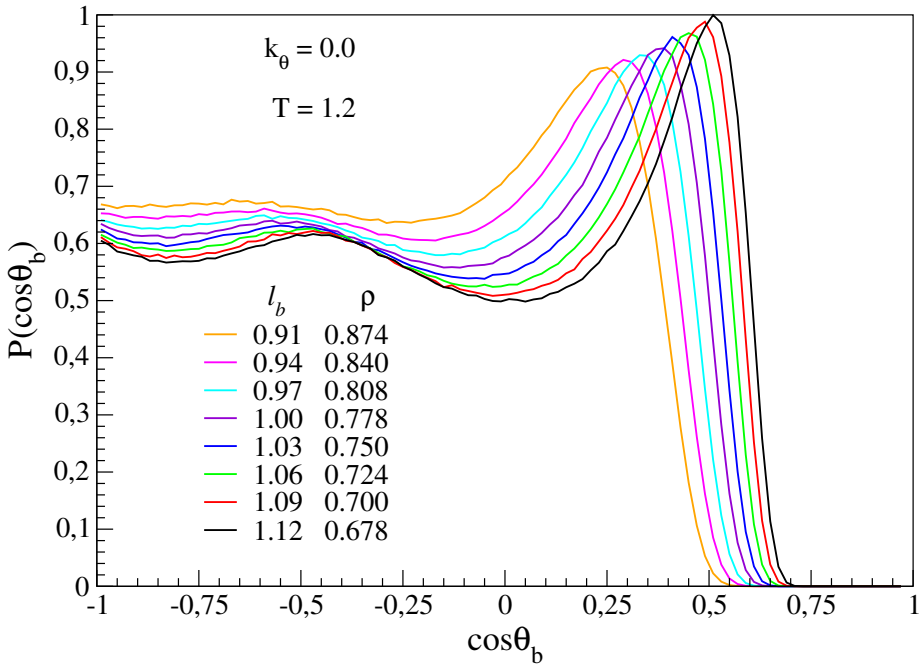

Figure 3.4: Distribution function of angles formed by triplets of subsequent bonded monomers. Most triplets are folded in such a way to keep terminal monomers at the LJ equilibrium distance ($\theta_b^1 = 59 \div 75°$). Other (less) favoured configurations are: stretched triplet ($\theta_b^2 \approx 180°$); terminal monomer being the central monomer of the next θ_b^1 triplet ($\theta_b^3 \approx \pi - \theta_b^1$). Notice that as the gap $|l_b - r_0|$ increases, $P(\cos\theta_b)$ broadens and flattens out, due to increasing disorder.

tion of bond angles $P(\cos\theta_b)$, shown in fig. 3.4. Its absolute maxima occur at bond angles θ_b^1 such that the separation between two terminal monomers of a triplet is around r_0, a distance included in the first coordination shell (for instance when $l_b = 0.91$ one has $\theta_b^1 = 75.52°$, so that, by Carnot theorem, the separation is $l_b \cdot \sqrt{2 \cdot (1 - \cos\theta_b^1)} \simeq 1.115$). Values of θ_b^1 range from $\approx 59°$ for $l_b = 1.12$, to $\approx 75°$ for $l_b = 0.91$. The other maxima of $P(\cos\theta_b)$ are found at $\theta_b^2 \approx 180°$ (two parallel subsequent bonds) and at $\theta_b^3 \approx \pi - \theta_b^1$, which corresponds to the situation in which a terminal monomer of a triplet is the central one of a next triplet forming in turn the favoured angle θ_b^1.

For all systems there is a cut-off in the bond angle distribution for small angles, due to the fact that terminal monomers of a triplet cannot interpen-

etrate. This holds also for the other angular distributions discussed in the following.

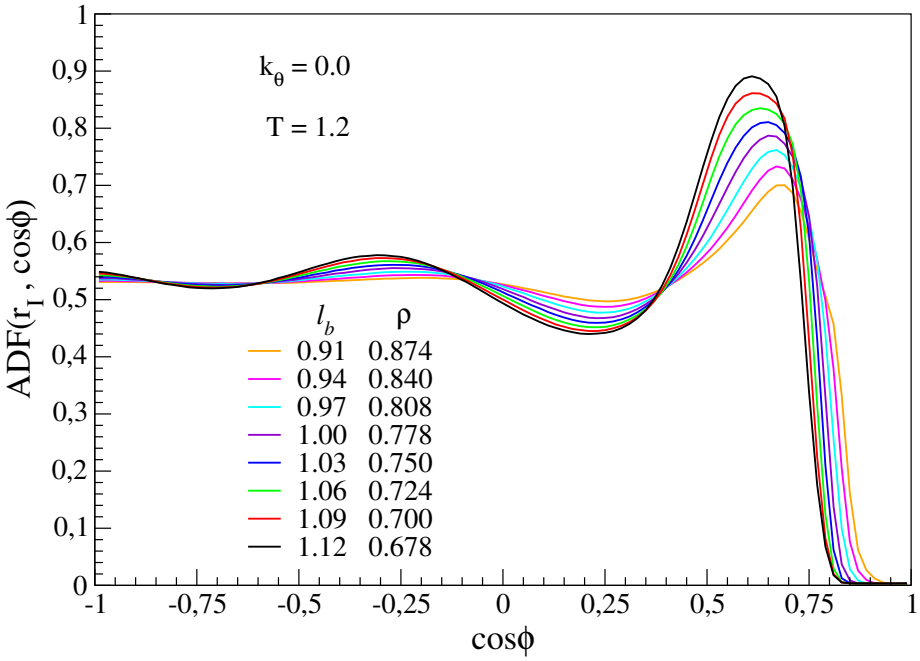

Figure 3.5: Distribution function of angles formed by triplets of first neighbour monomers. The $r_I = [0.7,\ 1.6]$ range of the first coordination shell is extrapolated from $g(r)$. The most frequent angles are found in the range $\phi = 46 \div 53°$, then $\phi = 96 \div 127°$ and $\phi \approx 180°$ for systems with large l_b. As in $P(\cos\theta_b)$, which is a subset of this distribution, also here the greater $l_b - r_0$ is, the flatter are the curves.

In order to complete the description of the first coordination shell, the angular distribution of first neighbour triplets $ADF\,(r_I, \cos\phi)$ is considered. Maxima of this function are found, as shown in fig. 3.5, in the ranges $\phi = 46 \div 53°$ (strong peaks), $\phi = 96 \div 127°$ (slighter peaks) and at $\phi \approx 180°$. There is no intuitive reason for the positions of these maxima, as they originate from rather collective aspects missing strong constraints such as that of the bond.

The second coordination shell lies in the range $r_{II} = [1.6,\ 2.5]$. The related peak of $g(r)$ is much broader than the first shell one, as positions of monomers in the second shell are much less correlated. Notice that for the same reason, the angular distribution of these monomers $ADF(r_{II}, \cos\phi)$, as shown in fig. 3.6, flattens out rather quickly for values of ϕ just greater than 90°, whereas correlations between terminal monomers in triplets forming smaller angles are still present, resulting in two peaks centred at $\phi \approx 60°$ and $\phi \approx 30°$.

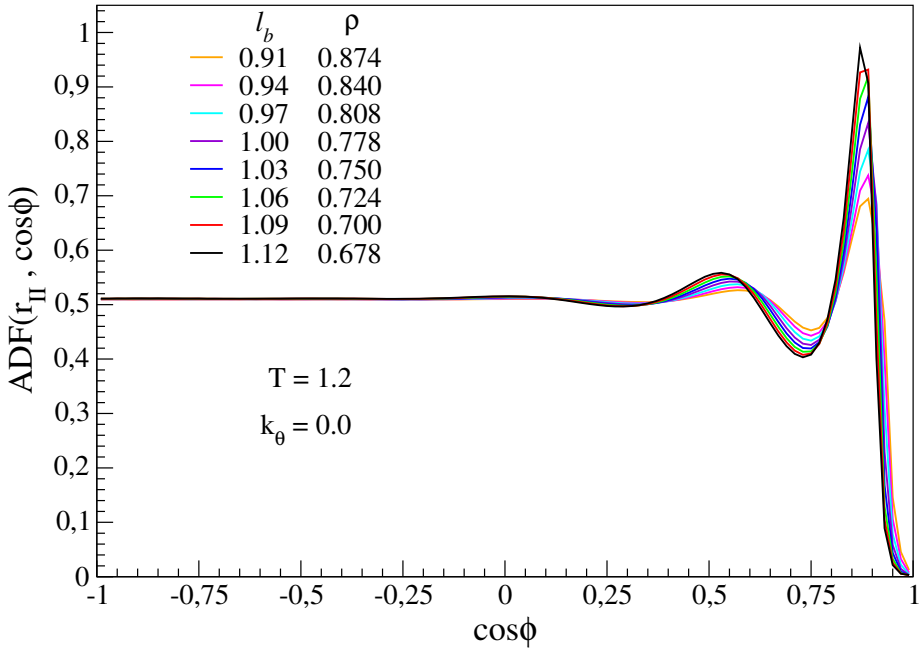

Figure 3.6: Angular distribution function of second neighbours. The second coordination shell is extrapolated from $g(r)$ to be $r_{II} = [1.6,\ 2.5]$. Spatial correlations survive only for triplets with terminal atoms close enough. As a consequence, $ADF\,(r_{II}, \cos\phi)$ is flat in the whole ϕ range, except for small angles. The favoured angles are around 30° and secondly around 60°. The disordering (flattening) effect of incommensurability between the principal scale lengths l_b and r_0 is again confirmed.

After that corresponding to the second coordination shell, the pair distribution function shows no other significant peak, and stabilizes on $g(r) = 1$, which means that at these distances, pairs are distributed as in an ideal gas, with a homogeneous density equal to the overall density of the liquid ρ. This absence of long range order is typical of polymeric liquids.

It is to remark that even in the liquid phase, the competition between the two length scales l_b and r_0 plays a role in the degree of structural order: in all the distribution functions discussed here, as the gap $|l_b - r_0|$ increases, widths of maxima increase with a consequent flattening, which is evidence of a decreasing order.

3.3.2 Chain stiffness

The effect of chain stiffness on the static properties is studied by simulating 8 systems each with a different value of k_θ: 1.0, 2.5, 4.0, 5.5, 7.0, 8.5, 10.0, and 12.5. Bond length is fixed at the value $l_b = r_0 = 1.12$. This choice is made in order to isolate the effect of chain stiffness from that of the competition between length scales.

As explained in the next section, systems with $k_\theta > 0$ undergo a variety of different solidification processes at different temperatures. In order to avoid solidification during the equilibration phase, initial temperatures and densities are selected in the following way:

$$\begin{aligned} &T = 1.2, \quad \rho_i = 1.00 \quad for \quad k_\theta < 7; \\ &T = 1.4, \quad \rho_i = 0.90 \quad for \quad 7 \leq k_\theta < 10; \\ &T = 1.6, \quad \rho_i = 0.80 \quad for \quad k_\theta \geq 10; \end{aligned}$$

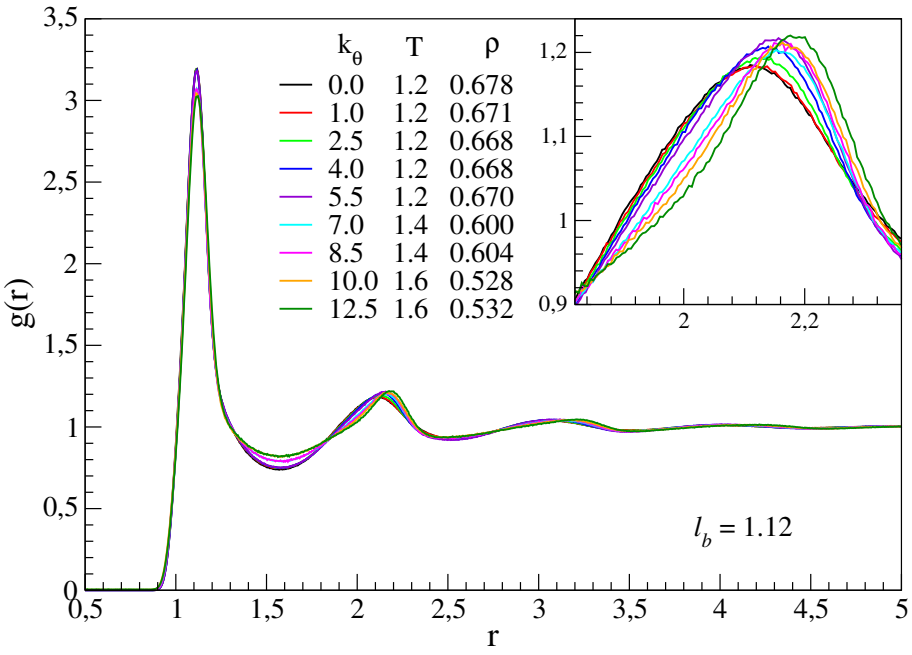

Figure 3.7: Radial pair distribution function $g(r)$ of liquids with bond length $l_b = r_0 = 1.12$ and different chain stiffness. All the sample are initialised with a certain density ρ_i, but stabilize on different values ρ during equilibration, reported in the legend. The peaks of $g(r)$, corresponding to second (see inset) and third coordination shells, are shifted to greater distances r for increasing values of k_θ. No effect on the global structure is observed.

As in the case of bond length, chain stiffness does not affect the global structure of the liquids, which appears disordered. This can be seen from fig. 3.7, in which the $g(r)$ function is shown. After a distance of about $r = 4$, the distribution flattens out on that of a uniform system of equal density ρ, and significant degree of order is present only at a very local scale, i.e. until the second coordination shell (range $r = 1.6 \div 2.5$). On this scale the effects of stiffness are small but still present: for increasing k_θ the peaks corresponding to second and third neighbours are shifted to greater r. This can be ascribed to the fact that if the stiffer chains are stretched, it is more "difficult" for monomers to pack densely.

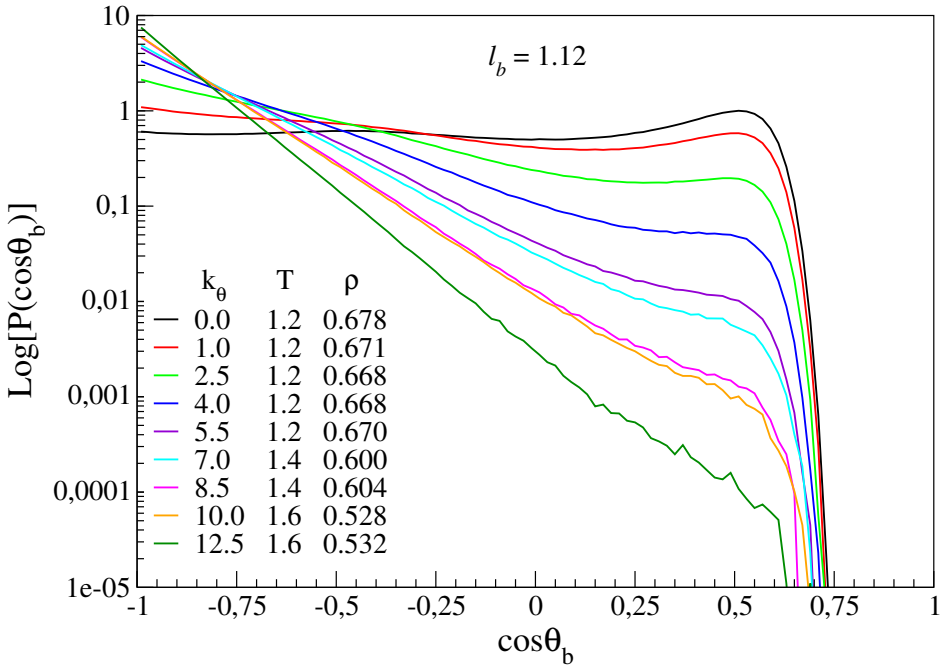

Figure 3.8: Semi-logarithmic plot of the distribution of bond angles. A Boltzmann-like behaviour is evident for stiffer systems (linear curves), as expected being the stiffness potential linear in $\cos\theta_b$. While for nearly fully flexible chains the distribution is flatter with peaks on the typical angles $\theta_b^1 \approx 59°$, $\theta_b^2 \approx 180°$, $\theta_b^3 \approx \pi - \theta_b^1$, stiff chains consist basically of aligned pairs of bonds.

The stretching behaviour of stiffer chains, demonstrated by increasing Kuhn lengths, reported later in fig. 3.21, is confirmed by analysis of the distribution of angles between adjacent bonds (i.e. angles formed by triplets of subsequent bonded monomers), which is shown in fig. 3.8. With increasing k_θ the folded configurations described in section 3.3.1 progressively disappear and $P(\cos\theta_b)$ becomes exponential, with maximum in $\theta_b = 180°$, which means

that the two subsequent bonds align. This exponential behaviour of the stiffer chains corresponds to a Boltzmann probability distribution, as the stiffness potential is linear in $\cos\theta_b$ (see 2.23).

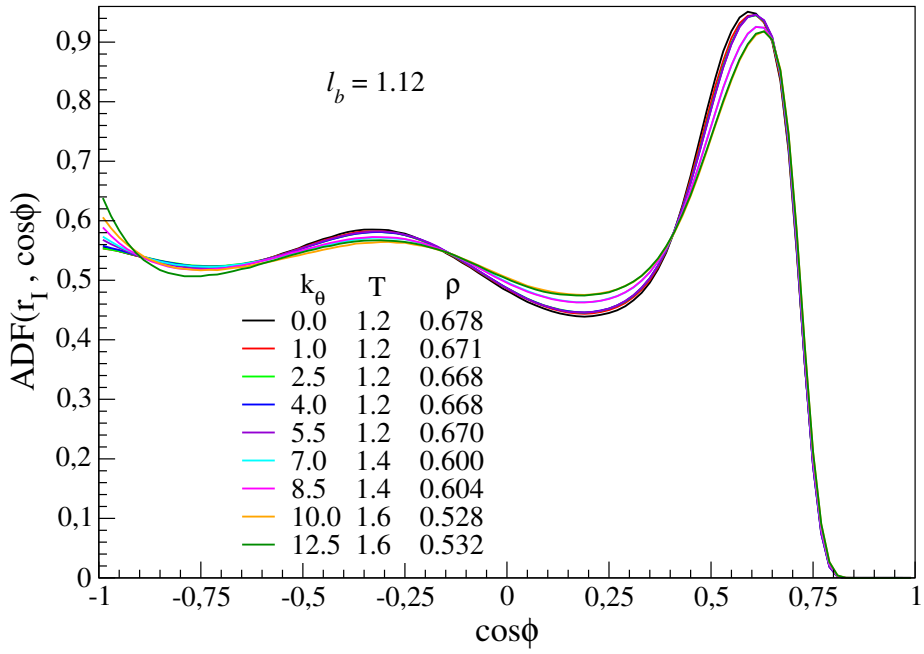

Figure 3.9: Angular distribution function of first neighbour triplets. Systems of stiffer chains display flatter distributions for little and intermediate angles, in favour of a more pronounced peak at $\phi = 180°$. The favoured values of ϕ are $50 \div 54°$ and $\approx 110°$.

In general the distribution of angles enclosed by triplets of first neighbours, as reported in fig. 3.9, shows that the favoured angles are little influenced by chain stiffness: the first peak is found in the range $50 \div 54°$ while the second is around $110°$ for all systems. The peak at $\phi = 180°$ is more pronounced for stiffer chains, resulting in a flattening of the distribution for intermediate angles.

Effects of stiffness eventually disappear in the angular distribution of second neighbours, as one can see in fig. 3.10. For all the values of stiffness, the favoured angles are approximately $30°$ (strongest peak) and $60°$ (weakest peak). The different distribution widths are ascribed to different equilibration temperatures: typically to higher temperatures correspond broader distributions, due to the disordering effect of thermal motion.

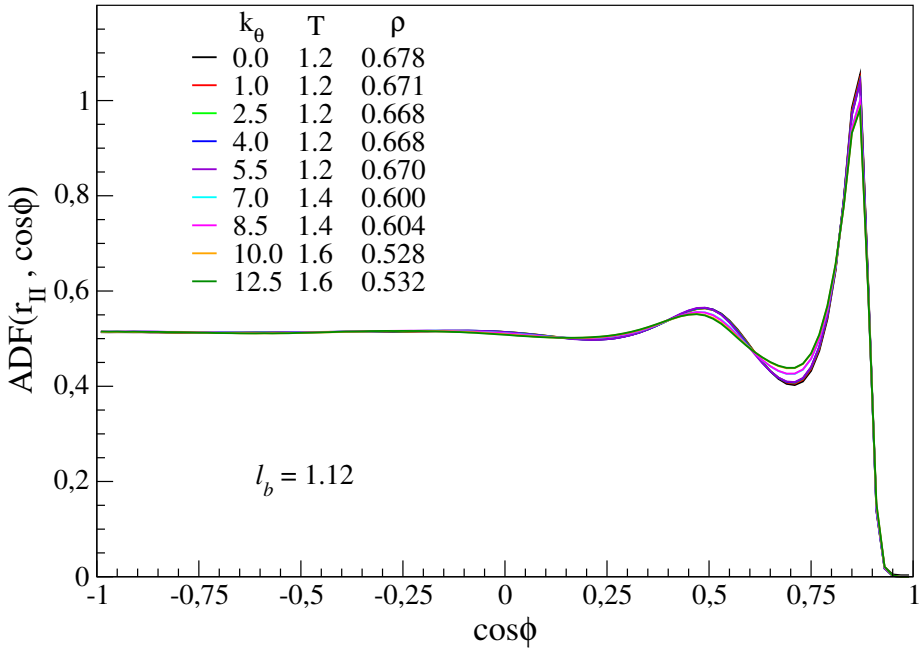

Figure 3.10: Angular distribution function of second neighbours. No effect of chain stiffness is observed, and the favoured angles continue to be $\phi \approx 30°$ and $\phi \approx 60°$ as in the fully flexible case. Distributions are broader for higher equilibration temperatures, as can be expected from the disordering due to thermal motion.

3.4 The solid phase

In order to obtain solids from the liquids studied in the last section, all the systems previously described are progressively cooled down from the corresponding initial temperatures, at the constant quench rate $|\dot{T}| = 2 \times 10^{-6}$, until they reach a temperature very close to zero (elastic properties are studied at exactly $T = 0$), namely $T = 10^{-3}$. The reason of this choice of $|\dot{T}|$ is that it is slow enough to provide a significant variety of morphologies formed upon solidification, at an acceptable computational cost.

During the cooling process, described in section 2.7, the response in static properties is monitored through the analysis of the temperature dependence of density $\rho(T)$ and of the global orientational order parameter $Q_6^{global}(T)$ described in section 3.2.4.

Once the final temperature is reached, the other order parameters and all the distribution functions already studied in the liquid phase (see section 3.3 for comparison) are measured.

3.4.1 Bond length

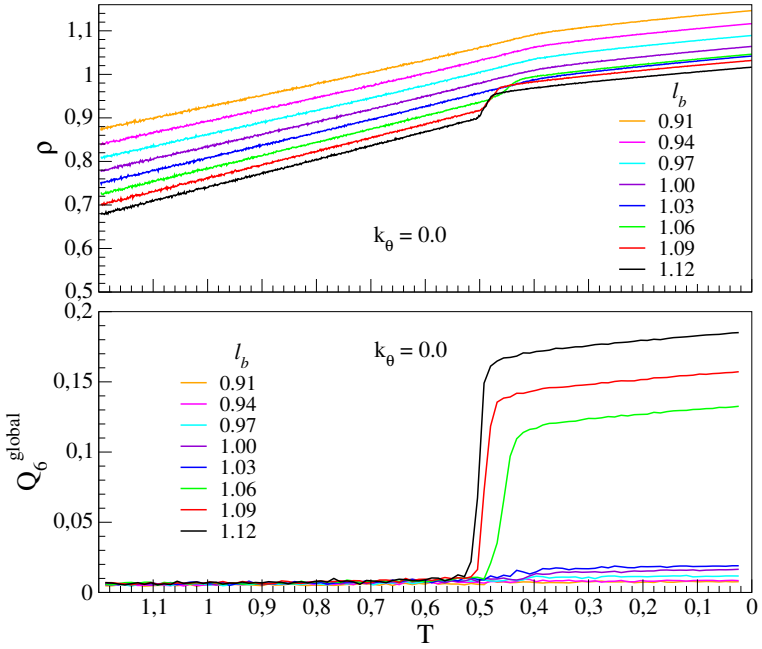

Figure 3.11: Density (upper panel) and global order parameter (lower panel) of systems with different bond lengths l_b, as a function of temperature T. During the cooling process, T is brought to zero from an initial value of 1.2, with quench rate $|\dot{T}| = 2 \times 10^{-6}$. At high temperatures all systems densify with almost the same thermal expansion coefficient, and no change in global order is observed. The response to cooling splits the curves into two families: systems with $l_b \leq 1.03$ vitrify at a certain value of $T = T_g$, around which density begins to increase more slowly with decreasing temperature, while global order keeps unchanged. Systems with $l_b \geq 1.06$ exhibit a sharp jump in density at $T = T_c$ similar to that of a first order transition to the solid phase, and a jump is simultaneously observed in the global order parameter.

As in the liquid phase, the effect of bond length is studied by setting k_θ to zero and varying systematically l_b in the bond potential eq. (2.20), from 0.91 to $r_0 = 1.12$. The plots reported display curves obtained from average on 16 simulation runs for each value of l_b.

In fig. 3.11 density and the global order parameter $Q_6^{global}(T)$ monitored during the cooling process are reported. At high temperatures, all systems show a linear increase of density as T decreases, which means that they densify at constant thermal expansion coefficient. At lower temperatures two different solidification behaviours are observed. For systems with equilibrium

bond length $l_b \leq 1.03$ a change of slope (thermal expansion coefficient) occurs at temperature $T = T_g$, as the liquids undergo glass transition.

For systems with $l_b \geq 1.06$, the different increases in density at high and low temperatures are separated by a sharp jump in density, occurring at temperature $T = T_c$. This jump is analogous to that of a first order phase transition, and it is therefore identified as the onset of crystallization. In the upper panel of fig. 3.11 the density jump appears less sharp because of the averaging process, but it is clearly visible in the behaviour of single runs, shown for a few cases in fig. 3.12.

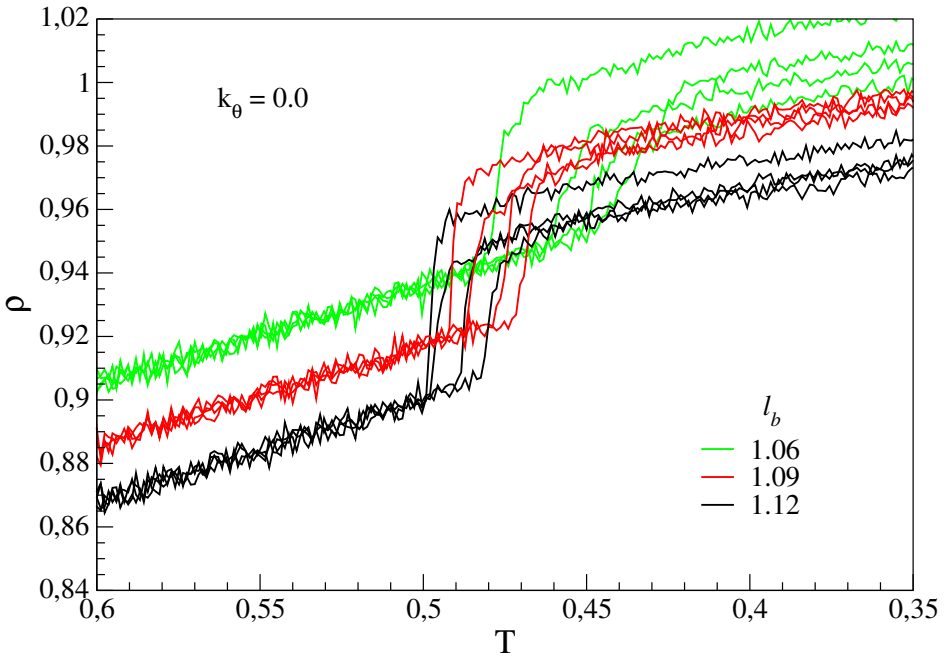

Figure 3.12: Density around T_c in some simulation runs of systems forming polymer crystals. Notice the sharp first order transition-like jumps before and after which density increase linearly with temperature.

In order to better characterize the two different solidification processes, the global orientational order parameter $Q_6^{global}(T)$ is measured as function of temperature (lower panel of fig. 3.11). Notice that glass forming samples, for which the change in density upon cooling is smooth and concave-down, show no significant change in the order parameter. This is given account for by the fact that systems going through glass transition tend to preserve their disordered liquid phase structure.

On the other hand, systems with $l_b \geq 1.06$ show, in most simulation runs, a sharp increase of $Q_6^{global}(T)$ at the very temperatures at which the jump in

density occurs, confirming the onset of a transition to a more ordered phase with respect to the liquid phase, i.e. nucleation. The nucleation process appears to be interrupted by glass transition, as the final values of $Q_6^{global}(T)$ are lower than the typical values obtained for ideal crystalline structures (table 3.1), and also span a rather wide range (in fig. 3.11 only the averages on the runs are reported). For this reason we expect the formed solids to be *partial* or *semi-crystals*, and they will be referred to in the following as polymer crystals or simply crystals. The differences in structure between

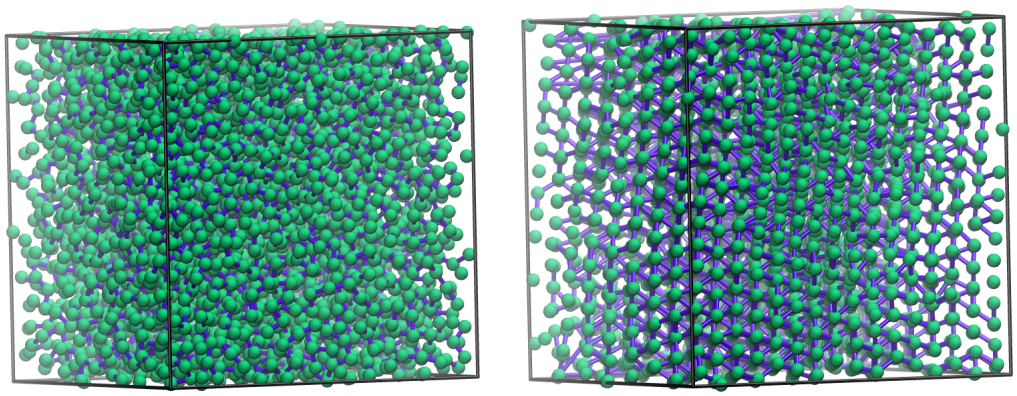

(a) glass **(b)** semi-crystal

Figure 3.13: Visualizations of the simulation box for a completely amorphous glass (a) and a partially crystallized glass (b). Monomers are represented in green, bonds in blue. In the partial crystal, notice the ordered alignment of monomers in some regions of space.

completely amorphous glasses and polymer crystals are easily understood through visualisations, reported in fig. 3.13, where the green spheres represent monomers and the blue links the bonds. While the bonds are randomly oriented in both the structures, in partially crystallized samples there are some regions of space where monomers tend to assume an ordered spatial disposition, which does not occur in pure glasses.

Solidification temperatures were extrapolated for every simulation run in two different ways for glass transition and polymeric crystallization. In the former case, T_g was determined as the temperature of intersection of linear fits to the high-T and low-T regimes of $\rho(T)$, whereas in the latter T_c was identified as the temperature of occurrence of the sharp density jumps.

The resulting solidification temperatures T_s are plotted in fig. 3.14. Both glass transition and crystallization temperatures increase monotonically with bond length, with the effective slope of T_c being more than twice that of T_g. When the gap between the two scale lengths $|l_b - r_0|$ of the system is small,

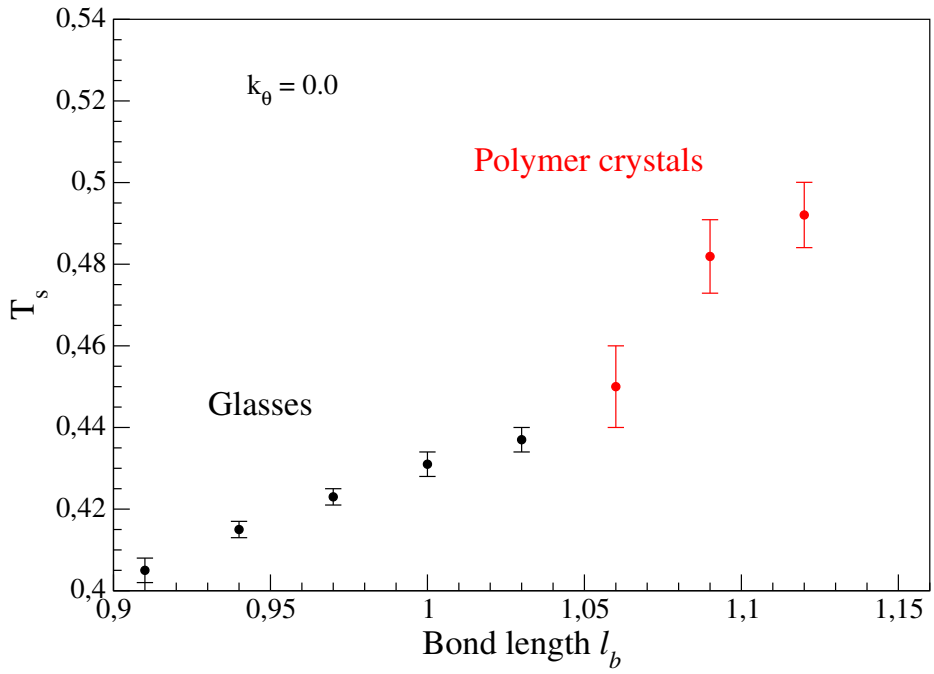

Figure 3.14: The dependence of solidification temperatures on bond length l_b is shown, at fixed quench rate $|\dot{T}| = 2 \times 10^{-6}$. Black dots correspond to glass transition temperatures, whereas red dots indicate polymeric crystallization temperatures.

crystallization takes place at higher temperatures, because the decrease of geometrical frustration results in deeper crystal-like minima of the potential energy landscape (see fig. 1.8), so that higher thermal energies are already enough for the system to be confined in one of these minima. With increasing gap, frustration increases and the available crystal-like minima are shallower, allowing only less thermally energetic monomers to stabilize in. Under some threshold value of bond length, included in $1.03 \leq l_b \leq 1.06$, frustration is so strong and thus crystal-like minima are so shallow, that the system under cooling continues sampling the energy landscape (PEL) without being confined, and thus entering the supercooled regime. When thermal energy is so low that the kinetics are arrested, the system finds itself in a certain point around a local minimum of the PEL, and the glassy state is reached. The temperature T_g at which this occurs increases monotonically with bond length under the crystallization threshold.

The different structures formed upon cooling are described in a more detailed way through the analysis of the monomer distribution functions at $T = 0$, namely $g(r)$, $P(\cos\theta_b)$, $ADF\,(r_I, \cos\phi)$ and $ADF\,(r_{II}, \cos\phi)$, and of

all the local and global order parameters. First, in fig. 3.15 the radial pair

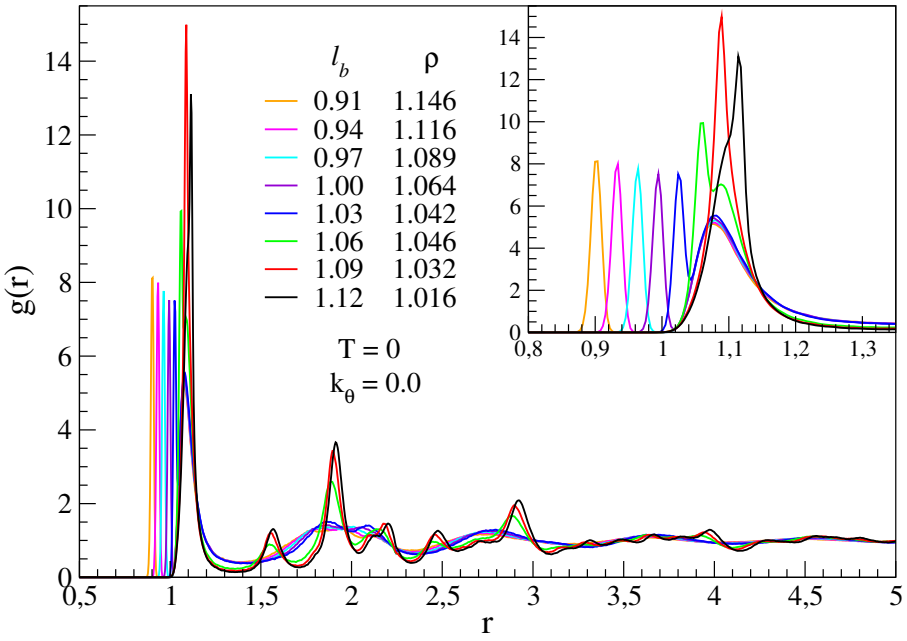

Figure 3.15: Radial pair distribution function $g(r)$ of solids with different bond lengths l_b. Two families of curves are clearly distinguishable: glass formers have flatter distributions which smoothen rapidly, whereas in polymer crystals strong peaks are present and modulation goes on for large values of r, exhibiting long range order. In the inset the first neighbour peak is shown for both the families. The densities ρ in the legend are those reached at the end of the cooling process.

distribution function $g(r)$ is shown. In this plot two families of curves are clearly identified. The ones which are flatter in the long range correspond to glasses ($0.91 \leq l_b \leq 1.03$). A strong increase can be noticed in the short range order of these structures, with respect to the liquids (see fig. 3.3). Consider for instance the peaks corresponding to the first coordination shells $r_I = [0.8,\ 1.4]$, highlighted in the inset. All the distributions are narrower with respect to their liquid equivalent. Those corresponding to glasses, except the $l_b = 1.03$ one, all go to zero in the range between l_b and r_0, while they kept non-null in the liquids. In the $l_b = 1.03$ case, the short range ordering effect is that of resolving the two l_b and r_0 peaks, which appeared joint in the $g(r)$ of the liquids.

Another signal of local ordering in glasses is encountered in the second coordination shell peak ($r_{II} = [1.4,\ 2.3]$), which is now resolved into the three different smaller peaks typical of polymer systems. An increase in the long

range order, in comparison to the liquid phase, is also present even if much weaker, as some slight peaks begin to pop up for values of $r \geq 2$, after which $g(r)$ at finite T no more shows modulation. Long range order is affected by l_b in the sense that from the second coordination shell on, $g(r)$ exhibits broader peaks the smaller is l_b. The disordering effect of the competition between bond length and LJ equilibrium separation thus continues to exist even among glasses.

The structure of polymeric crystals ($l_b \geq 1.06$) is quite different. Peaks in solid phase $g(r)$ are much more frequent and narrow, consistently with values reached by the Q_6^{global} order parameter, and they survive for large distances ($r \approx 4$). Except for the peak relative to the first coordination shell, which in the $l_b = 1.09$ case is very narrow because the l_b and r_0 contributions are not resolved, all the peaks are as narrower as closer l_b is to r_0.

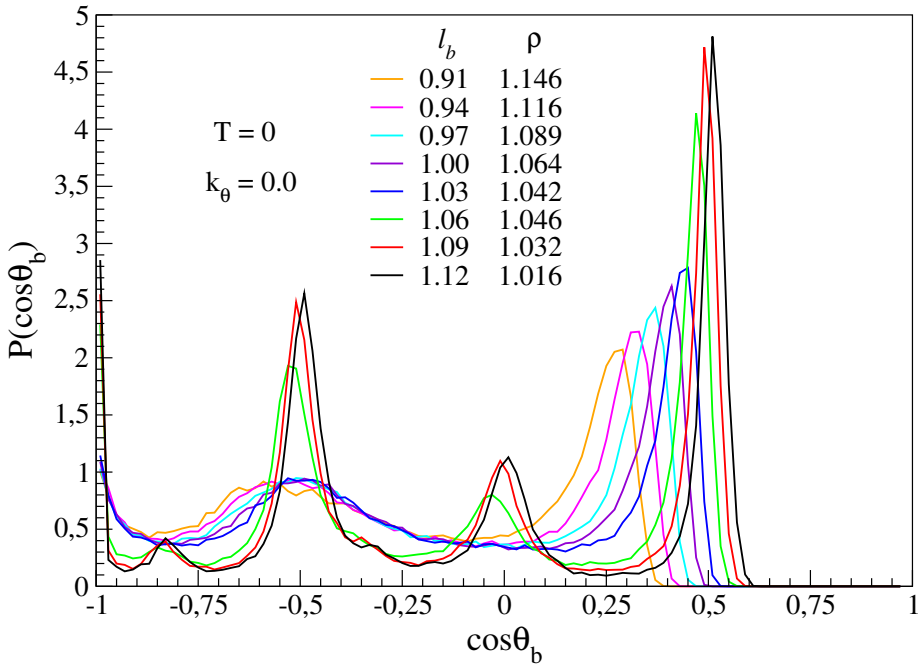

Figure 3.16: Distribution of angles formed by triplets of subsequent bonded monomers. The family of sharper curves ($l_b \geq 1.06$) correspond to polymeric crystals. The favoured angles of 90° and 145° appear in addiction to those already present in the liquids. These angles are associated with the more ordered monomer configuration settling upon crystallization. Flatter curves ($l_b \leq 1.03$) belong to glasses. Favoured angles are the same as in the liquid phase, but peaks are narrower due to removal of thermal vibrations.

A narrowing of the peaks is observed also in the angular distribution

functions. The distribution $P(\cos\theta_b)$ of angles between pairs of subsequent bonds is shown in fig. 3.16. As far as glasses are concerned, it can be seen that the favoured angles are the same as in the finite T regime. On the other hand, in the case of polymer crystals two more peaks appear at $\theta_b \approx 90°$ and at $\theta_b \approx 145°$. It can be guessed that these two angles are functional to the establishment of a more ordered structure. This is confirmed by analysis of the angular distributions of first neighbours .

$ADF\,(r_I, \cos\phi)$, shown in fig. 3.17, for polymeric crystals is almost equivalent to $P(\cos\theta_b)$. This means that the necessity of monomers to rearrange in an ordered structure is dominant so that triplets tend to form specific angles irrespective of their bonded or non bonded nature. This behaviour is not encountered in glasses, where the angular distribution of bonded monomers is quite different from that of the other first neighbours: while there is no change with respect to the liquids for large angles, a remarkable effect takes

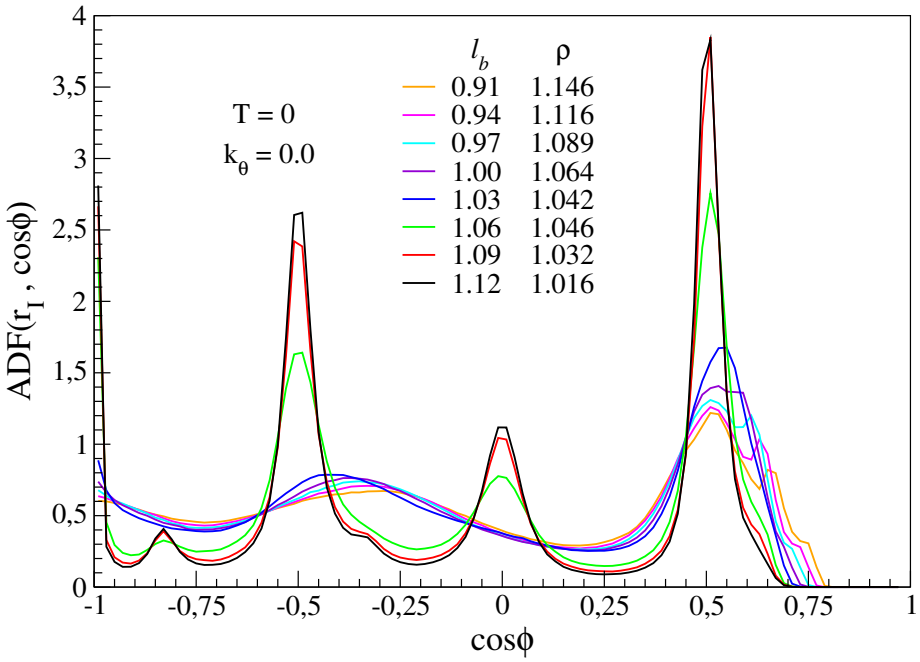

Figure 3.17: Angular distribution function of first neighbour triplets (r_I = [0.8, 1.4] as extrapolated from $g(r)$). For crystals ($l_b \geq 1.06$) the favoured angles are the same as in the bond angle distribution, since both bonded and non bonded near monomers occupy the reciprocal positions which are required by crystalline structure. Glasses ($l_b \leq 1.03$) exhibit almost the same distribution as in the liquids, except that the peak for large angles is shifted ($\phi = 36 \div 72°$) and splits in three with resolution proportional to $l_b - r_0$ difference.

place at small angles. A peak in the range $\phi = 36 \div 72°$ is found for all $l_b \leq 1.03$, which is resolved into three different contributions for $l_b = 0.91$. This resolution decreases with increasing l_b until it is no more visible for $l_b = 1.03$.

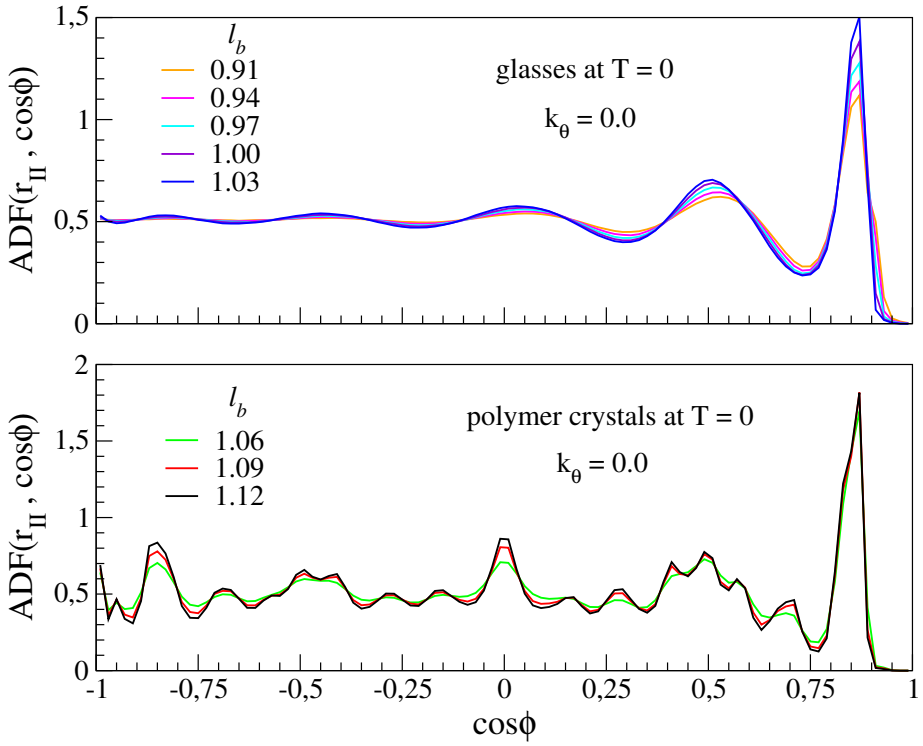

Figure 3.18: Angular distribution of the second coordination shell for glasses (upper panel) and polymeric crystals (lower panel), at $r_{II} = [1.4,\ 2.3]$. Glasses exhibit a (weak) increase in the long-range order, as $ADF\,(r_{II}, \cos\phi)$ shows modulation beyond $\phi = 90°$. In polymeric crystals this modulation is remarkably strong, since long range order is still significant, despite being weaker than in ideal crystals.

The angular distribution of second neighbours $ADF\,(r_{II}, \cos\phi)$, where $r_{II} = [1.4,\ 2.3]$, is shown in fig. 3.18. In glasses (upper panel) a slight increase in long-range order appears with respect to the liquids: modulation of $ADF\,(r_{II}, \cos\phi)$ holds on for the whole range of angles ϕ, with peaks of decreasing width for increasing $|l_b - r_0|$ gap. The increase in long-range order is much stronger in crystals (lower panel), where $ADF\,(r_{II}, \cos\phi)$ is strongly modulated.

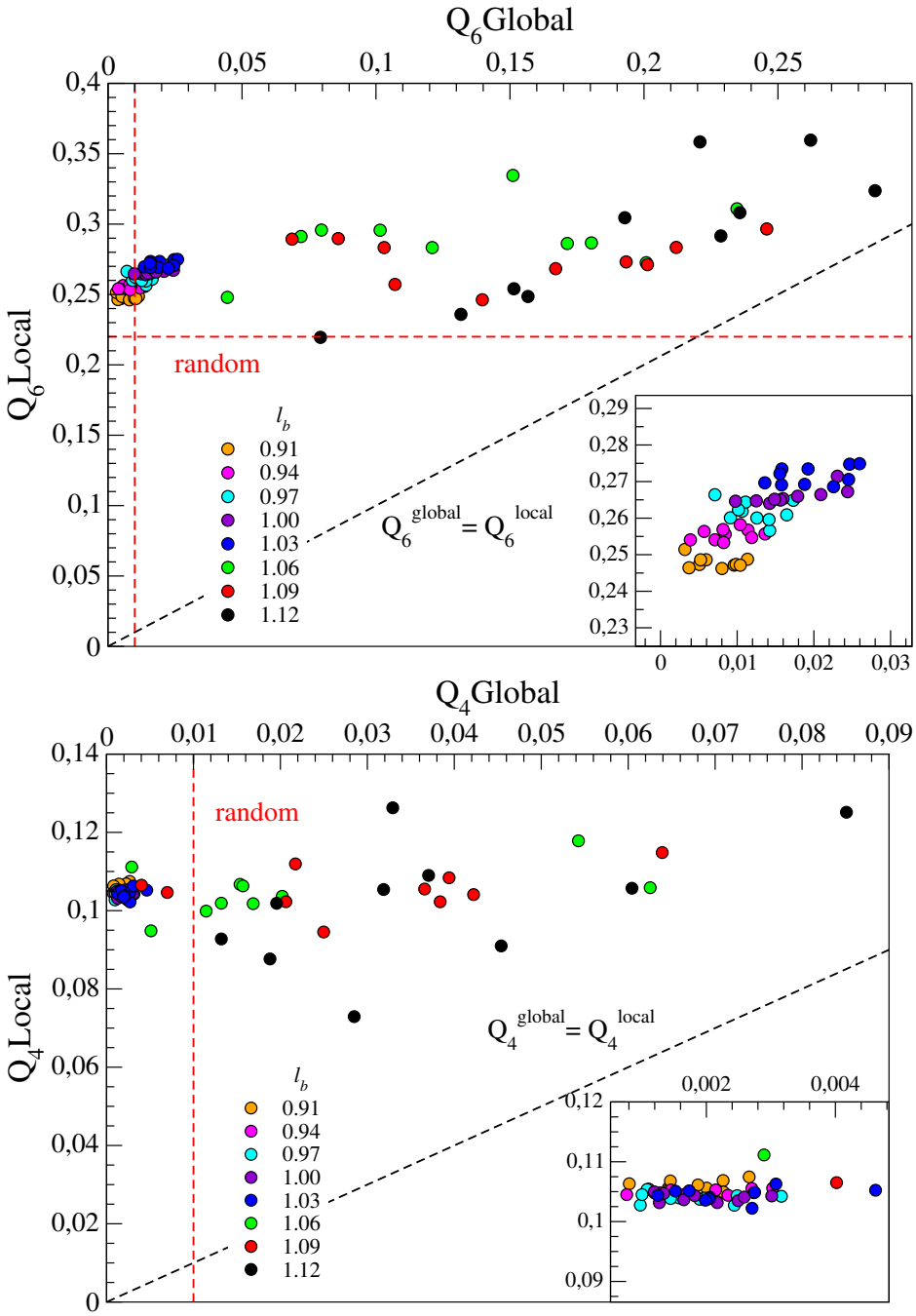

Figure 3.19: Correlations between the local and global expressions of the orientational order parameters Q_4 and Q_6, for systems of different bond length l_b. The red dashed lines correspond to the random configuration values $Q^{global}_{6,random} = Q^{global}_{4,random} \simeq 0.01$ and $Q^{local}_{6,random} = Q^{local}_{4,random} \simeq 0.22$. The black dashed line indicates the ideal structure $\frac{Q_l^{global}}{Q_l^{local}} = 1$ limit. In the insets, dots corresponding to glassy samples are reported to show the insensitivity of Q_4^{local} to bond length, in contrast with the increase of Q_6^{local} with l_b, and the correlation between Q_6^{global} and Q_6^{local}.

Additional information about local and global order of the structures formed upon cooling is provided by the orientational order parameters and their correlations (fig. 3.19). Glasses exhibit values of both Q_6^{global} and Q_6^{local} near to those corresponding to random configuration, with a smooth increase as bond length l_b gets closer to r_0. The two order parameters appear thus to be correlated. In polymeric crystals the two parameters span wider ranges, with Q_6^{local} closer to that of random configuration than of any ideal structure. Correlation between the two parameters is found also in crystals, with a tendency to the ideal structure ratio $\frac{Q_6^{global}}{Q_6^{local}} = 1$ which increases with decreasing $|l_b - r_0|$. Since Q_6^{local} of crystals is spread over a not so wide range around the glass-like value, while their Q_6^{global} is usually much bigger, one can argue that for $l = 6$, the global order achieved in polymeric crystals just comes from the repetition, through all the sample of the same, however disordered, local structure. The Q_4 parameters are insensitive to bond length in glasses, with Q_4^{local} assuming a value distant form that of random configuration, which confirms the observation that some sort of local order is present. As far as crystals are concerned, the same general trend $\frac{Q_4^{global}}{Q_4^{local}} \to 1$ with decreasing scale length discrepancy is found. Notice that Q_4^{local} in crystals is far from the random configuration value.

3.4.2 Chain stiffness

In this section the effect of chain stiffness on the static properties of polymers in the solid phase. Bond length is fixed at $l_b = r_0 = 1.12$ while k_θ is varied systematically from 0.0 to 12.5. Upon solidification, different morphologies arise in polymers with diverse stiffness. Before the analysis of the significant static quantities, a first guess at what happens upon cooling comes from the monitoring of response in density $\rho(T)$ and global orientational order parameter $Q_6^{global}(T)$. The quench rate is the same for all systems, namely $|\dot{T}| = 2 \times 10^{-6}$, while initial values of density and temperature can vary as specified in section 3.3.2.

The density and the global order parameter are shown in fig. 3.20 as function of decreasing temperature. At high temperature all systems densify at a constant thermal expansion coefficient. As temperature is decreased, it can be seen that chain stiffness begins to play a significant role in the solidification process. The fully flexible system goes through crystallization in most of the simulation runs, with the sharp density jumps described in section 3.4.1. For $k_\theta = 1.0$ the competition between glass transition and crystallization is clearly visible: around T_c of the fully flexible polymer, the density shows a slight concave up change in slope; nonetheless this is almost

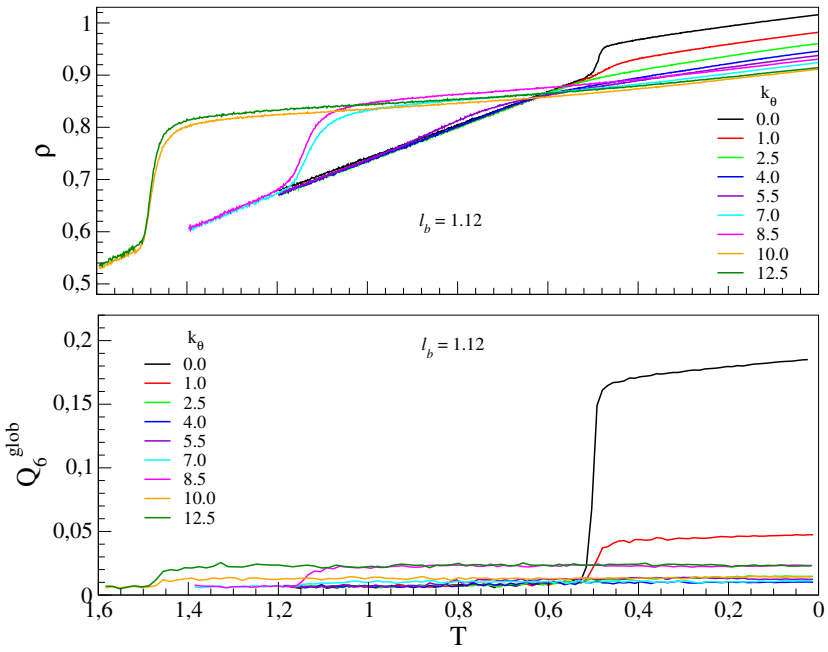

Figure 3.20: Response of samples with different chain stiffness to cooling. In the upper panel the increase of density with decreasing temperature is shown, and for each curve the corresponding behaviour of the order parameter $Q_6^{global}(T)$ is shown in the lower panel. Three different solidification behaviours are visible: stiff polymers ($k_\theta \geq 7.0$) undergo a nematic ordering transition at high temperatures, resulting in a sharp jump in density and a slight increase in global order; polymers with intermediate stiffness ($1.0 \leq k_\theta \leq 5.5$) undergo glass transition (change in density slope and no change in global order); fully flexible samples ($k_\theta = 0.0$) partially crystallize (sharp jump both in density and in the order parameter).

immediately hindered by the onset of glass transition, which turns the density curve concave down until it recovers the linear increase with decreasing temperature, now with the slope of a glass. This phenomenon gives rise to an intermediate structure described further below. For values of chain stiffness $2.5 \leq k_\theta \leq 5.5$, the ordering process is hindered before nucleation can start, and glass transition takes place, with a concave down change in the density slope. For stiffer systems sharp jumps in densities are found again. Since it can be said from the previous results, that chain stiffness prevents crystallization, and from the fact that these jumps occur at high temperatures, it can be guessed that for systems with $k_\theta \geq 7.0$ the observed transition is of another different kind.

This can be understood also from the monitoring of the global orien-

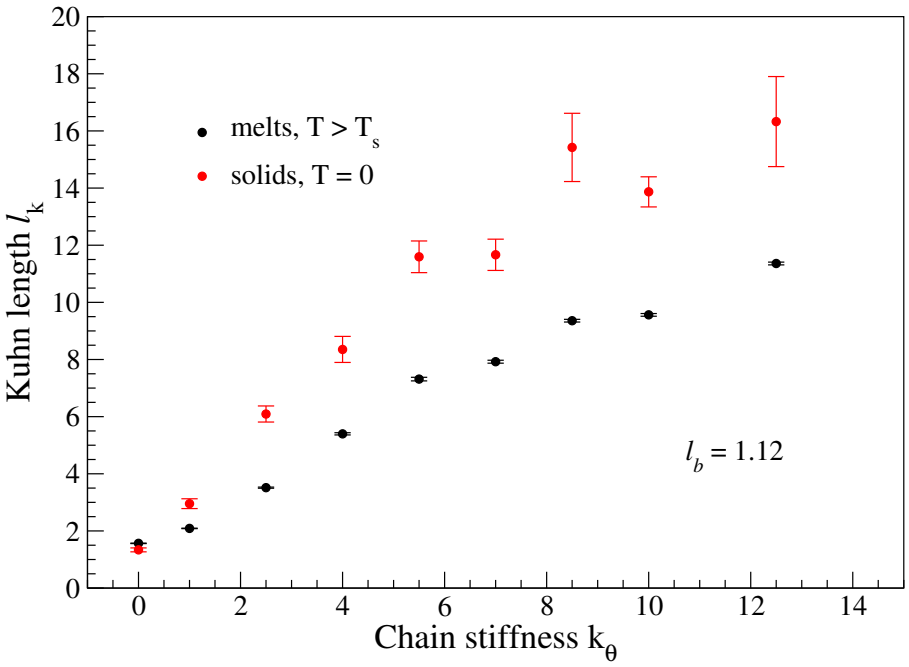

Figure 3.21: Correlations between Kuhn length and chain stiffness are shown for temperatures above solidification T_s (black dots), and for the zero temperature regime (red dots). Kuhn length increases with k_θ, as monomers belonging to stiffer chains tend to align.

tational order parameter $Q_6^{global}(T)$ during cooling. Proper polymeric crystallization occurs only for the fully flexible system, and rarely also for the $k_\theta = 1.0$ and $k_\theta = 8.5$ samples, when $Q_6^{global}(T)$ exhibits a sharp jump at a certain temperature, reaching a value greater than 0.1. In systems of stiffness $k_\theta = 1.0$ and $k_\theta = 12.5$ jumps also occur, but with much smaller final values. In all the other cases, including glasses with $2.5 \leq k_\theta \leq 5.5$ and systems with $7.0 \leq k_\theta \leq 10.0$, this order parameter shows no significant changes from its liquid phase value. That observed in high stiffness samples is identified as a transition to a nematic glass state, i.e. a state in which the chains are stretched and tend to align along the same direction.

Proof for this interpretation is provided by analysis of the Kuhn lengths l_k (fig. 3.21). The different structures of polymer crystals, normal glasses and nematic glasses are reproduced in the visualizations reported in fig. 3.22. The spatial disposition of monomers and chains are represented respectively in the first and in the second row of the figure. The structure of a partial crystal can be recognized by the alignment of the monomers (a) in a certain region of the simulation box, while disorder is present at the chain scale (d),

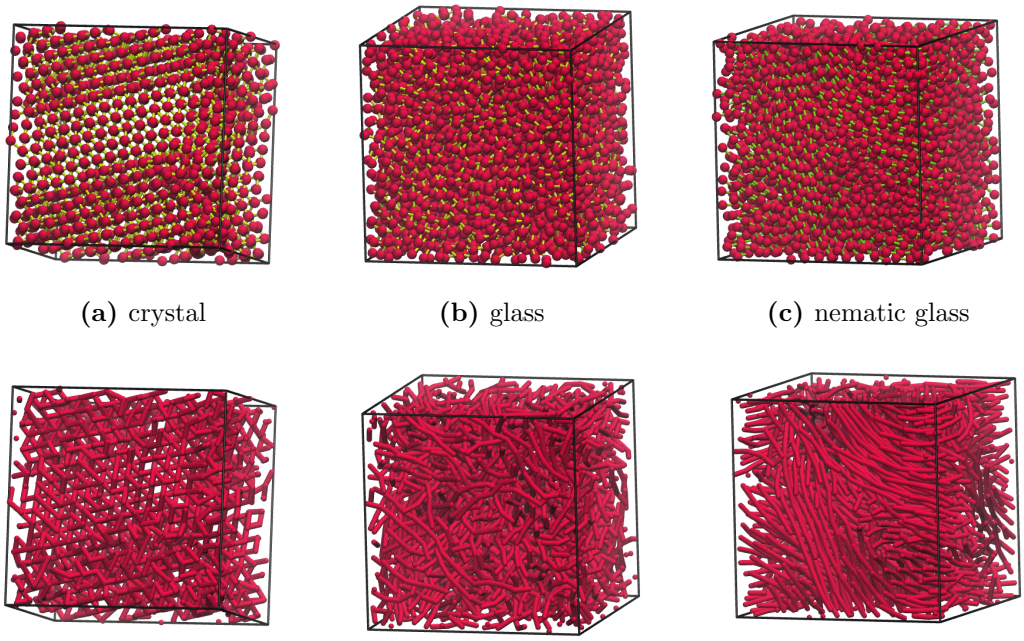

(a) crystal **(b)** glass **(c)** nematic glass

(d) crystal **(e)** glass **(f)** nematic glass

Figure 3.22: Visualizations of the simulation box for a polymer crystal (a, d), a normal glass (b, e) and a nematic glass (c, f). In the first row, monomers are shown in red and bonds in yellow, while in the second row the disposition of chains is illustrated.

except for the recurrence of the $\approx 60^\circ$ bond angle. In the typical amorphous glass (b-e), disorder is present both at the monomer and at the chain scale. The situation is again different for nematic glasses, in which the chains are highly stretched (f) and tend to align, while the disposition of monomers (c) is as disordered as in the amorphous glasses.

Solidification temperatures are reported in fig. 3.23 as function of chain stiffness. Restricting attention to glasses, the transition temperature T_g is observed to increase linearly with k_θ. Notice that differently from the case of varying bond length, in which a geometrical factor in the potential is changed with frustration effects, here it is the interaction constant (k_θ) to change, so that the single monomer potential well deepens with increasing chain stiffness. As a result, even if the local disposition of monomers is more disordered for stiffer chains (as discussed in the following), so that total potential energy minima are shallower, nonetheless single monomers are increasingly more confined to their positions. This means that the mobility of single monomers is reduced so that glass transition takes place more easily,

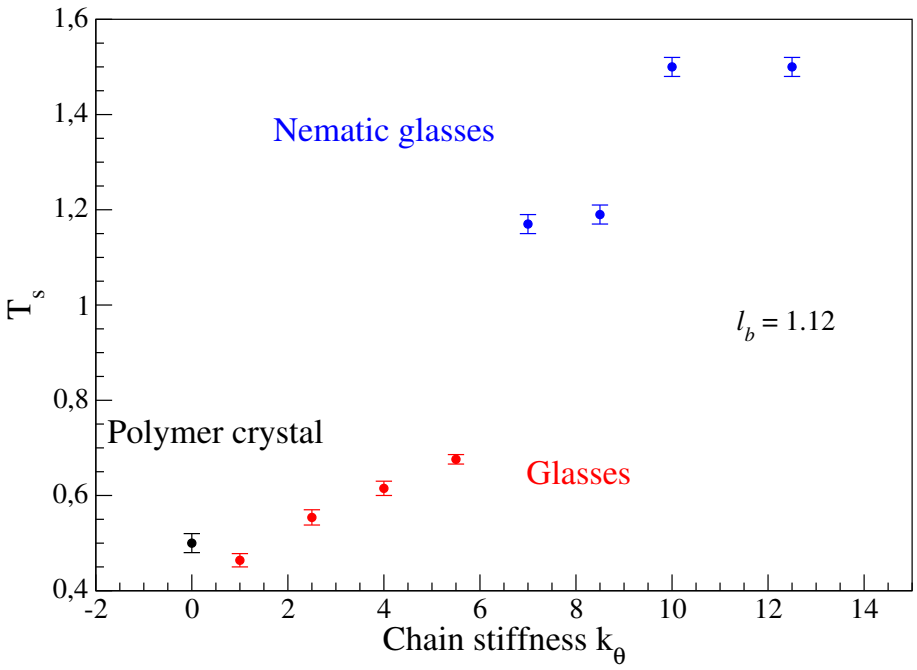

Figure 3.23: Solidification temperatures as function of chain stiffness. The black dot corresponds to the polymer crystallization temperature of the fully flexible sample, whereas red and blue dots represent pure and nematic glass transition respectively.

i.e. at higher temperatures.

The family of nematic glass transition temperatures is sharply separated from the others, but it has to be reminded that in systems with $7.0 \leq k_\theta \leq 8.5$ and $k_\theta \geq 10.0$, cooling starts from different initial temperatures, specified at the beginning of section 3.3.2. However it is evident that for nematic glasses, the transition temperature has a more complex dependence upon chain stiffness, even though they still are in an increasing relation, within error. These results are in agreement with the observations reported in [40].

The static properties are now considered.

First, $g(r)$ is reported in fig. 3.24. For all systems of non-zero stiffness, the radial distribution function is that of a glass (upper panel), with no remarkable differences. A longer range of more pronounced modulation with respect to the liquids, and the splitting of the second coordination shell peak into three contributions are again found, as in the study of the effects of bond length.

The ranges of the first and second coordination shells extrapolated from $g(r)$ are respectively $r_I = [0.8,\ 1.4]$ and $r_{II} = [1.4,\ 2.3]$. In these ranges,

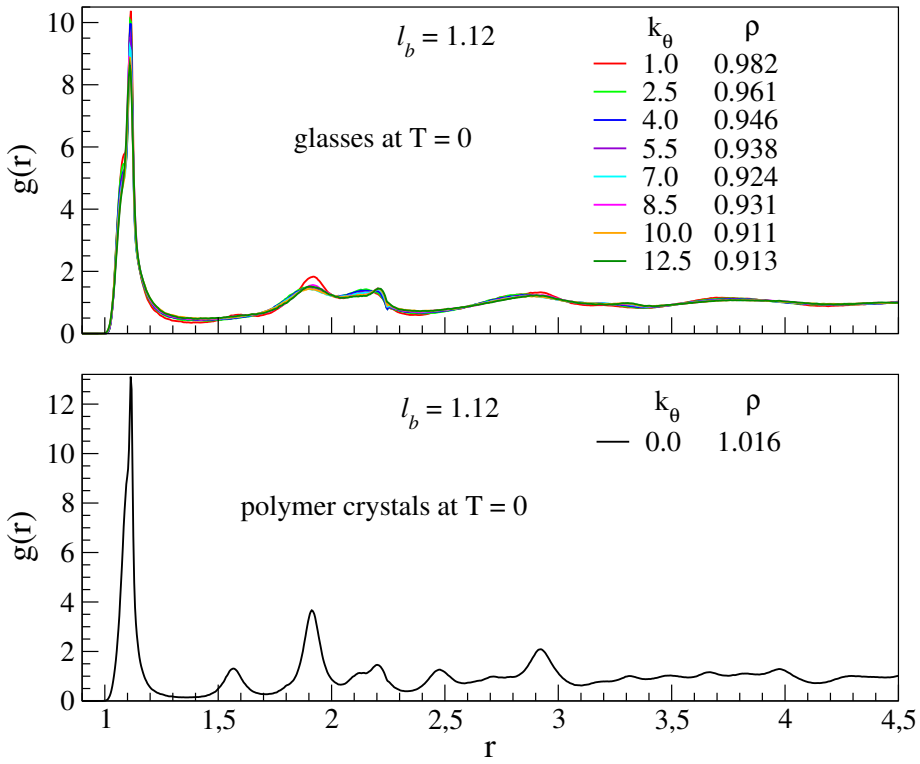

Figure 3.24: Radial pair distribution function of glasses (upper panel), and of the fully flexible polymeric crystal (lower panel). A similar configuration is found for all the non-crystalline systems, suggesting that glass transition eventually sets in also for nematic samples ($k_\theta \geq 7.0$). Flatter distribution are observed for systems with increasing chain stiffness, due to the disordering effect of chain stiffness.

analysis of the angular distributions of first and second neighbours is carried out.

As shown in fig. 3.25, the distribution of bond angles is modulated for the crystallized fully flexible system. This modulation is weak but still present in the $k_\theta = 1.0$ system, with much slighter peaks occurring at the same values of θ_b. This suggests that in this sample, monomers were rearranging in the ordered polymer crystal structure during cooling, when the dynamics became too slow, and glass transition took place. This effect is compatible with the two subsequent changes of slope observed in the density response $\rho(T)$ around solidification temperature (see fig. 3.20).

With increasing k_θ, $P(\cos\theta_b)$ becomes increasingly Boltzmann-like, i.e. exponential in $\cos\theta_b$, and for $k_\theta = 2.5$ the probability density $P(\cos\theta_b)$ is already under 0.1 for angles smaller than around 100°.

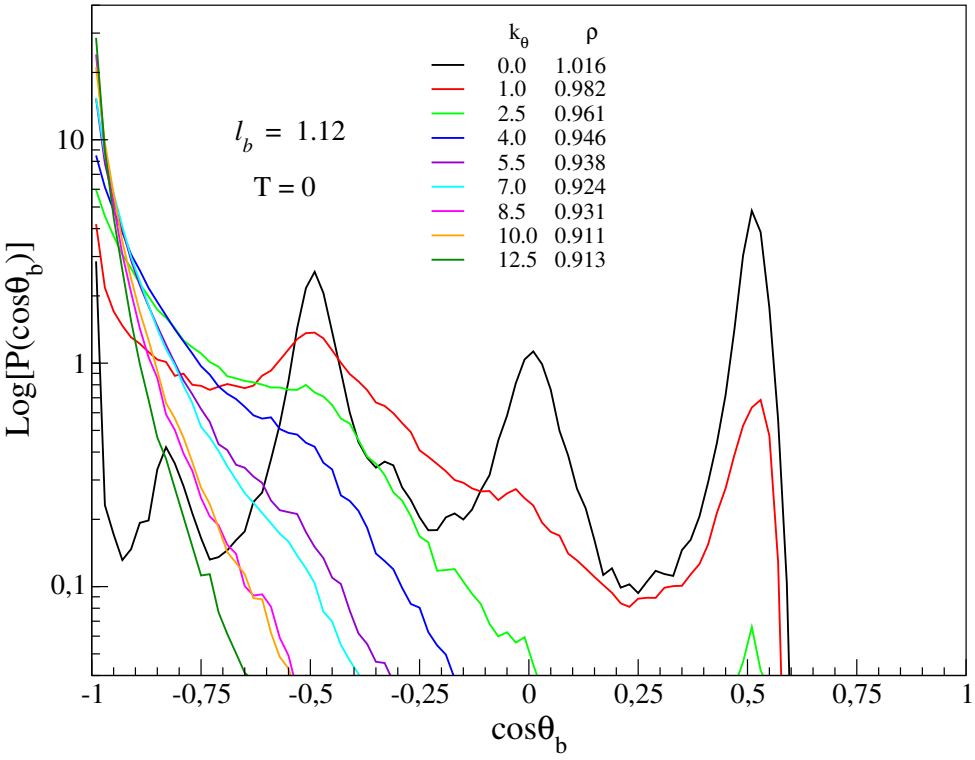

Figure 3.25: The distribution of bond angles θ_b is modulated for the crystallized samples, as an effect of established order. This modulation is found in a weaker fashion in the partially crystallized $k_\theta = 1.0$ sample. For increasing chain stiffness, $P(\cos\theta_b)$ becomes increasingly exponential (plot scale is semi-logarithmic). Acute angles are rarely formed ($P(\cos\theta_b) < 0.1$) by triplets of bonded monomers with chain stiffness $k_\theta \geq 2.5$.

Consider now the angular distribution of all the first neighbours $ADF\,(r_I, \cos\phi)$, shown in fig. 3.26. It can be seen that the sample with $k_\theta = 1.0$ again shows the effect of a nucleation interrupted by glass transition, as the corresponding distribution presents slight peaks at those values of ϕ which are the favoured angles in the fully flexible crystallized case (60°, 90°, 120° and 180°). The same trend in a weaker fashion is found for the $k_\theta = 8.5$ and $k_\theta = 12.5$ samples, whereas the one with $k_\theta = 10.0$ behaves in the same way as glasses. The latter show flatter distributions, index of greater disorder, and larger favoured angles with respect to the liquids, still close to 60° and 120°. These are the most frequent angles for a configuration in which the chains are aligned to each other.

The angular distribution of second neighbours do not change much upon

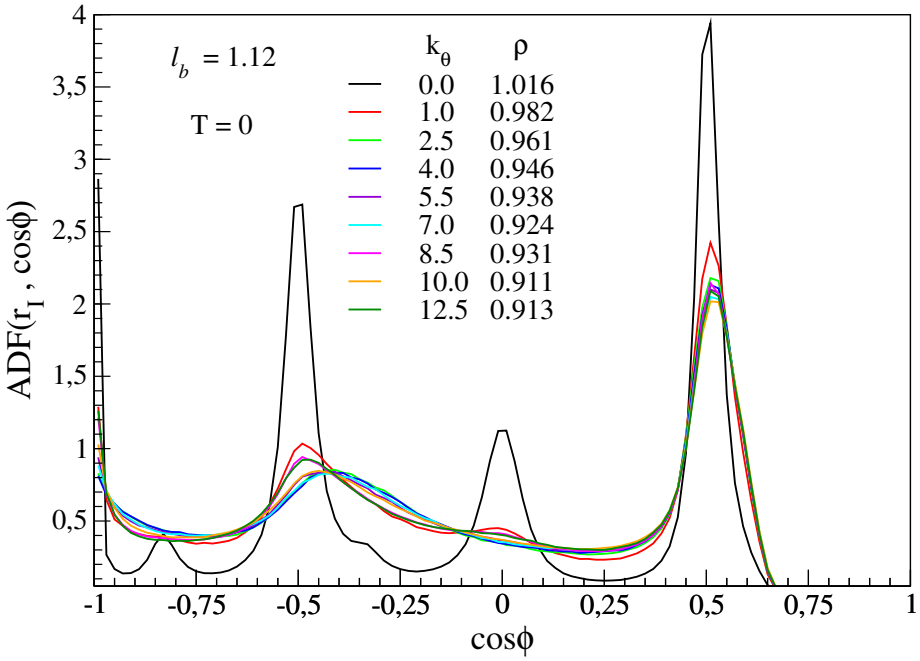

Figure 3.26: Angular distribution of monomers in the first coordination shell ($r_I = [0.8,\ 1.4]$, as extrapolated from $g(r)$). The $k_\theta = 1.0$, 8.5 and 12.5 samples exhibit again their intermediate structure, halfway between glassy and crystalline. The two different structures share favoured angles $\phi = 60°$, 120° and 180°. Additional angles formed in crystalline structures are $\phi = 90°$ and 145°, irrespective of chain stiffness. The flattening (disordering) effect of k_θ is confirmed.

vitrification, as can be seen from the upper panel of fig. 3.27. The favoured angles in glasses with chain stiffness are the same as in their liquid phase. The only remarkable change is found in modulation, which is slightly increased, since the degree of order increases weakly through glass transition. This order degree is smaller for stronger chain stiffness, as stiffer systems exhibits flatter distributions. This is an additional hint about the non globally ordered nature of the structures formed by the stiffest polymers upon solidification, even if the observed density jump is similar to that encountered in the crystallization of fully flexible polymers.

Additional information about local and global order is provided by the study of orientational order parameters (fig. 3.28). Glasses with chain stiffness exhibit different order parameters with respect to fully flexibles. At the local scale, the discriminating parameter is here Q_4^{local}. The latter smoothly increases with increasing chain stiffness, towards the random configuration value $Q_{4,random}^{local} \simeq 0.22$ while Q_6^{local} stabilizes on a value around 0.28. Thus,

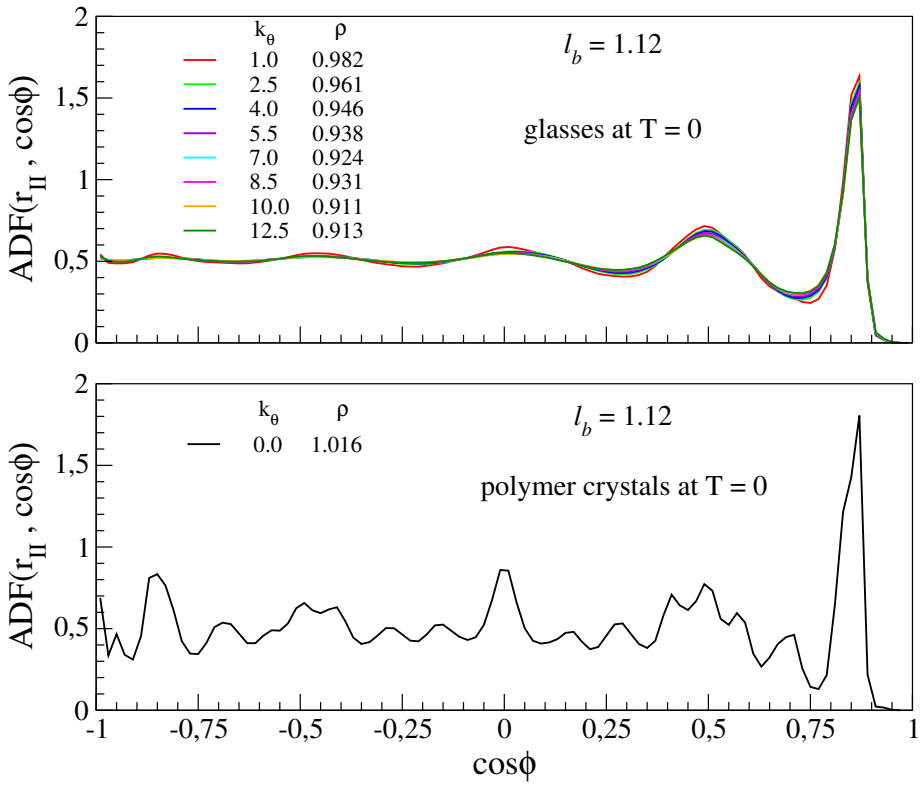

Figure 3.27: Angular distribution of second neighbours. Glasses (upper panel) exhibit no significant change from their liquid phase, except for a slightly increased range of modulation, due to gain of some global order which tend to vanish with chain stiffness.

the disordering effect of chain stiffness is confirmed. On the other hand, at the global scale both Q_4^{global} and Q_6^{global} are around the corresponding random configuration values, except for the single crystallized runs.

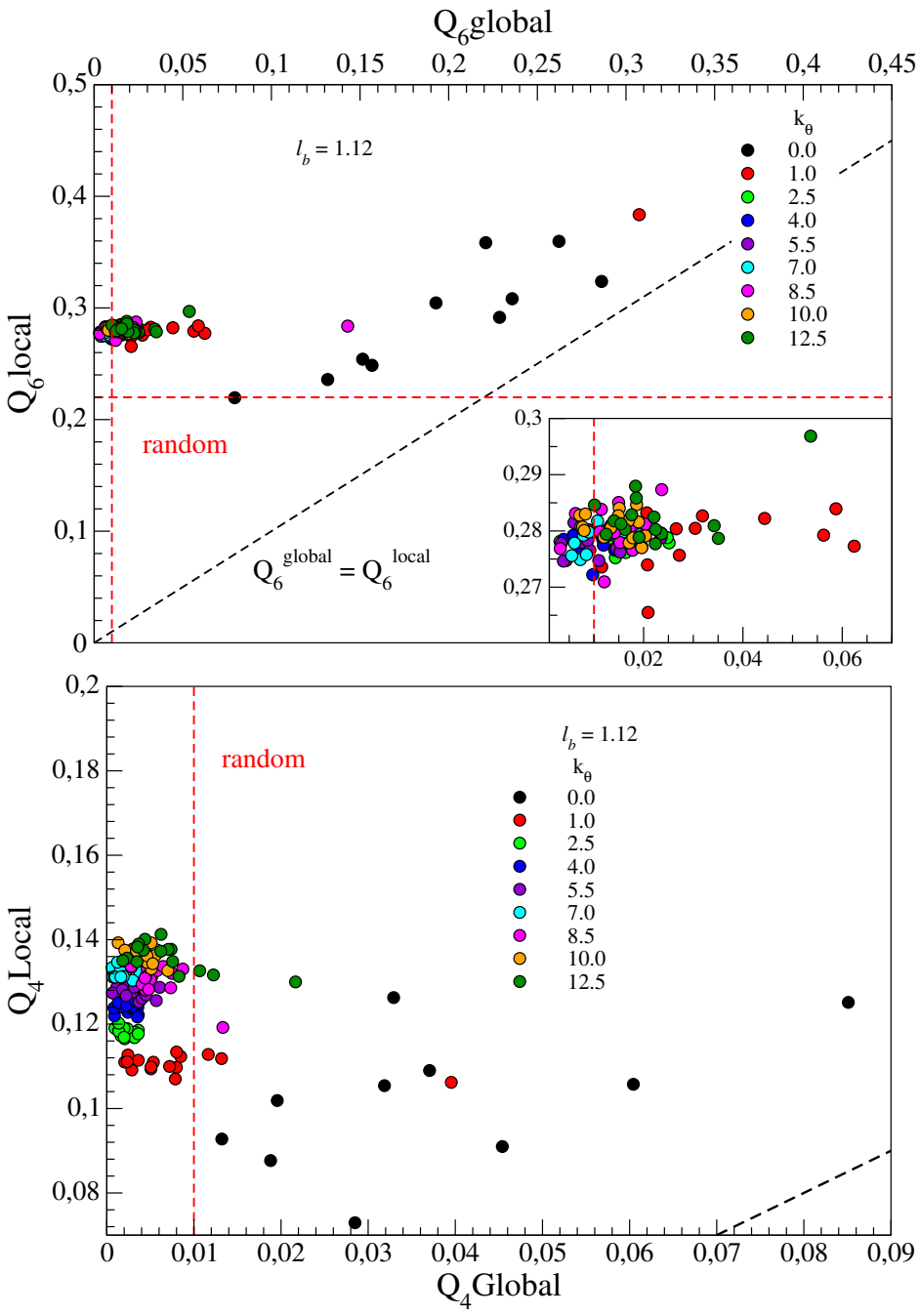

Figure 3.28: Correlations between the local and global expressions of the orientational order parameters Q_4 and Q_6, for systems with different chain stiffness k_θ. The red dashed lines correspond to the random configuration values $Q_{6,random}^{global} = Q_{4,random}^{global} \simeq 0.01$ and $Q_{6,random}^{local} = Q_{4,random}^{local} \simeq 0.22$. The black dashed line indicates the ideal structure $\frac{Q_l^{global}}{Q_l^{local}} = 1$ limit. In the inset of the upper panel, the focus is on glasses. The discriminant parameter in the local structure for stiff polymers is Q_4^{local}, increasing with chain stiffness.

3.5 Conclusions

In this section, we carried out a preliminary characterization of the polymer model of which we want to study the mechanical properties. For a better understanding of the model, we studied its static properties both in the phase of liquid and in the glassy state (with possible partial crystallization) at nearly zero temperature. The average spatial disposition of monomers has been measured in both cases, while density and global order have been monitored during cooling, allowing for investigation of solidification processes and extrapolation of glass transition and crystallization temperatures.

The latter have shown significant dependence from the connectivity-related parameters of the model, namely bond length l_b and chain stiffness k_θ. The glass transition temperature T_g increases monotonically with both l_b and k_θ. The crystallization temperature T_c also increases monotonically with l_b, while the temperature of transition to the nematic phase increases in a more complex way with k_θ.

The bulk morphologies of solid phase, obtained via linear cooling, are related to chain shape, which is controlled by systematic variation of the connectivity-related parameters. The microscopic details of the bond potential are found to have a strong effect on the microscopic local arrangement of monomers upon cooling. The gap $|l_b - r_0|$ between the two characteristic length scales of the model (r_0 is the bead diameter) causes geometrical frustration, which results in looser dispositions of neighbouring monomers, proved by the broadening of spatial distributions increasing smoothly with the size of the gap. The disordering effect also affects the propensity of a polymer to either crystallize or form a glass. Chain stiffness is observed to have an analogue disordering, distribution broadening effect. This happens because monomers are subjected to the additional constraint of keeping aligned to the successive along the chains.

Fixing the quench rate, for fully-flexible polymers an upper limit of bond length $l_{b,glass} = 1.03$ within which samples form glass, and a lower limit $l_{b,crys} = 1.06$ beyond which they form polymer crystals, are found. Similarly, threshold values of chain stiffness for semi-flexible polymers are found, separating semi-crystals ($k_\theta = 0.0$) from completely amorphous glass ($k_\theta \geq 1.0$), and the latter from nematic glasses ($7.0 \leq k_\theta$).

This first part of the work is also functional to the next, in which the mechanical response of the solids obtained here is studied.

Chapter 4

Elastic and yielding properties at zero temperature

4.1 Introduction

In crystalline materials, the phenomenon of plastic flow is well understood in terms of the motion of topological defects such as dislocations [43]. In amorphous solids like polymeric crystals and glasses, it is not yet clear what the carriers of plasticity are and whether the onset of plasticity can be related to the microscopic properties of the material. Despite existing attempts to relate mechanical properties of amorphous systems to the details of the interaction potential [44], a link is still missing that would allow for a better control of mechanical properties directly from the design of the microscopic structure.

In addiction, there are a number of works, based on the idea of shear-inducted changes in the potential energy landscape (mentioned in section 1.4), both experimental [45] and computational [46], which suggest that a relation can be established between the linear elastic response of a material subjected to small strains, and its plastic behaviour at larger strains. Finding a correlation between the linear behaviour at vanishing small perturbations (strains of order 10^{-4}), and the strongly non linear and irreversible response (yielding) to considerable external driving (order 10^{-1} deformation), is obviously an ambitious and challenging goal.

In the following part of this work the role of microscopic properties, such as bond length and chain stiffness, in the mechanical response of polymer glasses is studied, focusing both on their linear elastic response and on their plastic yielding. The existence of a correlation between these two deeply different behaviours is also investigated.

In order to study the mechanical response under shear deformation of the systems characterized in chapter 3, the athermal quasi-static (AQS) simulation protocol is used. This protocol, described in details in section 2.7, consists in the deformation at zero temperature of the solids, obtained after quenching in 3.4, and is performed iterating two steps, starting from an equilibrium configuration for each sample: (i) the system is deformed homogeneously by a very small increment; (ii) energy is minimized. For each choice of the shear direction xy, xz, or yz, homogeneous deformation is obtained tilting the simulation box and remapping all the monomers in the new box. Conceptually, this remapping corresponds to forcing all monomers to undergo the same global displacement, i.e. undergo an affine deformation. Since the non-affine contribution (relaxation of the monomers to energetically more convenient positions after deformation) has been recently shown to be significant in the elastic response of glassy systems [22], a minimization is performed after each strain increment, which reproduces the non-affine displacements of monomers, by relaxing them towards their equilibrium positions.

In every deformation process along a chosen direction, the initially cubic ($xy = xz = yz = 0$ in eq. (2.16)) simulation box is deformed by increasing the corresponding tilt factor from zero to 15% of the box side, in 15000 increments of 0.001%. The global stress is computed by average on all the monomers, while the strain considered is that of the simulation box.

For instance in a simple and homogeneous shear deformation along the xy direction, like that shown in fig. 4.1, the coordinates $\mathbf{X}$ of all the points in the box are mapped into the new ones $\mathbf{x}$ in the following way[1]:

$$x = X + \frac{xy}{L}Y \tag{4.1}$$

$$y = Y \tag{4.2}$$

$$z = Z \tag{4.3}$$

The displacement field $\mathbf{u}(\mathbf{X})$ is just

$$u_x = \frac{xy}{L}Y \tag{4.4}$$

$$u_y = 0 \tag{4.5}$$

$$u_z = 0 \tag{4.6}$$

[1]Notice that this transformation is applied also to the coordinates of the monomers only in the first step. By performing minimization, monomers take new coordinates and in this configuration the stresses are computed.

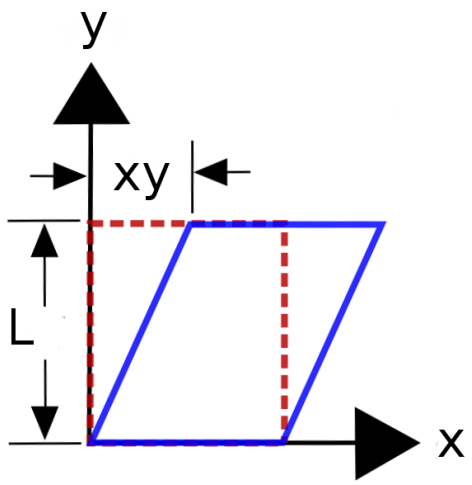

Figure 4.1: Two dimensional view of the xy-sheared simulation box of side L. The red dashed line corresponds to the profile of the original box, whereas the blue full line is the profile of the box when sheared with tilt factor xy. The global strain in this case is $\frac{xy}{L}$.

and the corresponding macroscopic shear strain (which in the engineering notation is twice that in eq. (1.24)) is then

$$2 \cdot u_{xy} = \left(\frac{\partial u_x}{\partial Y} + \frac{\partial u_y}{\partial X} \right) = \frac{xy}{L} \tag{4.7}$$

After each strain increment and minimization, the global stress is computed. The resultant total stress is plotted against the macroscopic strain, in order to obtained stress-strain curves like the one shown in fig. 4.2.

It is here reminded that the systems studied consist in $N_c = 160$ chains of $M = 25$ monomers, either fully flexible ($k_\theta = 0.0$) with diverse bond lengths l_b, or with fixed bond length $l_b = r_0 = 1.12$ and diverse chain stiffness k_θ, where r_0 is the bead diameter.

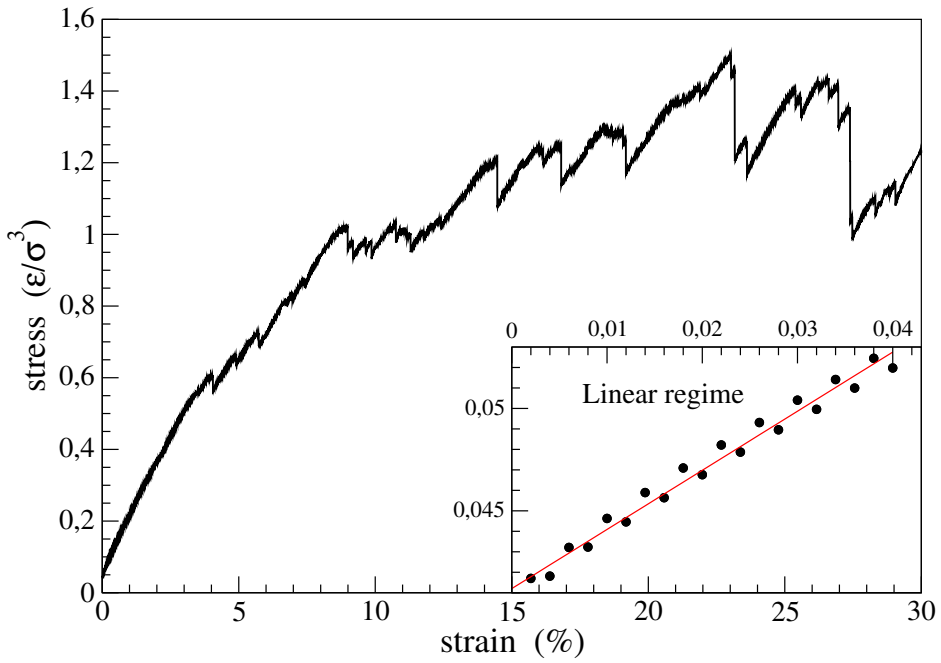

Figure 4.2: Example of a typical stress-strain curve. In the inset, the fitted data in the linear regime are shown.

4.2 Shear modulus

For small deformations, the mechanical response is expected to be linear, and described by eq. (1.31). When the applied deformation is a simple shear, all the diagonal components of both the strain and stress tensor are zero, while the non diagonal components are related by eqs. (1.32), (1.33) and (1.34)

$$\sigma_{xy} = 2G_3 u_{xy}$$

$$\sigma_{xz} = 2G_4 u_{xz}$$

$$\sigma_{yz} = 2G_5 u_{yz}$$

In our study of shear elastic response, the engineering definition of strain $\gamma_{ik} = 2u_{ik}$ is adopted, and the characteristic simple shear modulus G of a sample is estimated as

$$G = \frac{1}{3}\left(G_3 + G_4 + G_5\right) \tag{4.8}$$

Each of the components $G_{3,4,5}$ of a sample can then be measured by fitting the corresponding stress-strain curve in its linear regime. This regime of small

strain is not well-defined and must be chosen as a compromise between a small enough upper threshold of strain and a reasonable number of points to fit under that threshold. The reason for the former condition comes directly from the definition of shear modulus, whereas the latter condition is required in order for the fit to be reliable.

We chose to fit all the stress-strain curves with a strain threshold $\gamma^t_{ik} = 4 \cdot 10^{-2}$, which in our measurements allowed for 21 points to fit. An example is reported in fig. 4.2.

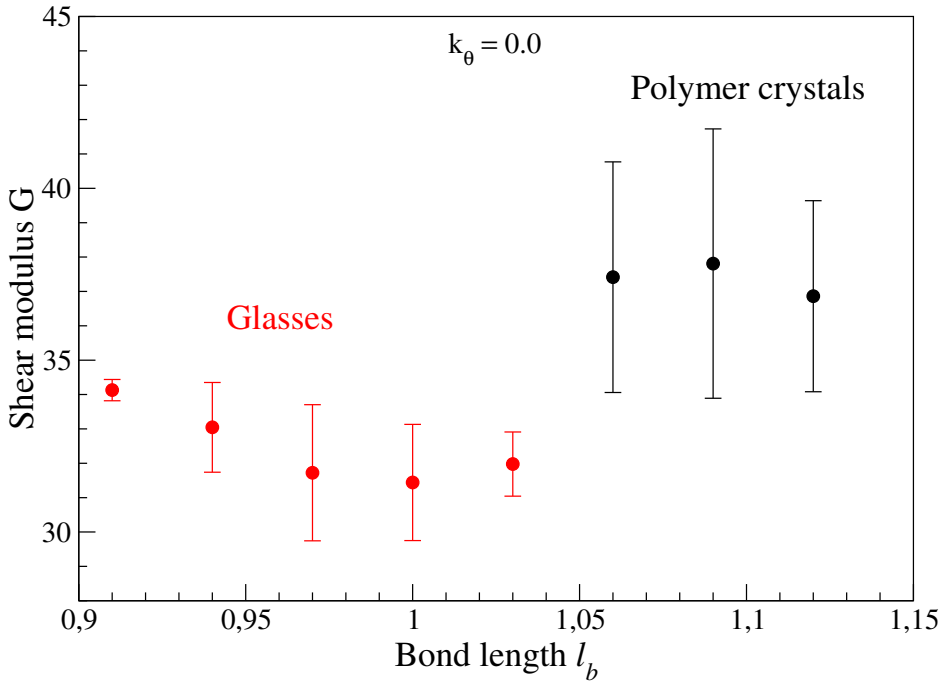

Figure 4.3: Shear modulus plotted against bond length. The two families of points correspond to glasses (red dots) and polymer crystals (black dots). For each sample G is obtained via average on the moduli measured in 16 different simulation runs. The associated error is the standard deviation of these measures.

In order to understand the role of chain connectivity on the elastic response of the zero temperature solids obtained via cooling, the shear modulus G, as averaged on the measures for 16 simulation runs, is plotted both against bond length l_b (in fig. 4.3) and against chain stiffness k_θ (in fig. 4.4).

The reported error is estimated as the standard deviation of the values obtained on each run. The fact that these errors are very large must not be ascribed to the precision of measurement. The reason for large errors is that in any simulation run the same system is stuck by glass transition in a

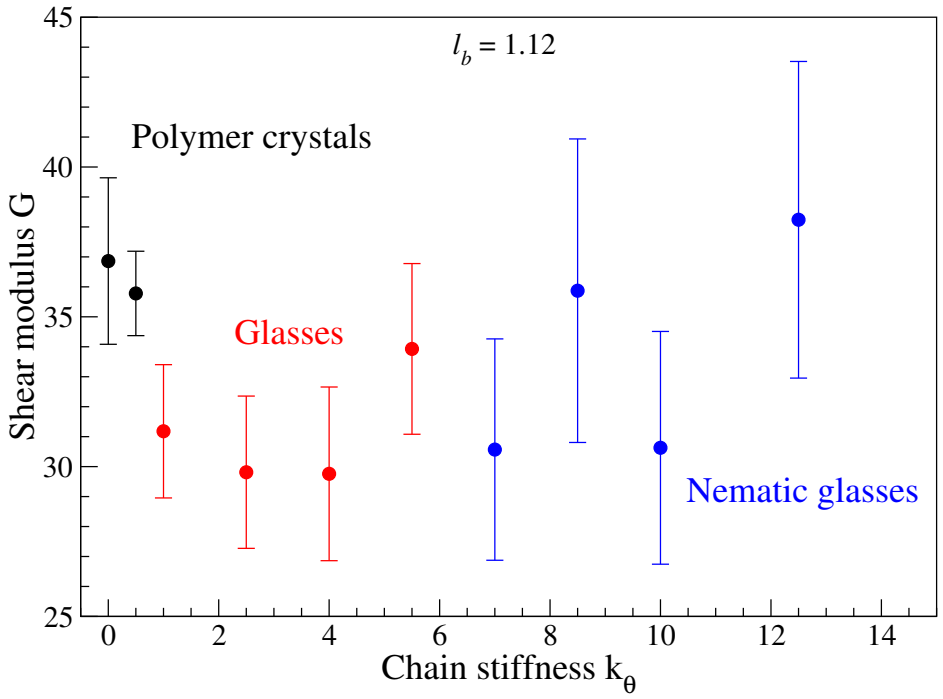

Figure 4.4: Shear modulus plotted against chain stiffness. The three families of points correspond to polymer crystals (black dots), glasses (red dots) and nematic glasses (blue dots) . For each sample G is obtained via average on the moduli measured in 16 different simulation runs. The associated error is the standard deviation of these measures.

different local minimum of potential energy, to which a certain configuration corresponds. To this configurations can correspond strongly different elastic properties.

Keeping in mind the qualitative nature of these results, the only effect that can be ascribed to chain connectivity is that of a decreasing trend of $G(l_b)$ observed in glasses, at least for small values of l_b. This trend seems to invert near the threshold bond length $l_b = 1.03$ over which partial crystallization occurs. Except for this slight trend, within the same family of systems (polymer crystals, pure and nematic glasses), neither bond length nor chain stiffness is observed to have effect on the elastic response.

One more evident effect in shear moduli is observed between the two families of polymer crystals and pure glasses. Polymer crystals generally show a stronger elastic response with respect to completely amorphous systems. As the case of nematic glasses stands alone, with shear moduli that span a range of values including those of both polymer crystals and glasses, it can be

concluded that the only structural feature that affects the elastic response is the global order (see fig. 3.19 and fig. 3.28 for differences in local and global ordering among the different solid structures).

4.3 Yielding properties

A yielding event is identified as an abrupt drop in stress, occurring at some point on the stress-strain curve of a sample, after which stress starts to rise again with strain. A yielding event is thus a significant relaxation process for a material subjected to deformation.

The physical quantities used to characterize the yielding behaviour of a sample are the scalar strain

$$u_y = \frac{1}{3}\left(u_y^{xy} + u_y^{xz} + u_y^{yz}\right) \tag{4.9}$$

and scalar stress

$$\tau_y = \frac{1}{3}\left(\frac{\sigma_y^{xy}}{2} + \frac{\sigma_y^{xz}}{2} + \frac{\sigma_y^{yz}}{2}\right) \tag{4.10}$$

at which the first considerable yielding event occurs. Since many stress drops $\Delta\sigma$ of different size are observed in a single stress-strain curve (ranging from order 10^{-3} to 10^{-1}), the determination of whether an event is considerable or not is quite arbitrary. A reasonable choice must then be done of a threshold value of stress drop $\Delta\sigma_t$, over which the drop is associated to a proper yielding event. The value

$$\Delta\sigma_t = 0.1$$

has been found to be a good choice, since a stress drop of that size is usually the starting point of a series of other similar drops and rises, which characterizes a different mechanical response of the sample with respect to the precedent.

The values of strain u_y and stress τ_y at yield for the systems with different bond length l_b and chain stiffness k_θ, each resulting from average on 16 simulation runs, are reported respectively in fig. 4.5 and fig. 4.6. The corresponding errors are the standard deviation of the values obtained in the runs. These errors give an estimate of the mean range of values obtained for the same system arrested by glass transition in different configurations.

The range of strain at which a sample yields is very similar among systems with different chain stiffness and bond length, namely $4.5 \leq u_y(l_b) \leq 6.3$ and $4.3 \leq u_y(k_\theta) \leq 8.6$. Thus, the strain required for a system to yield depends neither on the structure nor on connectivity.

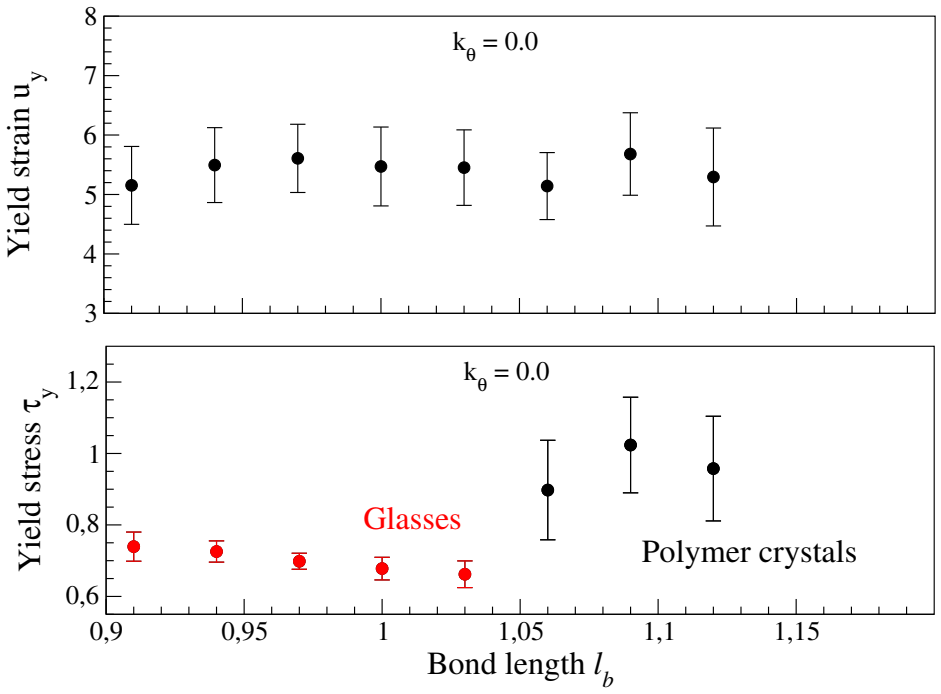

Figure 4.5: Strain (upper panel) and stress (lower panel) measured at yield for fully flexible systems of different bond length. Dots are the values resulting from average on the simulation runs, and error bars are their standard deviations. While yield strain is the same for all systems inside error, stress is quite different from totally amorphous (red dots) to partially ordered solids (black dots). Yield stress also slightly decreases with bond length.

The situation is different for the yield stress. At equal strain reached, the gathered stress at yielding is different from system to system. The largest difference is found between polymer crystals and glasses: the yield stress of polymer crystals is $0.8 \leq u_y \leq 1.2$, whereas it is included in $0.6 \leq \tau_y \leq 0.8$ for glasses of fully flexible polymers and in $0.35 \leq \tau_y \leq 0.7$ for glasses of semi-flexible and stiff polymers. Thus, completely amorphous and more ordered structures yield under the same amount of strain, but the latter gather more stress before yielding.

Yield stress also appears to be weakly related to chain connectivity in amorphous glasses. Even if inside the error $\tau_y(l_b)$ and $\tau_y(k_\theta)$ can be said to be constant, a general decreasing trend can be observed in both. The situation for fully flexible glasses is particularly interesting as this trend seems to follow that of shear modulus, suggesting a possible correlation between τ_y and G.

This possibility has been investigated by plotting the couple of measured

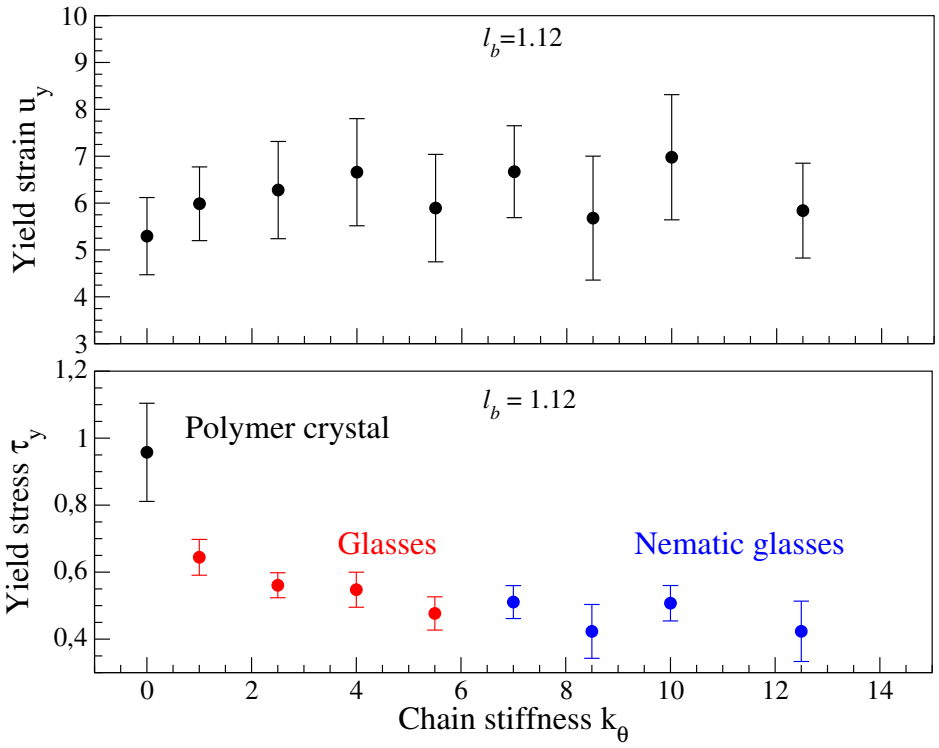

Figure 4.6: Strain (upper panel) and stress (lower panel) measured at yield for semi-flexible systems of different chain stiffness. Dots are the values resulting from average on the simulation runs, and error bars are their standard deviations. All systems share the same range of strain values at yield. Again, the greatest difference in yield stress is found passing from the partially ordered (black dot) to the totally amorphous (red dots) and nematic (blue dots) solids. Way slighter decreasing dependence on chain stiffness is observed.

(τ_y, G) for every single run of the fully flexible systems (characterized by different bond lengths). The results are shown in fig. 4.7 (upper panel). In this plot, the errors on stress are vanishing small, since LAMMPS computes stresses with a precision of 10^{-6}, whereas the error on the shear modulus of a single run results from fitting the stress-strain curve in its linear regime, and is then propagated with respect to eq. (4.8).

The measures are fitted linearly with zero intercept:

$$\tau_y = u_c \cdot G \tag{4.11}$$

with a resulting slope of

$$u_c = 0.0234 \pm 0.0028 \tag{4.12}$$

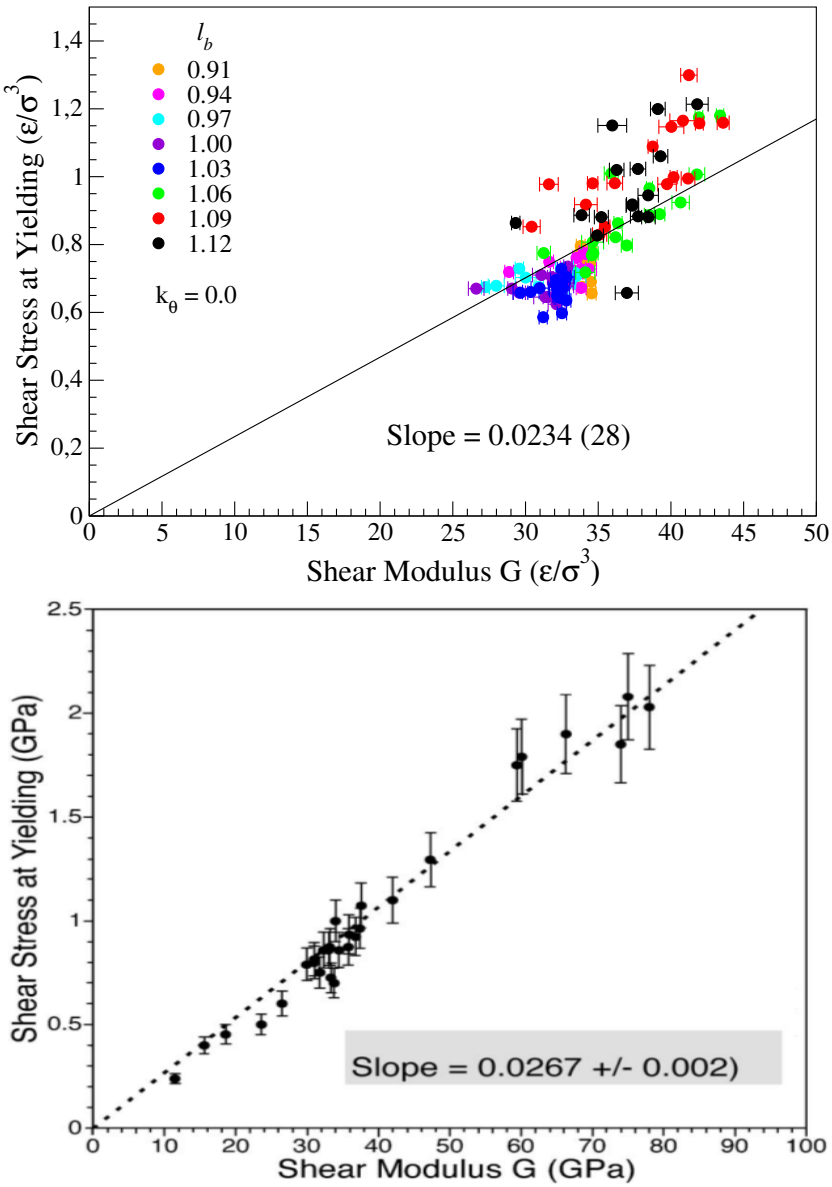

Figure 4.7: Correlation between yield stress u_y and shear modulus G. The upper panel shows measurements carried out in this work on the simulated fully flexible bead-spring model, first cooled down to zero temperature and then shear-deformed via the AQS protocol. Data are fitted with a linear formula of zero intercept. In the lower panel, the same measurement as carried out experimentally in [45] on metallic glasses at room temperature. Notice that in spite of the large differences between the two measurements (one obtained by MD simulations of macromolecular systems, the other by experiments performed on atomic systems), the fitting curve can be reasonably considered the same. This suggests an universality in the nature of this correlation.

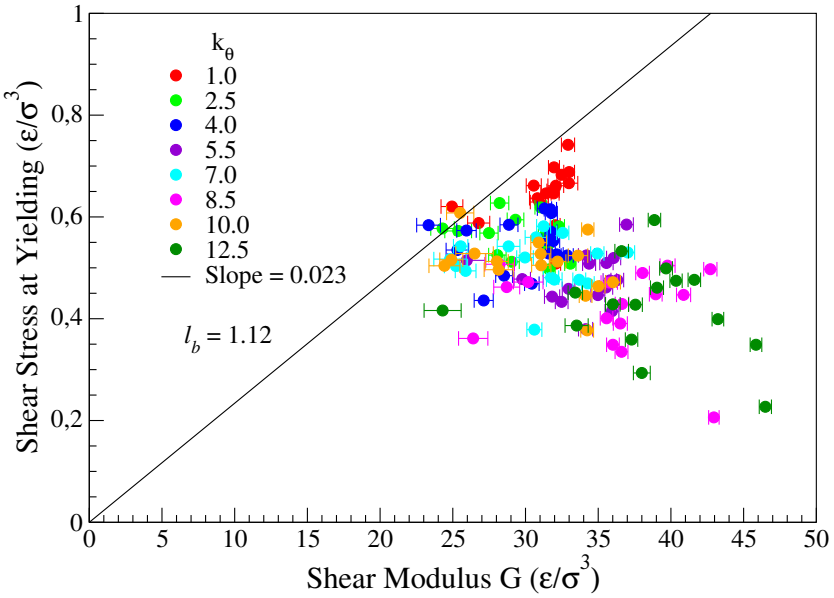

Figure 4.8: Deviation of systems of semi-flexible polymers from the linear correlation between the stress at yielding τ_y and the simple shear modulus G, observed in the fully-flexible case. The deviation is more significant the stiffer are polymer chains (i.e. the larger is chain stiffness k_θ).

This fit clearly has not to be intended as a best fit procedure. Rather, the aim is to show that the cluster of ≈ 130 couples of $(\tau_y,\ G)$ tend to distribute along a line, which is compatible with that obtained experimentally in [45] for metallic glasses (lower panel of fig. 4.7), namely $u_c^{exp} = 0.027 \pm 0.002$. The great differences between the latter study and this work are remarkable: first, the results in [45] are experimental, while here they come from MD simulations; second, the model glasses studied here are polymeric, i.e. made up of chain macromolecules of connected monomers, while metallic glasses are atomic systems.

The fact that despite these strong differences, the results are compatible, is quite interesting as it suggests some kind of universality in the correlation between two deeply different behaviours of glasses, i.e. the elastic response to small perturbations (deformations) and the highly non-linear phenomenon of yielding. In effect, the model presented in [45] in order to explain the $\tau_y(G)$ correlation, which is one of those that rely on the existence of a physical law like eq. (1.35), has no particular restrictions to metallic glasses.

In order to test the domain of this universality, the existence of the correlation $\tau_y = u_c \cdot G$ is investigated also for glasses of semi-flexible polymers. The results are shown in fig. 4.8. It is evident that in general eq. (4.11) is

not satisfied. But it can also be observed that the deviation is significant only for the highly stiff polymer glasses. The difference between the latter and metallic glasses is larger than in the case of fully flexible polymers, since connectivity in very stiff polymers has much greater importance than in fully-flexible ones, for which the only additional interaction with respect to the atomic systems is that of the bond between monomers subsequent along the chain.

Also the structure appears to have a role in the $\tau_y(G)$ correlation, since the systems which deviate more from eq. (4.11) are the partial crystals ($l_b \geq 1.06$ in fig. 4.7) and the nematic glasses ($k_\theta \geq 5.5$ in fig. 4.8). This is still consistent with the results of [45] as they refer to completely amorphous systems.

4.4 Conclusions

The mechanical response under simple shear deformation, of the semi- and fully-flexible bead-spring polymer models has been characterized in this chapter. In particular, the role played by the parameters determining the connectivity (bond length l_b and chain stiffness k_θ) has been investigated.

The mechanical response has been characterized through the measurement of the simple shear modulus G and of the stress τ_y and strain u_y at yielding. In addition the existence of a correlation between G and τ_y has been investigated and the results have been compared with the experimental observations reported in [45].

Within the family of glasses of fully flexible polymers, a very weak dependence of $G(l_b)$ is observed, with a monotonically decreasing trend which inverts at that value of bond length which sets the threshold for partial crystallization (at our fixed quench rate). But the strong difference in simple shear modulus is found to stand between glasses and partial crystals. The degree of ordering of the solid structure is thus what determines the elastic strength of the system.

The behaviour of $G(k_\theta)$ is more confused. The difference in strength between partial crystals and glasses is confirmed for low values of chain stiffness k_θ, but from the value $k_\theta = 5.5$ on, the observed shear moduli span the range of both crystals and glasses. The ranges of G for nematic glasses are particularly broad.

As far as the phenomenon of yielding is concerned, we observed that the strain at yielding is, in spite of its broad range, practically the same for all the systems, from the partial crystals of fully flexible polymers to the glasses of stiff polymers, irrespective of both structure and connectivity. On the other hand, the stress at yielding is sensitive to structure and to chain stiffness.

It is highest in crystals, and it monotonically decreases with k_θ in glasses of semi-flexible polymers including the nematic glasses, which are the ones with the lowest average stress at yielding.

A correlation is found between the stress at yielding τ_y and the simple shear modulus G of fully flexible polymer glasses. This correlation is compatible with that experimentally verified in [45] on metallic glasses, which have a strongly different feature with respect to our model, that of being atomic systems, i.e. without connectivity. In analogy with these results, the observed $\tau_y(G)$ is fitted with the linear relation eq. (4.11)

$$\tau_y = u_c \cdot G$$

where

$$u_c = 0.0234 \pm 0.0028$$

to be compared with the experimental measure reported in [45]

$$u_c^{exp} = 0.027 \pm 0.002$$

In the systems of semi-flexible polymers a significant deviation from this linear relation is observed. This deviation tends to increase with chain stiffness k_θ.

However, considering the great difference between the systems studied (glasses of polymer chains of 25 monomers and atomic metallic glasses) and between the methods of investigation used (MD simulations and experiments), the compatibility between the two results is reasonable, suggesting the existence of an universality of the correlation $\tau_y(G)$ for a class of systems. This class includes partially or totally amorphous systems, both atomic and polymeric (connected), at least as long as the stiffness of connections can be neglected.

Chapter 5

Summary of results

The original results obtained in this work, and presented in the last two chapters, are here summarized.

- The static properties of our polymer model in the liquid phase have been characterized, through analysis of the pair distribution function $g(r)$, the bond angle distribution $P(\cos\theta_b)$, and of the angular distributions of first and second neighbours $ADF(r_I,\ \cos\phi)$ and $ADF(r_{II},\ \cos\phi)$;

- The gap between the two characteristic lengths r_0 and l_b has a disordering effect resulting in the progressive flattening of all the distributions. Chain stiffness k_θ has an analogous but weaker effect;

- The solidification behaviour of the model undergoing linear cooling, is affected by the parameters related to connectivity, l_b and k_θ:

    * Systems with large $|l_b - r_0|$ gap tend to vitrify, while as the gap vanishes crystallization is favoured;

    * Intermediate values of stiffness hinder crystallization, whereas high values give rise to chain-scale order, which results in a solid state characterized by a nematic glassy phase;

- Both the glass transition temperature T_g and the crystallization temperature T_c increase as $|l_b - r_0|$ tends to vanish, in fully flexible polymers;

- In stiff polymers, the glass transition temperature T_g increases smoothly with intermediate values of k_θ. On the other hand, the increase in the solidification temperature T_s of transition to the nematic glass phase is discontinuous;

- The static properties of the low temperature solids obtained via cooling have been observed and compared to their liquid phase equivalent. The global and local order of the solid structures have been characterized, confirming the disordering effects of the gap $|l_b - r_0|$ and of chain stiffness k_θ;

- The elastic response at zero temperature of the solids, subjected to small simple shear deformation, has been characterized. Connectivity does not directly affects the elastic properties. However, since the latter depend on the ordering of monomers, connectivity plays a role by determining the solidification behaviour of the system.

- The yielding behaviour under large deformations has been characterized. The yield strain is independent of connectivity, while yield stress in amorphous glasses shows a decreasing trend with increasing k_θ (increasing chain-scale order);

- There is a correlation between the linear elastic response and the yielding behaviour of the zero temperature solids, at least in systems with low chain stiffness;

- The data related to this correlation are reasonably compatible with experimental data reported in the literature. Data are compatible when metallic glasses (experiment) and highly flexible connected systems (simulation) are compared, suggesting the existence of a universal nature of this correlation, irrespective of connectivity. However, there are important deviations from this correlation law, when chain stiffness is sufficiently large.

Appendix A

Monitoring of thermodynamic quantities

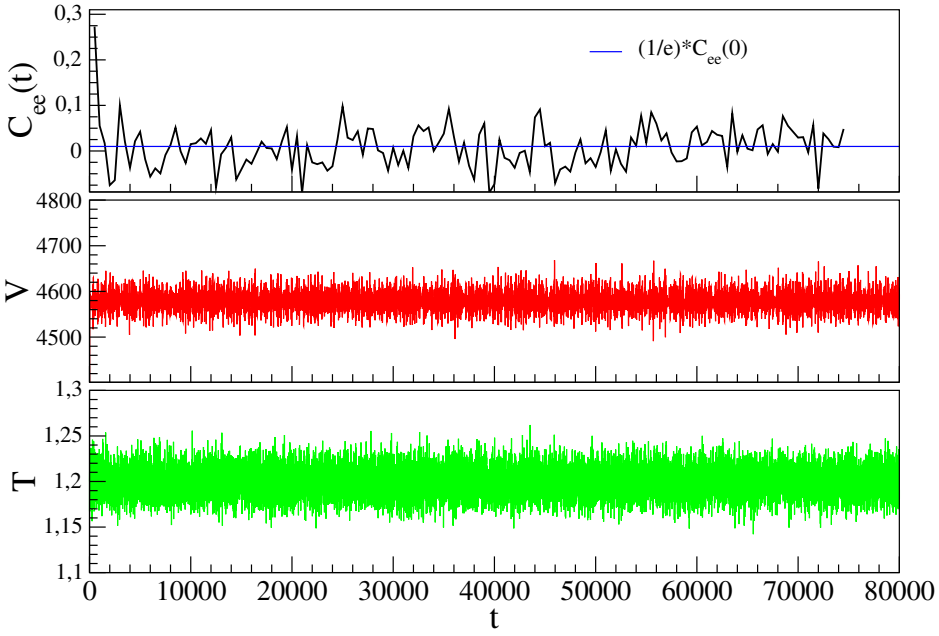

Figure A.1: Typical time evolutions of the end-to-end vector correlation function $C_{ee}(t)$, volume V and temperature T, during the equilibration period. Apart from fluctuations, temperature is kept constant on average by the external thermostat, and volume also fluctuates around its equilibrium value. Notice the blue line in the upper panel, corresponding to the value $\frac{1}{e}C_{ee}(0)$. The time at which C_{ee} reaches this value is the maximum relaxation time of the system τ_{ee}.

Some examples of the thermodynamic quantities monitored during the

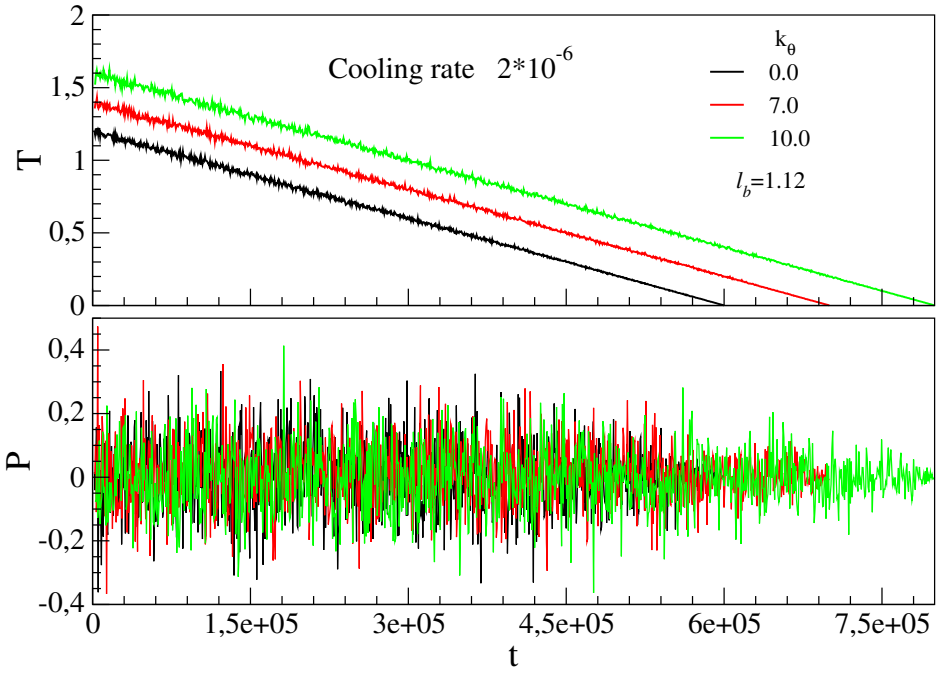

Figure A.2: Linear decrease of temperature during the cooling procedure at finite quench rate $2 \cdot 10^{-6}$ (upper panel) and the corresponding time evolution of pressure, which is kept at zero on average by the external barostat. The initial temperatures are different for systems with different stiffness.

equilibration and cooling procedures are reported for completeness, respectively in fig. A.1 and fig. A.2.

Bibliography

[1] P. G. Debenedetti, *Metastable liquids: concepts and principles*, Princeton University Press, Princeton, 1996.

[2] D. Cangialosi, *Journal of Physics: Condensed Matter*, 2014, **26**, 153101.

[3] D. Gundermann, U. R. Pedersen, T. Hecksher, N. P. Bailey, B. Jakobsen, T. Christensen, N. B. Olsen, T. B. Schrøder, D. Fragiadakis, R. Casalini, C. M. Roland, J. C. Dyre and K. Niss, *Nature Physics*, 2011, **7**, 816–821.

[4] R. S. Smith and B. D. Kay, *J. Phys. Chem. Lett.*, 2012, **3**, 725–730.

[5] C. A. Angell, *J. Phys. Chem. Solids.*, 1988, **49**, 863–871.

[6] H. S. Chen and M. Goldstein, *J. Appl. Phys.*, 1972, **43**, 1642–1648.

[7] S. Rogers and L. Mandelkern, *J. Phys. Chem.*, 1957, **61**, 985–991.

[8] J. C. Dyre, *Rev. Mod. Phys.*, 2006, **78**, 953–972.

[9] P. G. Debenedetti and F. H. Stillinger, *Nature*, 2001, **410**, 259–267.

[10] C. A. Angell, *J. Non-Cryst. Sol.*, 1991, **131-133**, 13–31.

[11] H. Bässler, *Phys. Rev. Lett.*, 1987, **58**, 767–770.

[12] I. Avramov, *J. Non-Cryst. Solids*, 2005, **351**, 3163–3173.

[13] Y. S. Elmatad, D. Chandler and J. P. Garrahan, *J. Phys. Chem. B*, 2009, **113**, 5563–5567.

[14] C. A. Angell, *Science*, 1995, **267**, 1924–1935.

[15] U. W. Gedde, *Polymer Physics*, Chapman and Hall, London, 1995.

[16] J. Baschnagel and F. Varnik, *J. Phys.: Condens. Matter*, 2005, **17**, R851–R953.

[17] J.-L. Barrat, J. Baschnagel and A. Lyulin, *Soft Matter*, 2010, **6**, 3430–3446.

[18] G. Strobl, *The Physics of Polymers, III Ed.*, Springer, Berlin, 2007.

[19] C. A. Angell, K. L. Ngai, G. B. McKenna, P. McMillan and S. W. Martin, *J. Appl. Phys.*, 2000, **88**, 3113–3157.

[20] M. Doi and S. F. Edwards, *The Theory of Polymer Dynamics*, Clarendon Press, 1988.

[21] L. D. Landau and E. M. Lifshitz, *Theory of Elasticity*, Pergamon Press, 1986.

[22] H. Mizuno, S. Mossa and J.-L. Barrat, *Phys. Rev. E*, 2013, **87**, 042306.

[23] Z. Wang, J. Li, W. Zhang, J. Qiao and B. Wang, *Metals*, 2015, **5(3)**, 1188–1196.

[24] J. L. Barrat and A. Lemaitre, in *Dynamical heterogeneities in glasses, colloids, and granular media*, ed. L. Berthier, G. Biroli, J. Bouchaud, L. Cipelletti and W. van Saarloos, Oxford university press, 2011, ch. 8.

[25] F. Stillinger, *Science*, 1995, **267**, 1935–1939.

[26] D. L. Malandro and D. J. Lacks, *J. Chem. Phys.*, 1999, **110**, 4593–4601.

[27] M. Utz, P. G. Debenedetti and F. H. Stillinger, *Phys. Rev. Lett.*, 2000, **84**, 1471–1474.

[28] S. Plimpton, *J. Comput. Phys.*, 1995, **117**, 1–19.

[29] S. Nosé, *J. Chem. Phys.*, 1984, **81**, 511–519.

[30] W. G. Hoover, *Phys. Rev. A*, 1985, **31**, 1695–1697.

[31] H. C. Andersen, *J. Chem. Phys.*, 1980, **72**, 2384–2393.

[32] G. J. Martyna, M. L. Klein and M. Tuckerman, *J. Chem. Phys.*, 1992, **97**, 2635–2643.

[33] G. J. Martyna, D. J. Tobias and M. L. Klein, *J. Chem. Phys.*, 1994, **101**, 4177–4189.

[34] W. Shinoda, M. Shiga and M. Mikami, *Phys. Rev. B*, 2004, **69**, 134103.

[35] W. C. Swope, H. C. Andersen, P. H. Berens and K. R. Wilson, *J. Chem. Phys.*, 1982, **76**, 637–649.

[36] A. W. Lees and S. F. Edwards, *J. Phys. C: Solid State Physics*, 1972, **5**, 1921.

[37] S. S. Ashwin and S. Sastry, *J. Phys.: Condens. Matter*, 2003, **15**, S1253–S1258.

[38] K. Kremer and G. S. Grest, *J. Chem. Phys.*, 1990, **92**, 5057–5086.

[39] R. S. Hoy and N. C. Karayiannis, *Phys. Rev. E*, 2013, **88**, 012601.

[40] H. T. Nguyen, T. B. Smith, R. S. Hoy and N. C. Karayiannis, *J. Chem. Phys.*, 2015, **143**, 144901.

[41] P. J. Steinhardt, D. R. Nelson and M. Ronchetti, *Phys. Rev. B*, 1983, **28**, 784–805.

[42] S. Bernini, F. Puosi, M. Barucco and D. Leporini, *J. Chem. Phys.*, 2013, **139**, 184501.

[43] D. T. F. Seitz, *Solid State Physics*, Academic Press, 1966.

[44] M. Talati, T. Albaret and A. Tanguy, *EPL (Europhysics Letters)*, 2009, **86**, 66005.

[45] W. L. Johnson and K. Samwer, *Phys. Rev. Lett.*, 2005, **95**, 195501.

[46] E. Lerner, I. Procaccia, E. S. C. Ching and H. G. E. Hentschel, *Phys. Rev. B*, 2009, **79**, 180203.